DYNAMICS OF MICROFLUIDIC AQUEOUS TWO-PHASE COMPOUND DROPLETS

WANG PENGZHI

NATIONAL UNIVERSITY OF SINGAPORE

2011

DYNAMICS OF MICROFLUIDIC AQUEOUS TWO-PHASE COMPOUND DROPLETS

WANG PENGZHI
(B.ENG NUS)

A THESIS SUBMITTED FOR THE DEGREE OF MASTER OF ENGINEERING

DEPARTMENT OF CHEMICAL AND BIOMOLECULAR ENGINEERING

NATIONAL UNIVERSITY OF SINGAPORE
2011

Summary

An aqueous two-phase system (ATPS) composed of dextran and polyethylene glycol provides a reliable and biocompatible platform for purification of biomedical products and cellular macromolecules. The incorporation of such an ATPS into microfluidics would make automated on-chip purification of desirable proteins and other products possible. In addition, microfluidic aqueous two-phase droplets could potentially be used to better mimic intracellular fluid environment. In order to control the physical and topological behaviors, it is therefore crucial to understand both the hydrodynamics and the thermodynamics of the aqueous two-phase microfluidic droplets. This thesis aims to address some of the relevant issues on such complex microfluidic droplets from hydrodynamic and thermodynamic point of view, which will help in better control and monitoring of on-chip ATPS.

The first part of the project focuses on the creation and characterization of microfluidic aqueous two-phase droplets. Continuous and uniform droplets can be successfully produced at a Y-shaped junction. The microfluidic droplets exhibit a continuum of morphologies for different flow speeds and compositions and they have been well classified to facilitate subsequent discussions. Some other interesting experimental phenomena have been observed, including the very fine reticulate heterogeneous fluid structures, fractal emulsions and the creation of micron-sized satellite ATPS droplets. They can potentially have great industrial applications.

In the second part, the underlying physics has been investigated. The rationales for transitions between different droplet morphologies have been investigated in analogy with the existing theory on droplet dynamics in an unconfined linear Stokes flow. Then, the characteristic size of the fluid filaments under strong shear stress has been determined by the technique of Fast Fourier Transform of the images. The interface thickness for compositions near the binodal line is calculated based on the Cahn-Hilliard theory. Surprisingly, we find that the characteristic size of the fine fluid filaments approaches the order of the interfacial thickness for compositions in close vicinity of the binodal line. In addition, the possibility of homogenization by applying very strong shear is also discussed based on existing scientific literature. The effect of chaotic mixing on the droplet morphology induced by the presence of a meandering section has also been studied.

Publication:

1. Su Hui Sophia Lee, Pengzhi Wang, Swee Kun Yap, T. Alan Hatton and Saif A. Khan, 'Tunable Spatial Heterogeneity in Structure and Composition within Aqueous Microfluidic Droplets', *Lab on a chip* (to be submitted)

Conferences:

1. Saif A. Khan, S.H. Sophia Lee, Pengzhi Wang and Swee Kun Yap, 'Stirring Immiscible Liquids in Nanoliter Cavities', accepted for oral presentation at the 15th International Conference on Miniaturized Systems for Chemistry and Life Sciences (MicroTas), Seattle, USA (2011)
2. Saif A. Khan, S.H. Sophia Lee, Pengzhi Wang and Swee Kun Yap, Bulletin of the American Physical Society, 63rd Annual Meeting of the APS Division of Fluid Dynamics, Volume 55, Number 16 (2010)

To my grandparents, my parents,

my brother and my beloved Rao Ying

Acknowledgment

First of all, I sincerely thank my supervisor, Dr. Saif A. Khan, for his patient guidance on me, who initially did not have much background in this scientific domain. It has always been his rigorous attitudes, passion and enthusiasm towards modern sciences that motivate me. Apart from his encouragement and help in my research, I have also learnt many valuable philosophies in life from him. Especially, I have understood and appreciated the importance of his positive attitudes and enthusiasm towards daily life while working with him. I believe that both the scientific knowledge and the life philosophies that I learnt from Dr. Khan will benefit me for the entire life.

I also have to thank my partners, Sophia Lee and Sweekun Yap, for their continuous help when I messed up the experiments. It has been really fun to observe new experimental phenomena together with them. Moreover, I really appreciate the daily help from Pravien Parthiban whenever I encounter problems in the lab. I equally thank the rest of my lab mates, Suhanya Duraiswamy, Dr. Md Taifur Rahman, Zahra Barikbin, Abhinav Jain, Toldy Arpad Istvan, Reno Antony Louis Leon, for their generous assistance, for their kind encouragement when I was frustrated, and for the laughter that we have had together.

In addition, I feel obliged to thank Professor John W. Cahn for his kind explanation on one of his famous papers on spinodal decomposition, and Professor William C. Johnson for sending me the detailed derivation of the Cahn-Hilliard theory written by him and Professor Hubert I. Aaronson.

I have to thank my best friends, Huang Lei and Li Wenyi, and my beloved Rao Ying, for their encouragement and consolation whenever I feel demoralized.

At last, I thank my grandparents, my parents and my brother. Human is made of water physically, but is made of love emotionally.

Contents

List of Figures

List of Tables

List of Symbols

$a(a_0)$	Radius of liquid thread (Initial radius)
a, b, c	Mole fractions for a ternary mixture
A, B, C	Representation of the three species in a ternary mixture
c_i	Mole fraction for species i
C	Mean curvature or Cauchy-Green tensor (Page 101)
Ca	Capillary number (Page 42,57)
g	Local free energy (J/mol)
G	Free energy (J) or the characteristic velocity gradient (Appendix F)
H	Depth of the microchannel ($\cong 100\mu m$)
I_0, I_1	Bessel function of the first kinds
$\widetilde{I}_0, \widetilde{I}_1$	Modified bessel function of the first kinds
J, j_i	Diffusive flux of species i
k_B	Boltzmann Constant
K	Coefficient for the gradient term in Cahn-Hilliard's formulation (Page 19)
K_0, K_1	Bessel function of the second kinds
$\widetilde{K}_0, \widetilde{K}_1$	Modified bessel function of the second kinds
L_C	Characteristic filament width obtained from FFT
L_{calc}	$= R_{crit}$ on Page 41 of Janssen's thesis [31].
$\mathbf{m}$	The orientation vector
n	Number of moles of molecules per unit volume
$\mathbf{n}, \widehat{n}$	Normal vector of the interface

n_Δ	No. of moles of lattice sites per unit volume (Page 35)
N_A	Avogadro constant
$p(p')$	Hydrodynamic (hydrostatic) pressure
r, U	Parameters for Laudau-Ginzburg energy (Page 20)
R	Gas constant. $R = k_B N_A$
R_G	Radius of gyration of the polymer
S	Entropy
T_c	Critical temperature for a mixture
$u(\mathbf{R})$	Enthalpy of mixing for a molecule at the site $\mathbf{R}$
U	Flow speed of the microfluidic droplet
$\mathbf{v}$	Velocity vector
Re	Reynold's number (Page 41)
ρ	Density
η	Viscosity
η_d, η_c	Viscosity of the disperse, continuous phase
ϕ	Order parameter
χ_{ij}	Interaction parameter: $\chi_{ij} = z(E_{ij} - (E_{ii} + E_{jj})/2)/(k_B T)$ with z as the coordination number and E_{ij} as the free energy of formation of a chemical bond between a i molecule and an adjacent j molecule
$\sigma(\sigma^R)$	Interfacial tension (from regular solution model)
σ_{ij}	The ij-th entry of the Cauchy stress tensor σ
$\sigma_{(ij)}$	Interfacial tension between species i and species j

β, γ	Definition Eq 3.25 (Page 23)
$\gamma_A, \gamma_B, \gamma_C$	Lagrange multiplier (Page 67)
$\dot{\gamma}$	Shear rate. $\dot{\gamma} = \sqrt{2\Gamma : \Gamma}$
$\mu(\mu')$	Viscosity of the matrix fluid (of the inner liquid thread)
μ_i	Chemical potential of species i
λ	Interaction distance (Page 29) or wavelength of disturbance
$\kappa(\kappa_1)$	Wavenumber ($\kappa_1^2 = \kappa^2 + \omega\rho/\mu$)
κ_1, κ_2	Parameter in Cahn-Hilliard's formulation. Definition on Page 19
ω	Angular frequency of the wave (1/s)
Ω	Fluid domain of interests
$\partial\Omega$	Boundary of the fluid domain of interests
$\epsilon(\epsilon_1)$	Small parameters ($\epsilon, \epsilon_1 \ll 1$)
ε	Amptitude of disturbance
$\dot{\varepsilon}$	Elongation rate. $\dot{\varepsilon} = \Gamma : (\mathbf{m} \otimes \mathbf{m})$
Υ	An energy function defined by Nauman [41] (Page 67)
Γ	$\Gamma = (\nabla\mathbf{v} + \nabla^T\mathbf{v})/2$
$\nabla\cdot$	Divergence operator
∇	Gradient operator
∇^2, Δ	Laplacian operator
$\tilde{}$	Fourier transform
$*$	Convolution operator

Chapter 1

Introduction

This chapter will briefly talk about the motivation for the microfluidic technology and its current development. Its wide range of applications in the industry and its advantages over the traditional chemical processes will also be discussed. The second section will present the specific microfluidic system of interests in this project - microfluidic aqueous two-phase system.

1.1 Introduction to Microfluidics

In the past few decades, nanotechnology has been the central spotlight of modern research due to increasing public demand on more sophisticated and compact equipment and devices. With an initial hope of building a biochemical laboratory on a small chip, microfluidics emerged as a new discipline in nanotechnology which is revolutionizing the existing chemical and biomolecular processes. Microfluidics is the science of designing, manufacturing, and formulating devices and processes that deal with fluid quantities of the order of nanoliters or even picoliters, which involves a wide range of scientific disciplines. Nowadays, it is not only used for chemical and biomedical analysis [14], but also for chemical synthesis [33][30], kinetic studies [57][58], screening for drug development [14][49], etc. Since the early 1990s, there has been a rapid development in microfluidic domain which is facilitated by the standardized technologies used in microelectromechanical systems (MEMS) such as photolithography, reactive ion etching. The most recent soft lithographic techniques [69] provide a well-standardized protocol for microfluidic devices.

The microfluidic chip is a small device which consists of microchannels, inlets and outlets. The inlets of the device are connected to the fluid reservoirs. For a typical microfluidic system, the fluid is introduced into the microchannels via the inlets and is transported along the microchannels until the outlet. The most common means of driving fluids through microchannels is by use of either an applied pressure difference (achieved by the use of pressurized cylinders and syringe pumps) or an applied electric field. With the use of special channel geometries such as the T- shaped and Y-shaped junctions, immiscible fluids can be segmented into droplets of uniform size. Each droplet miniaturizes an isolated reactor with intensive mixing. The microfluidic droplets can be clearly observed under a microscope. Various analytical operations have been integrated on a microfluidic platform [14]. On chip chromatography and capillary electrophoresis systems have been developed and widely used. Optical spectroscopy methods like UV Vis, IR, Raman, Surface Enhanced Raman, Surface Plasmon Resonance have been successfully incorporated into microfluidic systems. Molecular emission detectors, flame emission and flame ionization detectors have also been embedded into microfluidic devices and so have been various chemiluminescence, electroluminescence and fluorescence detection systems.

The advantage of microfluidics over conventional chemical processes is its small characteristic size. The dimension of the channels is around 300 microns, which ensures a laminar flow condition. Hence, in many occasions, molecular diffusion dominates over convectional diffusion, which is desired for certain chemical processes. Multiphasic chemical reactions can be very efficient due to its high surface-volume ratio which facilitates the mass transfer from one phase to another. Due to the short distances in the microchannels, mass and heat transfer is extremely fast. Hence, the conditions of microfluidic processes such as temperature can be regulated and maintained accurately. For protein crystallization, it is also much easier to achieve a rapid quenching so that nucleation takes place within a short amount of time to ensure a uniform size distribution of protein crystals. Working with smaller amount of fluids also implies that there is reduced consumption of the chemical reagents. The cost of chemicals and the dangers of working with hazardous materials are also minimized. Microscale systems also allow the user to access newer reaction pathways than those accessible while using a macroscale reactor. Scaling out to increase production rather than scaling up as involved in macroscale reactor design eliminates the high cost redesign step involved in moving from lab scale to pilot plant scale. Ability to couple online sensors allows screening of reaction parameters to optimize yields and to control product quality.

1.2 Aqueous Two-Phase System

In the pharmaceutical industry, there are stringent regulations on the purity of the products to make sure that other impurity chemicals do not have harmful effects on human. However, most of the current industrial separation processes involve organic solvents which might alter the chemical properties of the biomedical products. In addition, it is very difficult to completely isolate the desired products from organic solvents which are mostly very toxic. Hence, the downstream processing of biomedical products requires both biocompatible and efficient purification techniques. Recently, aqueous two-phase systems (ATPS) have been extensively studied due to the fact that they do not contain harmful chemicals. One typical example is an aqueous two-phase system composed of poly(ethylene glycol) (PEG) and dextran (DEX). It has been found this ATPS is able to separate a variety of macromolecules, membranes, organelles and cells [3][68].

In addition, the biochemical reactions in living eukaryotic cells take place in a heterogeneous environment containing a variety of macromolecules. Most of the *in-vitro* studies in dilute aqueous solutions are not able to capture the influence of heterogeneity on the chemical reaction. The microfluidic aqueous two-phase droplet of volume of the order of picoliters that we are interested in can potentially mimic the heterogeneous environment inside a cell. One of the particularities of such aqueous two-phase systems is that their interfacial tension is extremely low. The typical range is from 1 to a few hundred $\mu N/m$ [56][18]. In the framework of this project, microfluidic aqueous two-phase systems composed of PEG and DEX solutions have been successfully created and carefully investigated.

Chapter 2

Experiments and Observations

This chapter will firstly explain in details the procedures for the fabrication of the microfluidic device used (Section 2.1). Many fascinating experimental observations will be summarized in the next section (Section 2.2). These include the tunable droplet morphologies depending on the compositions of the polymer solutions and flow rate, very fine reticulate heterogeneous fluid structures, fractal emulsions and the creation of micron-sized satellite ATPS droplets.

2.1 Fabrication of Microfluidic Devices

The microchannel is fabricated using standard soft lithography technique [69]. The device is made of the Poly(dimethylsiloxane)(PDMS) which has over the past few years been the universal material for the fabrication of microfluidic devices.

The micro-channel layout is firstly designed using special software - AutoCad. The design is then printed out as a emulsion transparency (Infinite graphics). The width of the micro-channels in our design is 300 micrometers with equal channel

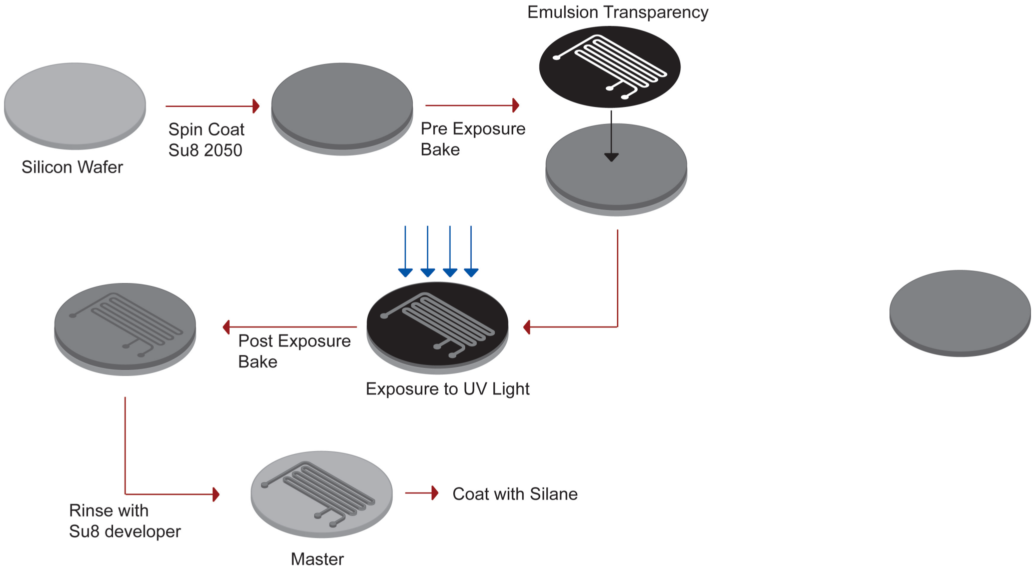

Figure 2.1: The detailed fabrication procedure of a master.

spacings. T-shaped or Y-shaped junctions are incorporated into the design to produce the segmented flow and ordered numbers are labeled along the channel to mark different positions on the chip. The printing of the emulsion transparency could accurately resolve features with characteristic dimensions as small as 20 micrometers and hence is able to fabricate channels of precise dimensions.

The master is fabricated using Su-8 2050 (MicroChem), a negative photo resist, with silicon wafer (4 inch, Syst Integration) as the substrate. The Silicon wafer is first kept on a hot plate (Heidolph) set at 250°C for 10 - 15 minutes to ensure that the wafer was dry. The Su-8 2050 is then spin-coated onto the silicon wafer after the wafer is allowed to cool down for a few minutes. The coated wafer is subsequently heated at 65°C for 10 minutes and subsequently at 95°C for 45 minutes before being slowly cooled down. The photolithography to define the micro-channels on the Su-8 coated wafers was carried out using a mask aligner system (MA8/BA6,

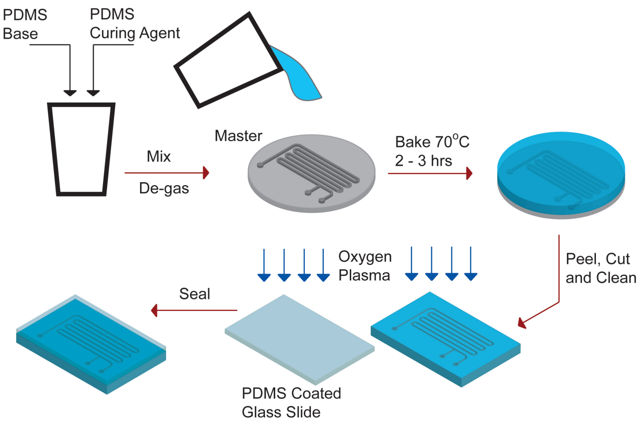

Figure 2.2: The detailed fabrication procedure of a PDMS replica.

Suss MicroTech). It is then exposed to UV lamp of intensity 8 mW/m^2 before being immediately transferred to a hot plate at 65°C for 5 minutes and then being baked at 95°C for 18 minutes. The wafer is then developed using Su-8 developer (MicroChem) by gentle agitation for approximately 40 minutes. Once all the unexposed Su-8 has been dissolved, the master is cleaned with isopropyl alcohol and dried under a stream of nitrogen. The master is then depth profiled using a Surface Profiler (P10,KLA-Tencor).

To make PDMS, a precursor base and a curing agent are mixed with a weight ratio of 10:1. The mixture is then degassed using a vacuum desiccator until no bubble is present in the liquid. This mixture is then poured over the silanized master placed in an aluminum foil dish before being baked at 70°C for 2 hours. The PDMS elastomer replica is subsequently peeled off the master carefully, cut into required shape and cleaned using scotch tape. Holes are also punched for the inlets and outlets in the PDMS replica. To seal the device, a glass slide(Corning Glass Works - 75 mm x 50 mm x 1 mm) spin-coated with PDMS and the PDMS replica are placed in a plasma cleaner for 45 seconds and are then brought into contact.

The PDMS surfaces oxidized by plasma will rapidly stick to each other. The whole device is then baked in a 100°C oven for another 24 hours. PEEK tubes (Vici, 1/16 inch outer diameter, 1mm inner diameter) of approximately 5 cm length for the inlet and 2.5 cm length for the outlet are fixed into the punched holes and glued using a two component epoxy (5 Minute Epoxy,Devcon).

2.2 Experimental Details and Observations

2.2.1 Phase Morphology Diagram

In our experiments, the DEX (MW = 500,000) solution and the PEG (MW = 8,000) solution are dispensed into the microfluidic channel via a Y-shaped junction and a mixture of perfluorodecaline(PFD) and perfluorooctanol(PO) with a volume ratio of 10:1 is injected as the continuous phase as shown in Figure 2.3. The DEX-PEG mixture will be segmented to droplets of uniform size by the continuous phase and is transported along the microfluidic channel. Above certain concentration, the aqueous mixture of two polymers will separate into two phases inside the droplet: one PEG-rich phase and one DEX-rich phase which stays inside the PEG-rich phase (Figure 2.4(a)). Each droplet can be considered as an isolated cell or a microreactor which can potentially be used to study the heterogeneous reactions in cells or for separation of macromolecules. High-speed optical microscope is used to investigate the dynamic phase behavior of such microsystem.

Due to the extremely low interfacial tension between the two aqueous phases, different morphologies have been observed and classified into four categories depending on the flow rate: single-lobe, heterogeneously fragmented (transition), reticulate and fine-reticulate. At extremely low flow rate, the droplet contains a single lobe

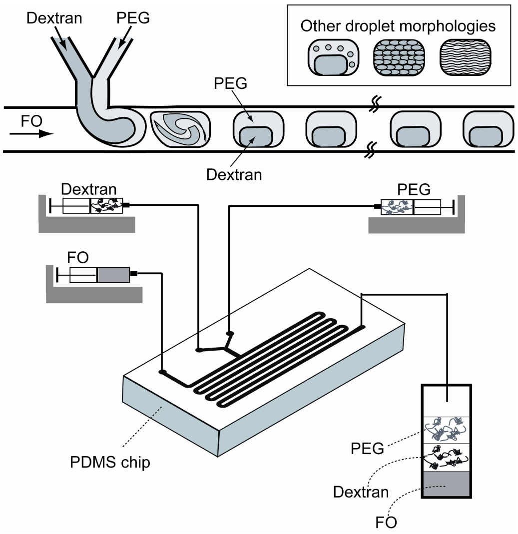

Figure 2.3: Schematics of the experimental setup

which maintains its shape as the droplet flows down in the microchannel as shown in Figure 2.4(a). As the flow rate increases, the interface starts to be torn apart and droplets of various size and shape can be observed inside the microfluidic droplet (Figure 2.4(b)). At high flow rate, the droplet exhibits a reticulated structure as shown in (Figure 2.4(c)). At even higher flow rate, the droplet will become transparent at a low microscope resolution (Figure 2.4(d)). If the microscope is adjusted to higher resolutions, uniform distribution of fine filaments can still be observed and we classify this morphology as a fine-reticulated structure (Figure 2.4(e)). One would naturally ask if a complete homogenization can be achieved by the shear stress in the microchannel and this question will be discussed in details in subsequent Chapters.

In addition, a miscibility map for the PEG-DEX aqueous mixture was constructed by doing experiments in batch (Figure 2.5(b)). In order to study how the flow rate and polymer composition influence the morphology of the droplet, a large number of experiments have been conducted with a fixed flow rate ratio (DEX: PEG:

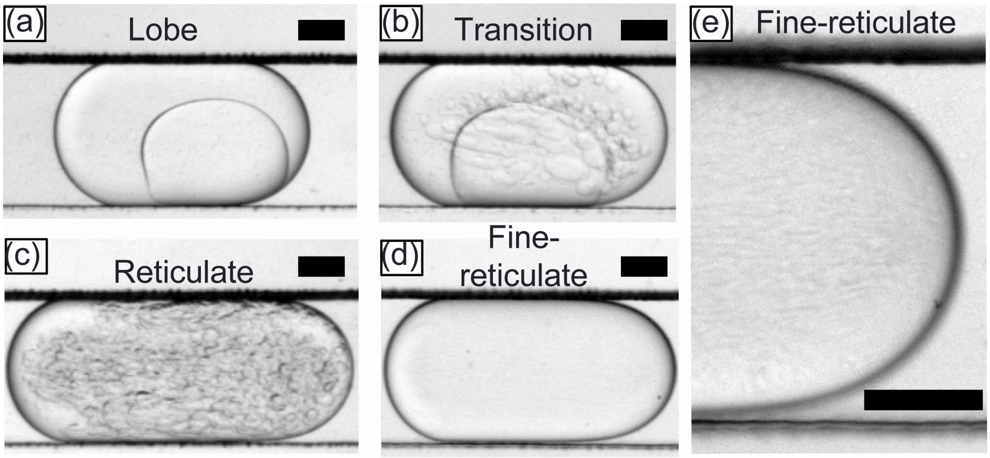

Figure 2.4: Typical images of the different morphologies of the aqueous two-phase droplets

Oil = 1: 1: 3). In addition, the weight percentage of PEG in the PEG stream is equal to that of DEX in the DEX stream. A morphology diagram was eventually constructed as shown by the different morphological regions in Figure 2.5(a). However, the two streams of polymer solutions at the inlet will coflow instead of forming emulsions and this specific region is named “Jet”.

One might argue that the reticulated structure may be influenced to a certain extent by the dispensing of the polymer mixture at the Y-shaped junction and hence we cannot conclude that the reticulated structure is completely due to the shear effect inside the droplet. Additional experiments have been dedicated to addressing this question. The flow was suddenly stopped and the droplets settled to a single-lobed morphology in a few minutes. Then the flow was restarted and it was observed that the single-lobed droplets became reticulated immediately as shown in Figure 2.6, which excluded the possibility that the dispensing at the inlet has influenced the morphology of the droplets.

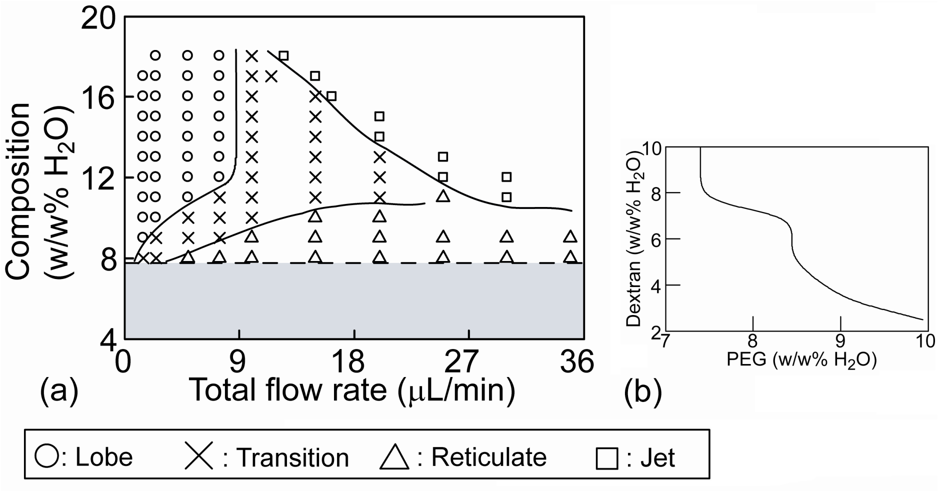

Figure 2.5: (a) Morphology diagram at different concentrations and flow rates. The flow rate ratio: PEG stream - DEX stream - Oil Stream = 1-1-3. The weight percentage of PEG in PEG stream is equal to that of DEX in DEX stream (b) The miscibility line

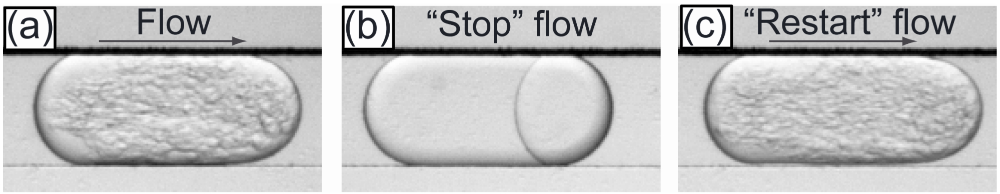

Figure 2.6: Morphology change of a stationary droplet after the flow is restarted

2.2.2 Study of the Fine-Reticulated Phase

An additional experiment was conducted in order to find out what happens to the homogenized droplets of DEX-PEG aqueous mixture after the flow is stopped. At compositions near the coexistence line (Figure 2.5(b)), the droplets appear to be transparent at relatively low resolution. After the pump was stopped, there was no phase separation taking place within the first twenty minutes (Figure 2.7(a)). The chip was left alone overnight and 15 hours later, all droplets inside the microchannel got back to the two-phase state with the DEX-rich phase surrounded by the PEG-rich phase (Figure 2.7(b)(c)). Hence, we can conclude that phase separation is actually a very slow process for the quasi-homogenized droplets induced by shear. In other words, we are able to produce a quasi-stable binary mixture just by applying shear in a microfluidic channel. This might have great applications in food industry because quasi-stable emulsions are desired like milk, etc. In addition, this might also be applied in protein separation because a quasi-homogenized phase maximizes the contact between different chemicals and phase separation could eventually take place off-chip. By drawing an analogy with the traditional process of separation, stopping the flow is an equivalent form of "quenching" which induces a transition from a homogeneous/quasi-homogeneous phase to phase separation.

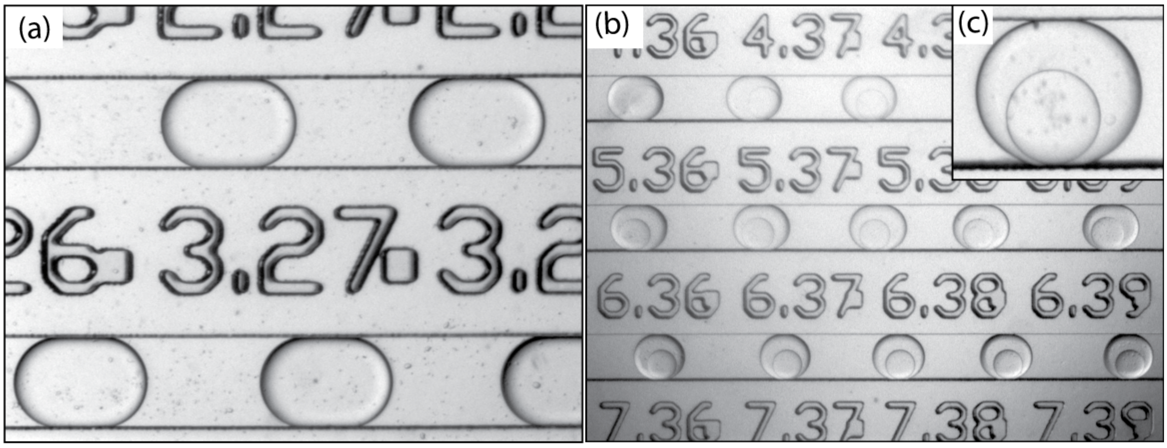

Figure 2.7: The morphology of the droplets after the pump was stopped (a) for 20 minutes (b) for 15 hours (c) a zoomed-in view

2.2.3 Fractal Emulsions

In the course of experiments, another fascinating phenomenon was observed. It was found that under certain circumstances, mostly for compositions near the miscibility line, nucleation and growth of a peculiar “third” aqueous phase develops along the channel as shown by Figure 2.8. One would naturally ask if it is possible that the third phase contains another phase, forming a fractal structure of multiple drop-in-drop complex. In the experiments by my lab mates, Toldy Arpad Istvan and Reno Antony Louis Leon, a fourth phase has been observed. Due to limitation of the equipment at our disposal, it is difficult to tell what this third and fourth aqueous phases contain. One plausible possibility is that the fluid rich in PEG is somehow trapped in the inner DEX-rich phase. They are then circulated along the streamline and cannot get contact to the outer PEG-rich bulk phase.

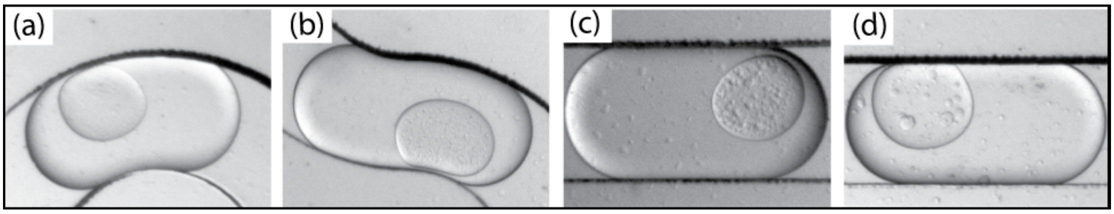

Figure 2.8: Nucleation and growth of a “third” phase inside the DEX-rich phase along the channel (a) the beginning of the meandering section (b) the end of the meandering section (c) the second lane (d) the third lane

2.2.4 Creation of Micron-sized Aqueous Two-Phase Droplets

The detachment of a water drop from the tap is in fact accompanied by the formation of a much smaller droplet of characteristic size of a few hundred microns that we cannot observe by naked eyes in daily life (Figure 2.9(c)). The phenomenon has been extensively investigated by fluid physicists because it poses many challenges to the printing technology. The suppression of such satellite droplets is crucial for designing precise ink spray devices [71]. On the other hand, the satellite droplets formed via such mechanism are of very uniform size and thus could be desirable for certain industrial applications. The formation of satellite droplets of micron size ($\sim 20\mu m$) is also observed in our experiments (Figure 2.9(a)(b)). If we are able to separate the satellite droplets from the big ones by special designs of the microchannels [62], it would be possible to produce micron-level aqueous two-phase emulsions of uniform size [1]. They can then be collected off-chip and be stabilized by adding surfactants.

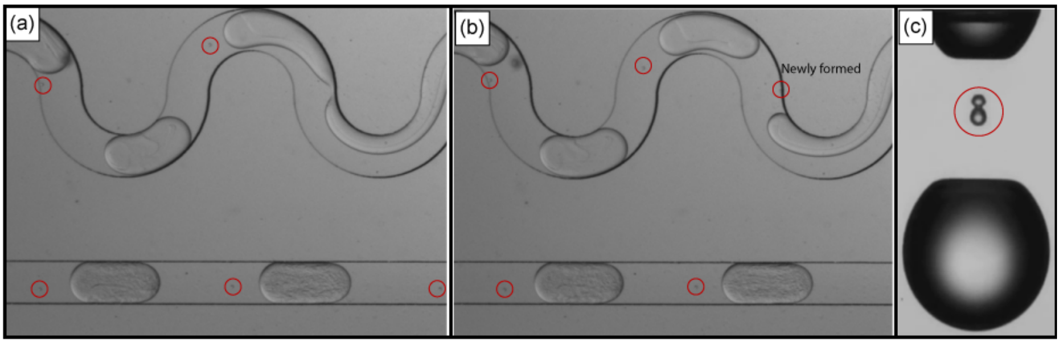

Figure 2.9: Formation of satellite droplets (a) the onset of the formation of an aqueous two-phase satellite in the microchannel (b) a newly formed satellite droplet (c) during the detachment of a water drop. The circles mark the location of the satellite droplets

---

[1] In fact, no evidence shows that the satellite droplets are aqueous two-phase ones. Further investigation on the composition of the satellite droplets is needed. However, due to limitation of our device and equipment at hands, it's difficult to have a detailed study in the framework of the thesis.

Chapter 3

Thermodynamics

In this chapter, the Cahn-Hilliard theory [8] for the interfacial free energy of a nonuniform binary mixture and its asymptotic dependence on temperature near critical conditions will be derived in details. The application of Cahn-Hilliard's formulation to nonuniform regular solutions will also be discussed. The original work by Cahn and Hilliard lacks detailed explanation and does not state the fact that the analysis near critical conditions applies the Landau theory. The author of this thesis gives a detailed flow of analysis from the Landau theory and also suggests some improvement and corrections on some coefficients. In addition, the dependence of the formation energy of a chemical bond between an i molecule and a j molecule on temperature is taken into account for analysis by the author as an improvement to the original paper by Cahn and Hilliard. The author also applies similar analysis for a ternary system and arrives at the conclusion that the surface free energy is minimized when the Δg term is equal to the gradient term (3.86). Based on these theoretical analysis, the interfacial thickness (l) of the PEG-dextran aqueous two-phase system(ATPS) will be approximately calculated from the experimental measurement of interfacial tensions for different compositions in literature [56][26]. As ATPS is well known for its low interfacial tension and diffused interface [26][36], this characteristic length (l) will give us a rough idea of the diffuseness of the PEG-dextran interface and will also help in further understanding of the hydrodynamics of the system, which will be discussed in the following chapters.

3.1 Landau Theory on Phase Transition

Phase transition happens everywhere in daily life and it has been one of the central spotlight of modern sciences. For example, the phase transition between solid, liquid and gas states, the transition between ferromagnetic and paramagnetic states of magnetic materials and the transition to superconductive state for certain materials, etc. In the terminology of modern physics, they are classified into first-order transition and second-order transition. First-order transitions are those that involve latent heat, like melting, evaporation, etc. For example,when the temperature is below the boiling point (T_e), the dependence of the free energy on density would be similar to (1) in Figure3.1(a2) and the free energy is minimized when the energy state of the system lies in the well on the right, corresponding to a higher density (ρ). As a result, the system would be liquid. When the temperature increases to above the boiling point, the system prefers an energy state in the well on the left, corresponding to a gas state of smaller density.

Examples of second-order transitions are the transition to superfluid, the transition between ferromagnetic and paramagnetic states, the spinodal decomposition of alloys upon cooling, and the transition to superconductive state. (Figure3.1(a1)(a2)). Lev Landau was the first to give a phenomenological explanation

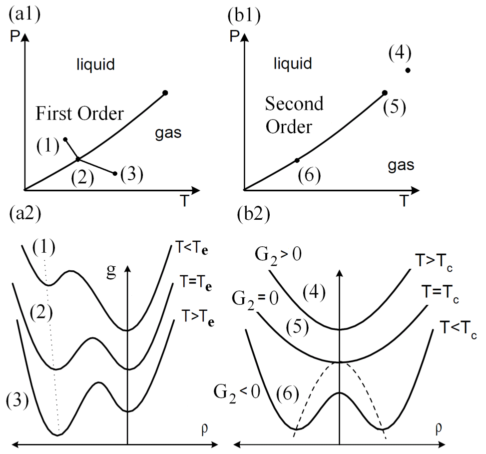

Figure 3.1: (a1)(a2) The profile change of the free energy of the first order transition (Evaporation) (b1)(b2) The profile change of the free energy of the second order transition, where T_m is the boiling point, G_2 is the second coefficient in Laudau's representation of free energy and T_c is the critical temperature for second order transition. The dash line traces the location changes of the two minima of the double-well profile as the temperature increases from below the critical temperature to the critical temperature.

on second order transition. Since the order parameter grows continuously from zero at critical point, Landau suggested a Taylor expansion of the free energy in the order parameter around critical point [9]. The free energy of a system should be a function of external variables and the order parameter ϕ, i.e.

$$G = G(T, P, \phi, N_i) \tag{3.1}$$

Since the order parameter is small near critical point. A Taylor expansion gives

$$G = G_0 + G_1\phi + G_2\phi^2 + G_3\phi^3 + G_4\phi^4 + ... \tag{3.2}$$

where G_i are all functions of T, P, and N_i. For binary alloy system, the odd terms have to vanish in order to preserve the symmetry of the system. Hence, we have

$$G = G_0 + G_2\phi^2 + G_4\phi^4 + ... \tag{3.3}$$

where G_4 is always positive by an argument of large fluctuation. This means that if the order parameter approaches the extreme values (either positive or negative), the corresponding energy state must be very large as well. If G_4 is negative, the energy of the system is minimized either at $\phi = 0$ or at extreme values (i.e., -1 or 1). It is the change of $G_2(T, P(T))$ with T that is responsible for the second order transition(Figure 3.1 (b1)(b2)). If $T < T_c$, $G_2 < 0$ and hence the free energy exhibits two minima which correspond to two states. If $T \geq T_c$, $G_2 \geq 0$ and the free energy has only one minimum. In this case, the system has homogenous composition. In other words, the second order transition takes place at $G_2(T) = 0$. A Taylor expansion of $G_2(T)$ at critical temperature gives

$$G_2 = G_2^*(T - T_c) + O\left((T - T_c)^2\right) ... \tag{3.4}$$

Due to the tendency of nature to minimize the free energy of the system, it is always thermodynamically preferred to be in states of minimum energy. At the minima of free energy, we must have

$$\frac{\partial G}{\partial \phi} = 2(T - T_c)G_2^*\phi + 4G_4\phi^3 = 0 \tag{3.5}$$

For $T < T_c$,

$$\phi = \pm\sqrt{\frac{G_2^*}{2G_4}(T_c - T)} \tag{3.6}$$

3.2 Cahn-Hilliard Theory

3.2.1 General Formulation of Free Energy

Cahn and Hillard [8] were the first to develop a comprehensive theory of phase separation based on the Landau-Ginzburg functional. The essential idea is that the free energy of a mixture per mole of mixture, g depends not only on the local composition but also on the local composition gradient. Therefore, they supposed that

$$G = n \int_{R^3} g d^3\mathbf{r} = n \int_{R^3} g(c(\mathbf{r}), \nabla c(\mathbf{r}), \nabla\nabla c(\mathbf{r}), ...) d^3\mathbf{r} \tag{3.7}$$

where $c(\mathbf{r})$ is the local mole fraction of one component, n is the number of moles of the mixture per unit volume and $\mathbf{r}$ is the scaled spatial vector with respect to the intermolecular distance, a_0, i.e., $\mathbf{r} = \mathbf{r}_{real}/a_0$. It is assumed that composition variation ($\sim O(1)$) is small as compared with the scaled distance $\mathbf{r}(\sim O(1000))$ over which there exists composition variation. Hence, the free energy function can be expanded into a Taylor series around the homogeneous composition field with zeros composition gradients, $g(c(\mathbf{r}), 0, 0, ...) = g_0(c)$

$$g(c(\mathbf{r}), \nabla c(\mathbf{r}), \nabla\nabla c(\mathbf{r}), ...) = g_0(c) + \left(\frac{\partial g}{\partial \nabla c(\mathbf{r})}\right)_{(c,0,0,..)} \cdot \nabla c(\mathbf{r}) +$$

$$\left(\frac{\partial g}{\partial \nabla\nabla c(\mathbf{r})}\right)_{(c,0,0,..)} : \nabla\nabla c(\mathbf{r}) + \frac{1}{2}\left(\frac{\partial^2 g}{\partial (\nabla c(\mathbf{r}))^2}\right)_{(c,0,0,.)} : (\nabla c(\mathbf{r}) \otimes \nabla c(\mathbf{r})) + ... \tag{3.8}$$

Here, we denote

$$\begin{aligned} \left(\frac{\partial g}{\partial \nabla c(\mathbf{r})}\right)_{(c,0,0,..)} &= L(c(\mathbf{r})) \\ \left(\frac{\partial g}{\partial \nabla\nabla c(\mathbf{r})}\right)_{(c,0,0,..)} &= K_1(c(\mathbf{r})) \\ \left(\frac{\partial^2 g}{\partial (\nabla c(\mathbf{r}))^2}\right)_{(c,0,0,.)} &= K_2(c(\mathbf{r})) \end{aligned} \tag{3.9}$$

It is important to note that the matrices L, K_1 and K_2 are functions of $c(\mathbf{r})$ only. Since the free energy is a scalar, it should be invariant with respect to reflection ($x_i \to -x_i$) and rotation ($x_i \to x_j$), where x_i stands for the spacial coordinates. The invariance with respect to reflection requires the term $L(c(\mathbf{r}))$ to vanish, whereas the invariance with respect to rotation makes $K_1(c(\mathbf{r})) = \kappa_1(c(\mathbf{r}))I$ and $K_2 = \kappa_2(c(\mathbf{r}))I$

where $\kappa_1(c(\mathbf{r}))$ and $\kappa_2(c(\mathbf{r}))$ are scalars which depends on the composition field $c(\mathbf{r})$ and I denotes the identity matrix. As a result, the Taylor series up to the second order is expressed as

$$g(c(\mathbf{r}), \nabla c(\mathbf{r}), \nabla\nabla c(\mathbf{r}), ...) = g_0(c) + \kappa_1 \nabla^2 c + \frac{\kappa_2}{2}(\nabla c)^2 + ... \tag{3.10}$$

By applying the divergence theorem[1], we arrive at

$$g = g(c, \nabla c) = g_0(c) + \frac{K}{2}(\nabla c)^2 \tag{3.11}$$

where $K/2 = [-d\kappa_1/dc + \kappa_2/2]_{(c,0,...)}$. Here, $g_0(c)$ is the free energy density for a homogeneous binary solution (J/mol). For example, the $g_0(c)$ of a binary mixture which obeys the regular solution model can be expressed as $g_0(c) = RT[clnc + (1-c)ln(1-c) + \chi c(1-c)]$, with χ as the interaction parameter and c as the mole fraction. In the original work of Cahn and Hilliard, the Landau-Ginzburg approximation was employed, i.e., $g_0(\phi) = -r\phi^2/2 + U\phi^4/4$, where r and U are two constants and the order parameter ϕ is defined as the concentration difference between the two components, i.e., $\phi = c_1 - c_2$. It is important to note that for small ϕ, the Landau-Ginzburg expression can be obtained by Taylor expansion of the regular solution model.

$$clnc + (1-c)ln(1-c) + \chi c(1-c) = \left(-ln2 + \frac{\chi}{4}\right) + \left(\frac{1}{2} - \frac{\chi}{4}\right)\phi^2 + \frac{1}{12}\phi^4 + ... \tag{3.12}$$

---

[1] In fact, the system is supposed to be infinitely large in the formulism of Cahn and Hilliard. Hence, the composition field $c(\mathbf{r})$ can be chosen such that $\nabla c(\mathbf{r}) \cdot \widehat{n} = 0$. By applying the divergence theorem, the surface integral term vanishes. However, in a more general setting, $\nabla c(\mathbf{r}) \cdot \widehat{n}$ may not be zero. H. I. Aaronson and W. C. Johnson have shown that κ_1 has to be zero in order to have a well-defined problem. Otherwise, an additional term $1/2\kappa_3(\mathbf{r})(\nabla^2 c(\mathbf{r}))^2$ has to be incorporated into the expression of the free energy density g

where $\phi = (1-c) - c$. In this context, the chemical potential[2] (J/mol) is defined as the variational derivative of the total free energy with respect to a function $c(\mathbf{r})$

$$\mu = \frac{\delta(G/n)}{\delta c(\mathbf{r})} = \frac{\partial g}{\partial c} - \nabla \cdot \frac{\partial g}{\partial \nabla c} = -K\nabla^2\phi - r\phi + U\phi^3 \tag{3.13}$$

At equilibrium, the chemical potential should be zero for a concentration field without constrains, i.e.,

$$-K\nabla^2\phi - r\phi + U\phi^3 = 0 \tag{3.14}$$

This differential equation has an analytical solution for a planar interface,

$$\phi(x) = \sqrt{\frac{r}{U}} tanh \frac{x}{\sqrt{2}\xi} \tag{3.15}$$

with $\pm\sqrt{r/U}$ the equilibrium bulk concentrations and ξ $(= \sqrt{K/r})$ the characteristic thickness of the interface.

3.2.2 Interfacial Tension Near Critical Condition

Under such a general setting, Cahn and Hilliard defined the specific interfacial energy (interfacial tension) as the difference per unit area of interface between the actual free energy of the system and that of a mixture of constant chemical potentials for each species. In the one-dimensional case, the surface tension is

$$\sigma = n \int_{-\infty}^{+\infty} \left(\Delta g(c) + \frac{K}{2} \left(\frac{dc}{dx} \right)^2 \right) dx \tag{3.16}$$

where $\Delta g(c) = g_0(c) - (c\mu_A + (1-c)\mu_B)$ and μ_A and μ_B are the chemical potentials (J/mol) of the species A and B respectively at the equilibrium compositions c_α (or c_β)(Figure 3.2). n denotes the number of moles of the mixture per unit volume. From

---

[2] This definition by Cahn and Hilliard is actually equivalent to the chemical potential difference between the two species, i.e., $\mu_A - \mu_B$

the treatment of phase equilibria by Gibbs, $\mu_A = g_0(c_\alpha) + (1 - c_\alpha)g_0'(c_\alpha) = g_0(c_\beta) + (1 - c_\beta)g_0'(c_\beta)$ and $\mu_B = g_0(c_\alpha) - c_\alpha g_0'(c_\alpha) = g_0(c_\beta) - c_\beta g_0'(c_\beta)$. According to this expression, if the average composition of a small system is inside the spinodal region, the system tends to phase separate in order to minimize the $\Delta g(c)$ term. However, phase separation will generate a composition gradient and thereby increasing the total free energy. If the system is too small, there would be a critical size below which the $(\nabla c)^2$ term becomes too dominant that the system prefers an uniform composition. In order to minimize the specific surface tension, the Euler-Lagrange equation has to be employed, i.e.

$$\frac{\partial I}{\partial c} = \frac{d}{dx}\left(\frac{\partial I}{\partial(dc/dx)}\right) \tag{3.17}$$

where I represents the integrand of Eq 3.16. Since I does not explicitly depend on x, the equation above can be written in another form (Beltrami Identity)

$$\frac{d}{dx}\left(I - \frac{\partial c}{\partial x}\left(\frac{\partial I}{\partial(dc/dx)}\right)\right) = 0 \tag{3.18}$$

where

$$\frac{d}{dx} = \frac{\partial}{\partial x} + \frac{dc}{dx}\frac{\partial}{\partial c} + \frac{d^2c}{dx^2}\frac{\partial}{\partial(dc/dx)}$$

With the boundary condition that both $\Delta g(c)$ and dc/dx tend to zero as x tends to infinity, the minimum condition for the free energy is obtained

$$\Delta g(c) = \frac{K}{2}\left(\frac{dc}{dx}\right)^2 \tag{3.19}$$

Hence, by applying Eq 3.19, the specific interfacial free energy is

$$\sigma = 2n\int_{-\infty}^{+\infty} \Delta g(c)dx = 2n\int_{c_\alpha}^{c_\beta} \Delta g(c)\frac{dx}{dc}dc =$$

$$2n\int_{c_\alpha}^{c_\beta} \Delta g(c)\left(\frac{K}{2\Delta g(c)}\right)^{1/2} dc = 2n\int_{c_\alpha}^{c_\beta}\left(\frac{K\Delta g(c)}{2}\right)^{1/2} dc \tag{3.20}$$

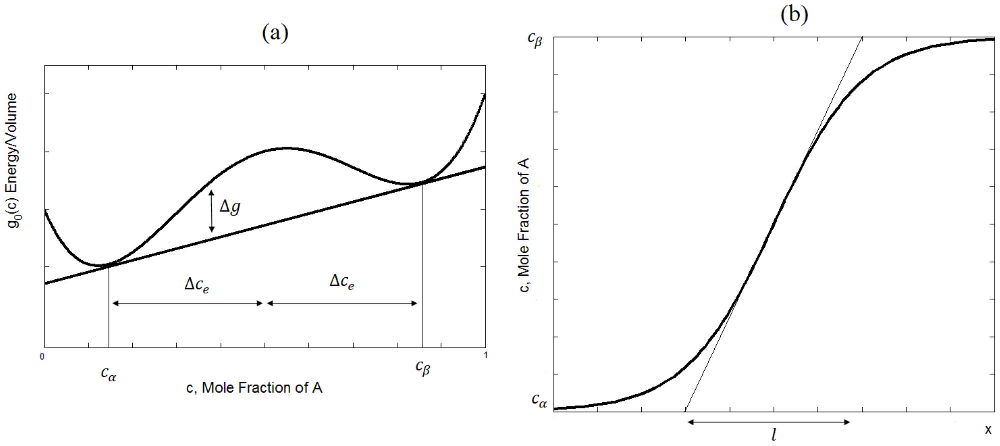

Figure 3.2: (a)The free energy as a function of composition (b) Composition profile of the interface and interfacial thickness, l.

In the following text, the composition profile near the critical temperature, T_c, and composition, c_c, is to be investigated based on the theory of Landau that has been explained in Section 3.1. In general, the order parameter in the formulation of Landau corresponds to the composition difference between the two species, i.e.,

$$\phi = c - (1 - c) = 2\Delta c \in [-1, 1] \tag{3.21}$$

If we have a regular solution, it is certain that the free energy difference $\Delta g(c)$ is symmetric with respect to c. Hence, $c - c_c = c_c - (1 - c) = \Delta c$ and $c_\beta - c_c = c_c - c_\alpha = \Delta c_e$. According to Eq 3.3 and Eq 3.4, near the critical temperature

$$g_0(c) = G_0 + G_2^*(T - T_c)(2\Delta c)^2 + G_4(2\Delta c)^4$$

$$g_0(c_\alpha) = G_0 + G_2^*(T - T_c)(2\Delta c_e)^2 + G_4(2\Delta c_e)^4$$

$$g_0(c_\beta) = G_0 + G_2^*(T - T_c)(2\Delta c_e)^2 + G_4(2\Delta c_e)^4 \tag{3.22}$$

Since

$$\Delta g(c) = g_0(c) - (c\mu_A + (1-c)\mu_B) = g_0(c) - (cg_0(c_\alpha) + (1-c)g_0(c_\beta)) \tag{3.23}$$

we have

$$\begin{aligned}(\Delta g(c))_{T\sim T_c} &= G_2^*(T-T_c)\left((2\Delta c)^2 - (2\Delta c_e)^2\right) + G_4\left((2\Delta c)^4 - (2\Delta c_e)^4\right)\\ &= \beta(T-T_c)\left((\Delta c)^2 - (\Delta c_e)^2\right) + \gamma\left((\Delta c)^4 - (\Delta c_e)^4\right) \qquad (3.24)\end{aligned}$$

where

$$\begin{aligned}\beta &= \left(\frac{1}{2!}\frac{\partial^3 g_0}{\partial T \partial c^2}\right)_{T=T_c} = 4G_2^* = 4\left(\frac{1}{2!}\frac{\partial^3 g_0}{\partial T \partial \phi^2}\right)_{T=T_c}\\ \gamma &= \left(\frac{1}{4!}\frac{\partial^4 g_0}{\partial c^4}\right)_{T=T_c} = 16G_4 = 16\left(\frac{1}{4!}\frac{\partial^4 g_0}{\partial \phi^4}\right)_{T=T_c} \qquad (3.25)\end{aligned}$$

By applying the Eq 3.6,

$$\left(\phi^2\right)_{T\sim T_c} = \frac{G_2^*}{2G_4}(T_c - T) \tag{3.26}$$

This is equivalent to write

$$(\Delta c_e)^2_{T\sim T_c} = \frac{\beta}{2\gamma}(T_c - T) \tag{3.27}$$

Combining Eq 3.27 and Eq 3.24, we have

$$(\Delta g(c))_{T\sim T_c} = \gamma\left((\Delta c_e)^2 - (\Delta c)^2\right)^2 \tag{3.28}$$

From Eq 3.20 and Eq 3.28, the specific interfacial free energy at equilibrium near critical condition is

$$\begin{aligned}(\sigma)_{T\sim T_c} = 2n\int_{-\Delta c_e}^{+\Delta c_e}\left(\frac{K\gamma}{2}\right)^{1/2}\left((\Delta c_e)^2 - (\Delta c)^2\right)d(\Delta c) =\\ 2n\int_{-\Delta c_e}^{+\Delta c_e}\left(\frac{K\gamma}{2}\right)^{1/2}\left(\frac{4}{3}(\Delta c_e)^3\right)d(\Delta c) \qquad (3.29)\end{aligned}$$

where the parameter K is assumed constant when it is sufficiently close to T_c. By applying Eq 3.27,

$$(\sigma)_{T\sim T_c} = \frac{2n}{3\gamma}K^{\frac{1}{2}}\beta^{\frac{3}{2}}(T_c - T)^{\frac{3}{2}} \tag{3.30}$$

3.2.3 Interfacial Thickness Near Critical Condition

The composition profile must satisfy the minimum condition (Eq 3.19) and applying Eq 3.28,

$$\frac{dc}{dx} = \frac{d\Delta c}{dx} = (2\Delta g/K)^{1/2} = \left(\frac{2\gamma}{K}\right)\left((\Delta c_e)^2 - (\Delta c)^2\right) \tag{3.31}$$

Since $\int 1/(1-x^2)dx = arctanh(x)$, Eq 3.31 can be integrated with boundary condition $\Delta c = 0$ at $x = 0$:

$$\int_0^{\Delta c} \frac{d\Delta c}{\Delta c_e^2 - \Delta c^2} = \frac{1}{\Delta c_e}\int_0^{\frac{\Delta c}{\Delta c_e}} \frac{d\left(\frac{\Delta c}{\Delta c_e}\right)}{1-\left(\frac{\Delta c}{\Delta c_e}\right)^2} = \frac{1}{\Delta c_e} arctanh\left(\frac{\Delta c}{\Delta c_e}\right) = \left(\frac{2\gamma}{K}\right)\int_0^x dx \tag{3.32}$$

We arrive at the conclusion that

$$\left(\frac{\Delta c}{\Delta c_e}\right)_{T \sim T_c} = tanh\left(\left(\frac{\beta(T-T_c)}{K}\right)^{1/2} x\right) \tag{3.33}$$

The interfacial thickness is estimated by l as shown in Fig 3.2(b). It is obtained by taking the slope of the free energy curve at $\Delta c = 0$ and determining the distance between the two intersects with $c = c_\alpha$ and $c = c_\beta$. Hence, by applying Eq 3.19

$$l = \frac{c_\beta - c_\alpha}{(dc/dx)_{c_c}} = \left(\frac{2\Delta c_e}{(2\Delta g/K)^{1/2}}\right)_{\Delta c=0} \tag{3.34}$$

From Eq 3.28,

$$(\Delta g)_{\Delta c=0} = \gamma(\Delta c_e)^4 \tag{3.35}$$

Hence, Eq 3.34 becomes

$$l = \left(\frac{2K}{\gamma}\right)^{1/2}\frac{1}{\Delta c_e} \tag{3.36}$$

From Eq 3.27,

$$l = 2\left(\frac{K}{\beta(T_c - T)}\right)^{1/2} \tag{3.37}$$

By combining Eq 3.30 and Eq 3.37, we find a relationship between the interfacial tension and the interfacial thickness near critical condition

$$\sigma l^3 = \frac{16nK^2}{3\gamma} \tag{3.38}$$

3.2.4 Application to Regular Solution

In classical thermodynamics, an ideal solution is defined as a mixture of multiple components which cannot be distinguished from one another and the free energy of mixing per mole is simply $g_0^{id} = RT \sum c_i ln c_i$. A regular solution refers to a mixture of multiple components with zero excess entropy and zero excess volume[3], i.e., $s^E = 0$ and $v^E = 0$. The free energy of mixing per mole of a binary regular solution is

$$g_0^R = RT\left(clnc + (1-c)ln(1-c) + \chi c(1-c)\right) \tag{3.39}$$

where $\chi = z(E_{AB} - (E_{AA} + E_{BB})/2)/(k_B T)$ with z as the coordination number and E_{ij} as the free energy of formation of a chemical bond between a i molecule and an adjacent j molecule and c represents the mole fraction of species A.

As we see from Figure 3.3, the double-well potential changes to a parabola at $\chi = 2$ and the critical composition $c_c = 0.5$. For a binary mixture, the chemical potential of each species can be calculated from the averaged free energy of the mixture by

$$\mu_A(c) = g_0 + (1-c)\frac{dg_0}{dc} \qquad \mu_B(c) = g_0 - c\frac{dg_0}{dc} \tag{3.40}$$

where c is the composition of species A. By using Eq 3.39, the chemical potential of the two species (J/mol) are

$$\mu_A(c) = RT\left(lnc + \chi(1-c)^2\right) \qquad \mu_B(c) = RT\left(ln(1-c) + \chi c^2\right) \tag{3.41}$$

---

[3] Excess property refers to the deviation from ideal solution model, i.e., $M^E = M - M^{id}$

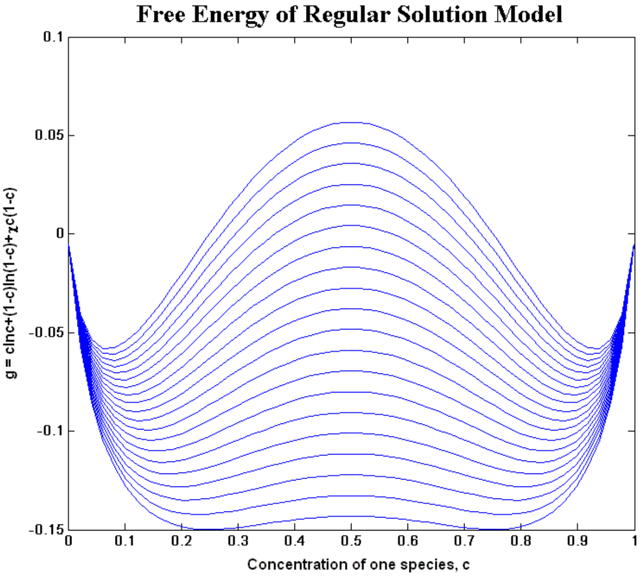

Figure 3.3: The scaled free energy for regular solution $g_0/RT = clnc + (1-c)ln(1-c) + \chi c(1-c)$ with χ changing from 3 to 2.2. Bifurcation occurs at $\chi = 2$

Note that $\mu_A(c)$ and $\mu_B(c)$ satisfy $g_0 = c\mu_A(c) + (1-c)\mu_B(c)$. The equilibrium compositions c_α or c_β (Figure 3.2) satisfies $g_0'(c) = 0$ [4], which gives

$$ln\left(\frac{c_e}{1-c_e}\right) = \chi(2c_e - 1) \tag{3.42}$$

where $c_e \in \{c_\alpha,\ c_\beta\}$.

---

[4] The free energy of a regular solution is symmetric and hence the equilibrium compositions correspond to $g_0' = 0$. Otherwise, they must satisfy $g_0'(c_\alpha) = g_0'(c_\beta) = (g_0(c_\alpha) - g_0(c_\beta))/(c_\alpha - c_\beta)$

Free Energy of a Nonuniform Regular Solution

Enthalpy

In this section, we will consider the cubic lattice model of a binary regular solution, where each molecule occupies one lattice site. The possibilities of find a A molecule at a particular lattice site R is denoted as $P(\mathbf{R})$ and it is equal to the local mole fraction of species A at R, i.e., $P(\mathbf{R}) = c(\mathbf{R})$. The probability of find a AB bond with A at site R and B at site S (Figure 3.4):

$$P_{AB}(\mathbf{RS}) = c(\mathbf{R})(1 - c(\mathbf{S})) \tag{3.43}$$

By Taylor expansion around the site R,

$$c(\mathbf{S}) = c(\mathbf{R}) + \nabla c(\mathbf{R}) \cdot \mathbf{r} + \frac{1}{2!}\nabla\nabla c(\mathbf{R}) : (\mathbf{r} \otimes \mathbf{r}) + \frac{1}{3!}\nabla\nabla\nabla c(\mathbf{R}) \vdots (\mathbf{r} \otimes \mathbf{r} \otimes \mathbf{r})... \tag{3.44}$$

where the vector $\mathbf{r} = \mathbf{S} - \mathbf{R}$, $r = |\mathbf{r}|$ and r_i is the ith component of the vector $\mathbf{r}$. In Einstein notation, Eq 3.44 is written as

$$c(\mathbf{S}) = c(\mathbf{R}) + \frac{\partial c(\mathbf{R})}{\partial x_i} r_i + \frac{1}{2!}\frac{\partial^2 c(\mathbf{R})}{\partial x_i \partial x_j} r_i r_j + \frac{1}{3!}\frac{\partial^3 c(\mathbf{R})}{\partial x_i \partial x_j \partial x_k} r_i r_j r_k ... \tag{3.45}$$

The number of lattice sites in the shell of radius from r to $r + dr$ is $nN_A dV = nN_A(r^2 sin\phi dr d\varphi d\phi)$, where n is the number of moles of the mixture per unit volume, N_A is the Avogadro number. The enthalpy of mixing for a molecule at the site R, $u(\mathbf{R})$, is calculated by fixing an A molecule at the site R. [5]Hence,

$$u(\mathbf{R}) = \int_0^{\pi} \int_0^{2\pi} \int_0^{+\infty} nN_A r^2 c(\mathbf{R})(1 - c(\mathbf{S}))\nu(r) dr d\varphi sin\phi d\phi \tag{3.46}$$

---

[5] One may argue that a B molecule can also occupy the site R. If we consider both cases (the site R is occupied by an A or B), each AB bond would be counted twice and a factor of 1/2 has to be added. It is equivalent to just consider the case where A is fixed at the site R.

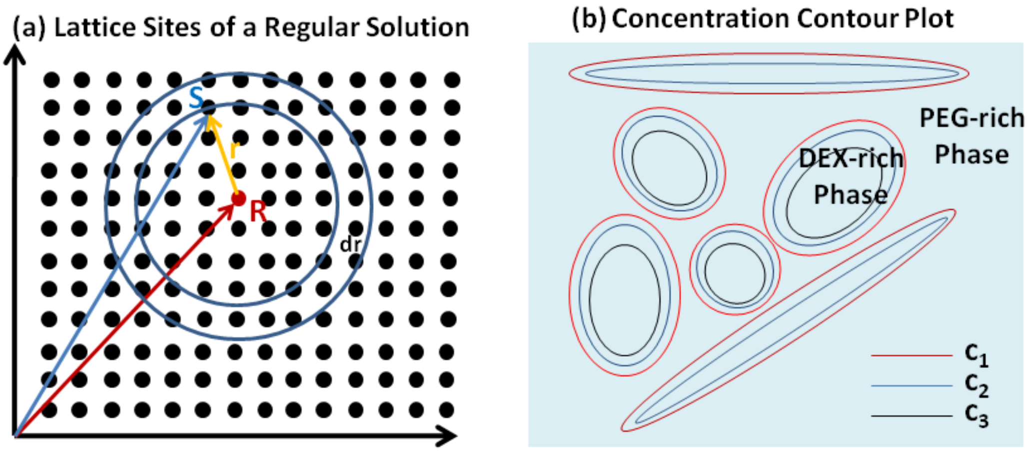

Figure 3.4: (a) The lattice site for a regular solution (b) The different equicomposition layers indicated in different colors.

where $\nu(r) = E_{AB}(r) - (E_{AA}(r) + E_{BB}(r))/2$ with $E_{ij}(r)$ as the formation energy of a chemical bond between an i molecule and a j molecule having a distance of r. Substitute Eq 3.44 into Eq 3.46,

$$u(\mathbf{R}) = \int_0^{\pi}\int_0^{2\pi}\int_0^{+\infty} nN_A r^2 c(\mathbf{R})\times$$

$$\left(1 - c(\mathbf{R}) - \nabla c(\mathbf{R})\cdot\mathbf{r} - \frac{1}{2!}\nabla\nabla c(\mathbf{R}) : (\mathbf{r}\otimes\mathbf{r})\right)\nu(r)drd\varphi sin\phi d\phi \tag{3.47}$$

The enthalpy per mole of molecules at the site R

$$\begin{aligned} h(\mathbf{R}) &= N_A u(\mathbf{R}) = N_A\omega c(\mathbf{R})(1 - c(\mathbf{R})) \\ &- N_A c(\mathbf{R})\nabla c(\mathbf{R})\cdot\int_0^{\pi}\int_0^{2\pi}\int_0^{+\infty} nN_A r^2\nu(r)\mathbf{r}drd\varphi sin\phi d\phi \\ &- \frac{1}{2}N_A c(\mathbf{R})\sum_i\sum_{j\neq i}\frac{\partial^2 c(\mathbf{R})}{\partial x_i\partial x_j}\int_0^{\pi}\int_0^{2\pi}\int_0^{+\infty} nN_A r^2\nu(r)r_i r_j drd\varphi sin\phi d\phi \\ &- \frac{1}{2}N_A c(\mathbf{R})\sum_i\frac{\partial^2 c(\mathbf{R})}{\partial x_i^2}\int_0^{\pi}\int_0^{2\pi}\int_0^{+\infty} nN_A r^2\nu(r)r_i^2 drd\varphi sin\phi d\phi \end{aligned} \tag{3.48}$$

where ω is defined as

$$\omega = 4\pi n N_A \int_0^{+\infty} r^2 \nu(r) dr \tag{3.49}$$

The second and the third terms of Eq 3.48 vanish. The enthalpy per mole of molecules at the site R is

$$h(\mathbf{R}) = N_A \omega c(\mathbf{R})(1-c(\mathbf{R})) - \frac{N_A}{2} c(\mathbf{R}) \sum_i \left(\frac{\partial^2 c(\mathbf{R})}{\partial x_i^2} \int_0^{\pi} \int_0^{2\pi} \int_0^{+\infty} n N_A r^2 \nu(r) r_i^2 dr d\varphi sin\phi d\phi \right)$$

$$= N_A \omega c(\mathbf{R})(1-c(\mathbf{R})) - \frac{N_A}{2} \frac{c(\mathbf{R})}{3} \left(\sum_i \frac{\partial^2 c(\mathbf{R})}{\partial x_i^2} \right) \int_0^{\pi} \int_0^{2\pi} \int_0^{+\infty} n N_A r^2 \nu(r) \left(\sum_i r_i^2 \right) dr d\varphi sin\phi d\phi$$

$$= N_A \omega c(\mathbf{R})(1 - c(\mathbf{R})) - 2\pi N_A c(\mathbf{R}) \frac{1}{3} \nabla^2 c(\mathbf{R}) \int_0^{+\infty} n N_A r^4 \nu(r) dr d\varphi sin\phi d\phi \tag{3.50}$$

because of the relation

$$\int_0^{\pi} \int_0^{2\pi} \int_0^{+\infty} r_1^2 r^2 \nu(r) dr d\varphi sin\phi d\phi = \int_0^{\pi} \int_0^{2\pi} \int_0^{+\infty} r_2^2 r^2 \nu(r) dr d\varphi sin\phi d\phi$$

$$= \int_0^{\pi} \int_0^{2\pi} \int_0^{+\infty} r_3^2 r^2 \nu(r) dr d\varphi sin\phi d\phi \tag{3.51}$$

If we define a root-mean-square interaction distance λ by

$$\lambda^2 = \frac{\int_0^{+\infty} r^4 \nu(r) dr}{3 \int_0^{+\infty} r^2 \nu(r) dr} \tag{3.52}$$

the enthalpy per mole of molecules (J/mol) at the site R follows from Eq 3.50

$$h(\mathbf{R}) = RT\chi \left(c(\mathbf{R})(1 - c(\mathbf{R})) - \frac{1}{2} \lambda^2 c(\mathbf{R}) \nabla^2 c(\mathbf{R}) \right) \tag{3.53}$$

with

$$\chi = \frac{\omega}{k_B T} \tag{3.54}$$

Entropy

In this section, we will carry out a discrete analysis of the lattice model. The local composition $c(\mathbf{r})$ a surjective map from the domain of lattice sites to a discrete set of composition values $\{c_1, ..., c_P, ...|\ 0 \leq c_P \leq 1\ \forall c_P\}$. The entire lattice can be classified to a finite number of equicomposition layers of composition $\{c_P\}$, containing N_P molecules correspondingly (Figure 3.4). The number of ways of arranging the molecules within the layer of composition c_P:

$$W_P = \frac{N_P!}{(c_P N_P)!((1-c_P)N_P)!} \tag{3.55}$$

The total number of ways of packing for the entire lattice is

$$W = \prod_P W_P \tag{3.56}$$

By Boltzmann's definition of entropy, the total entropy of the lattice

$$S = k_B lnW = k_B ln\left(\prod_P W_P\right) = k_B \sum_P lnW_P \tag{3.57}$$

By Stirling's formula, $ln(n!) = nlnn - n + O(lnn)$,

$$S = -k_B \sum_P N_P \left(c_P lnc_P + (1-c_P)ln(1-c_P)\right) \tag{3.58}$$

If we denote the entropy per molecules at a lattice site of composition c_P as $s(c_P)$, the total entropy of the lattice should be

$$S = k_B \sum_P N_P s(c_P) \tag{3.59}$$

By comparing Eq 3.58 with Eq 3.59, the specific entropy of a molecule at a lattice site of composition c is

$$s(c) = -k_B \left(clnc + (1-c)ln(1-c)\right) \tag{3.60}$$

which can be converted to the entropy per mole by multiplying a factor of $N_A = R/k_B$. This is the same as the entropy of a uniform regular solution of composition c.

Free Energy

From the enthalpy and entropy expression of a non-uniform regular solution, Eq 3.53 and Eq 3.60, the free energy per mole at position $\mathbf{r}$ (Eq 3.7)

$$g(c(\mathbf{r}), \nabla c(\mathbf{r})) = g_0^R - \frac{1}{2} RT\chi\lambda^2 c(\mathbf{r})\nabla^2 c(\mathbf{r}) \tag{3.61}$$

where g_0^R is defined by Eq 3.39. In the treatment of Cahn and Hilliard (Eq 3.10), the parameter κ_1, κ_2 and K can be identified

$$\kappa_1 = -\frac{1}{2} RT\chi\lambda^2 c(\mathbf{r}) \qquad \kappa_2 = 0 \tag{3.62}$$

$$\frac{K}{2} = -\frac{d\kappa_1}{dc} + \frac{\kappa_2}{2} = \frac{1}{2} RT\chi\lambda^2 \tag{3.63}$$

In conclusion, the free energy per mole of molecules of a nonuniform regular solution ($\nabla c(\mathbf{r}) \neq 0$) at a lattice position $\mathbf{r}$ is

$$g(c(\mathbf{r}), \nabla c(\mathbf{r})) = g_0^R(c(\mathbf{r})) + \frac{1}{2} RT\chi\lambda^2 (\nabla c(\mathbf{r}))^2 \tag{3.64}$$

Interfacial Free Energy and Thickness for a Regular Solution

Using Eq 3.39 and Eq 3.41, the Δg term in Eq 3.16 for a regular solution is calculated

$$\Delta g^R = g_0^R - (c\mu_A + (1-c)\mu_B) = RT\left(-\chi(c-c_e)^2 + cln\left(\frac{c}{c_e}\right) + (1-c)ln\left(\frac{1-c}{1-c_e}\right)\right) \tag{3.65}$$

where $c_e \in \{c_\alpha,\ c_\beta\}$. The derivatives of g_0^R (Eq 3.39) are listed:

$$\begin{aligned}
\left(g_0^R\right)' &= \frac{\partial g_0^R}{\partial c} = RT(\chi(1-2c) + lnc - ln(1-c)) \\
\left(g_0^R\right)'' = \frac{\partial^2 g_0^R}{\partial c^2} &= RT(-2\chi + \frac{1}{c} + \frac{1}{1-c}) = -2N_A\omega(T) + RT(\frac{1}{c} + \frac{1}{1-c}) \\
\left(g_0^R\right)''' &= \frac{\partial^3 g_0^R}{\partial c^3} = RT(-\frac{1}{c^2} + \frac{1}{(1-c)^2}) \\
\left(g_0^R\right)'''' &= \frac{\partial^4 g_0^R}{\partial c^4} = RT(\frac{1}{c^3} + \frac{1}{(1-c)^3})
\end{aligned} \tag{3.66}$$

From the definitions Eq 3.25 and with the property of regular solutions $c_c = 1/2$,

$$\beta^R = \frac{1}{2!}\left(\frac{\partial\left(g_0^R\right)''}{\partial T}\right)_{T=T_c} = \frac{1}{2}R\left(\frac{1}{c} + \frac{1}{1-c}\right)_{T=T_c} - N_A\omega'(T)_{T=T_c} \cong 2R \tag{3.67}$$

with the last equality only valid for $\omega'(T)_{T=T_c} \ll k_B$, where

$$\omega'(T)_{T=T_c} = 4\pi N_A\left(\int_0^{+\infty} r^2\frac{\partial}{\partial T}\left(n(T)\nu(r,T)\right)dr\right)_{T=T_c} \tag{3.68}$$

and

$$\gamma^R = \frac{1}{4!}\left(\left(g_0^R\right)''''\right)_{T=T_c} = \frac{4}{3}RT_c \tag{3.69}$$

At critical condition, $\chi = 2$. From Eq 3.20, the interfacial free energy becomes

$$\begin{aligned}
\sigma^R = 2n\int_{c_\alpha}^{c_\beta}\left(\frac{K}{2}\Delta g^R(c)\right)^{1/2}dc &= 2n\int_{c_\alpha}^{c_\beta}\left(\frac{1}{2}RT\chi\lambda^2\Delta g^R(c)\right)^{1/2}dc \\
&= \sqrt{2}n\lambda RT\int_{c_\alpha}^{c_\beta}\left(\chi\frac{\Delta g^R}{RT}\right)^{1/2}dc
\end{aligned} \tag{3.70}$$

For temperature in the vicinity of T_c, by Eq 3.30, the interfacial free energy is simply

$$(\sigma^R)_{T\sim T_c} = 2nRT_c\lambda\left(1 - \frac{N_A\omega'(T)_{T=T_c}}{2R}\right)^{3/2}\left(\frac{T_c - T}{T_c}\right)^{3/2} \tag{3.71}$$

The interfacial thickness can also be obtained by plugging the values of the parameters K and β (Eq 3.67, Eq 3.63) into the expression Eq 3.37.

3.3 ATPS Interfacial Thickness

In this section, we would like to study how diffuse the interface between the DEX-rich phase and PEG-rich phase is by approximately evaluating the interfacial thickness. Firstly, the mathematical expression for the total free energy of a ternary mixture [25] can be obtained by the same argument as what Cahn and Hillard did for a binary system. In the following context, PEG, DEX and water are denoted by 1, 2 and 3 respectively. The free energy for a ternary mixture is:

$$G = n_\Delta \int_V g_0(c_1, c_2) + \frac{K_1}{2}(\nabla c_1)^2 + K_{12}(\nabla c_1)(\nabla c_2) + \frac{K_2}{2}(\nabla c_2)^2 dV \tag{3.72}$$

where n_Δ represents the molar density (mol/m^3), $g_0(c_1, c_2)$ represents the free energy per mole of a uniform mixture of volume fraction $(c_1, c_2, 1 - c_1 - c_2)$ and c_1 and c_2 represent the volume fraction of PEG and DEX[6]. One possible option is the Flory-Huggins expression [5]:

$$\begin{aligned} g_0(c_1, c_2) = RT(&\frac{c_1}{N_1} lnc_1 + \frac{c_2}{N_2} lnc_2 + (1 - c_1 - c_2)ln(1 - c_1 - c_2) \\ &+ \chi_{12}c_1c_2 + \chi_{13}c_1(1 - c_1 - c_2) + \chi_{23}c_2(1 - c_1 - c_2)) \end{aligned} \tag{3.73}$$

where N_1 and N_2 represents respectively the number of monomers of the two polymers.

The physical data that are used for analysis is summarized in the following table:

The Flory-Huggins parameters [34] are

$$\chi_{12} = \frac{245}{RT} \quad \chi_{13} = \frac{100}{RT} \quad \chi_{23} = \frac{0}{RT} \tag{3.74}$$

---

[6] In the derivation of the Cahn Hilliard theory (Section 3.2), c represents the mole fraction. In fact, if you define c to be the volume fraction, the derivation of Section 3.2 does not change. In order to be consistent with the parameter definitions by Ariyapadi and Nauman [5], c will represent volume fraction in the calculation of interfacial thickness that follows.

Properties	PEG(1)	DEX(2)
Molecular Weight	8000	500,000
Monomer Weight	44	162
Number of monomers	180	3086
Radius of Gyration	$R_{G_1} = 3nm$	$R_{G_2} = 15nm$

Table 3.1: Physical Data for PEG and DEX

Based on the density measure of PEG and DEX solutions [2][17], the volumes of the PEG and DEX monomer are calculated to be around $64\mathring{A}^3$ and $164\mathring{A}^3$ respectively (The corresponding densities are $1161kg/m^3$ and $1645kg/m^3$). The molecular volume of water is around $30\mathring{A}^3$[7]. Therefore, the monomer volumes of DEX and PEG are approximately five times and two times larger than that of a water molecule. We can see that the monomer sizes of the two polymers are different from each other and are different from the size of a water molecule. As a result, some theoretical treatments are not able to accurately describe this nonuniform character, in particular the Flory-Huggins theory. However, this project aims to get an approximative caculation of the interface thickness in order to get a rough idea of its length scale. From the theoretical treatment of Ariyapadi and Nauman [5], the gradient energy parameters can be expressed as follows:

$$K_1 = RT\frac{R_{G_1}^2}{3}\left(\chi_{13} + \frac{1}{N_1c_1} + \frac{1}{1-c_1-c_2}\right)$$

$$K_2 = RT\frac{R_{G_2}^2}{3}\left(\chi_{23} + \frac{1}{N_2c_2} + \frac{1}{1-c_1-c_2}\right)$$

$$K_{12} = RT\left(\frac{R_{G_1}^2}{6}\left(\chi_{13} - \chi_{12} + \frac{1}{N_1(1-c_1-c_2)}\right) + \frac{R_{G_2}^2}{6}\left(\chi_{23} - \chi_{12} + \frac{1}{N_2(1-c_1-c_2)}\right)\right) \tag{3.75}$$

---

[7] Since the molar volume of water is $v = 18 \times 10^{-6}m^3/mol$, the molecular volume is approximately $v/N_A = 18 \times 10^{-6}/(6.02 \times 10^{23}) = 30 \times 10^{-30}m^3$. Hence, $n_{Delta} = 1/v = 5.6 \times 10^5$

According to the formulation of Cahn and Hilliard [8], the specific surface free energy for an unconfined fluid domain is minimized when the Δg term and the concentration gradient term are equal (Eq 3.19). It can be proved that this condition still holds true for a ternary polymer-polymer-solvent system. The specific interfacial free energy for a planar interface is defined as

$$\sigma = n_\Delta \int_{-\infty}^{+\infty} \left(\Delta g(c_1, c_2) + \frac{K_1}{2}(\nabla c_1)^2 + K_{12}(\nabla c_1)(\nabla c_2) + \frac{K_2}{2}(\nabla c_2)^2 \right) dx \tag{3.76}$$

where $\Delta g(c_1, c_2) = g_0(c_1, c_2) - c_1\mu_1 - c_2\mu_2 - (1 - c_1 - c_2)\mu_3$ with μ_1, μ_2 and μ_3 as the respective chemical potentials of the three species in a uniform mixture of volume fractions $(c_1^\alpha, c_2^\alpha, 1 - c_1^\alpha - c_2^\alpha)$. For a planar interface, $\nabla = d/dx$. Eq 3.76 can be written in an alternative form,

$$\sigma = n_\Delta \int_{-\infty}^{+\infty} \left(\Delta g(\overrightarrow{c}) + \frac{1}{2} \nabla \overrightarrow{c} \otimes \nabla \overrightarrow{c} : \begin{pmatrix} K_1 & K_{12} \\ K_{12} & K_2 \end{pmatrix} \right) dx \tag{3.77}$$

where

$$\overrightarrow{c} = \begin{pmatrix} c_1 \\ c_2 \end{pmatrix} \tag{3.78}$$

At equilibrium, the Euler-Lagrange condition has to be satisfied, i.e.,

$$\frac{\partial I}{\partial \overrightarrow{c}} = \frac{d}{dx} \left(\frac{\partial I}{\partial \nabla \overrightarrow{c}} \right) \tag{3.79}$$

with I represents the integrand of Eq 3.77. Since I does not explicitly depend on x, the Euler-Lagrange condition can be written as (Beltrami Identity)

$$\frac{d}{dx} \left(I - (\nabla \overrightarrow{c}) \cdot \left(\frac{\partial I}{\partial \nabla \overrightarrow{c}} \right) \right) = 0 \tag{3.80}$$

where

$$\frac{d}{dx} = \frac{\partial}{\partial x} + \frac{\partial \overrightarrow{c}}{\partial x} \frac{\partial}{\partial \overrightarrow{c}} + \frac{\partial^2 \overrightarrow{c}}{\partial x^2} \frac{\partial}{\partial (d\overrightarrow{c}/dx)} \tag{3.81}$$

Hence,

$$I - (\nabla \overrightarrow{c}) \cdot \left(\frac{\partial I}{\partial \nabla \overrightarrow{c}} \right) = constant \tag{3.82}$$

With the boundary condition that $\Delta g(\overrightarrow{c})$ and $d\overrightarrow{c}/dx$ tend to zero as x tends to infinity,

$$I - (\nabla\overrightarrow{c}) \cdot \left(\frac{\partial I}{\partial \nabla \overrightarrow{c}}\right) = 0 \tag{3.83}$$

Since I represents the integrand of Eq 3.77,

$$\frac{\partial I}{\partial \nabla \overrightarrow{c}} = \begin{pmatrix} K_1 & K_{12} \\ K_{12} & K_2 \end{pmatrix} \cdot (\overrightarrow{c}) \tag{3.84}$$

and therefore

$$(\overrightarrow{c}) \cdot \frac{\partial I}{\partial \nabla \overrightarrow{c}} = (\overrightarrow{c}) \cdot \begin{pmatrix} K_1 & K_{12} \\ K_{12} & K_2 \end{pmatrix} \cdot (\overrightarrow{c}) \tag{3.85}$$

Hence, Eq 3.83 would become

$$\Delta g(\overrightarrow{c}) = \frac{1}{2}\nabla\overrightarrow{c} \otimes \nabla\overrightarrow{c} : \begin{pmatrix} K_1 & K_{12} \\ K_{12} & K_2 \end{pmatrix} \tag{3.86}$$

In other words,

$$\sigma = 2n_{\Delta} \int \frac{K_1}{2}\left(\frac{dc_1}{dx}\right)^2 + K_{12}\left(\frac{dc_1}{dx}\right)\left(\frac{dc_2}{dx}\right) + \frac{K_2}{2}\left(\frac{dc_2}{dx}\right)^2 dx \tag{3.87}$$

Diamond et al [13] (Table 1 (F)) have experimentally determined the partition of the two macromolecules in the two phases. Their experimental data for PEG 8000 and DEX 500,000 are used here for a rough calculation. The partitioning of the two molecules is summarized in the following table.

Ryden and Albertsson [56] have determined the interfacial tension between the two phases by the method of rotating drops for an overall composition of 5.2% DEX and 3.8% PEG to be around 2 $\mu N/m$ [8]. In addition, the composition profiles of the

---

[8] Although PEG of molecular weight of 6000-7500 is used in the experiment of Ryden, the interfacial tension they obtained should not differ significantly from that for PEG 8000. The difference should be within a factor of 2. This can be verified by the experiments of Forciniti et al [18]

	Total	Bottom(α) %wt	Top(β) %wt	Bottom(α) %vol	Top(β) %vol
DEX	5.2	9.46	1.05	0.060	0.006
PEG	3.8	1.85	5.70	0.017	0.050
Water	91	88.64	93.32	0.924	0.944

Table 3.2: Partitioning of PEG and DEX in the aqueous two phases. $\%wt$ means weight percentage and $\%vol$ means volume fraction.

two polymers are assumed to be the same and vary in space as a hyperbolic tangent function, i.e.,

$$c_i = c_i^\alpha + \frac{c_i^\beta - c_i^\alpha}{2}\left(1 + tanh\left(\frac{x}{l}\right)\right) \tag{3.88}$$

The interfacial thickness is defined as l according to Cahn and Hilliard [8]. In fact, it would be better if the composition profiles of the two polymers are characterized by two hyperbolic tangent functions with two characteristic lengths, l_1 and l_2. However, in the framework of this project, one single characteristic length is assumed just to find out a rough value for the interfacial thickness. The numerical method is trial-and-error by constantly changing the value of l until the calculated interfacial tension is close to the experimental value with an error less than $\pm 5\%$ of the experimental value. The interfacial thickness l is found to be around $3\mu m$ for an overall composition of 5.2% DEX and 3.8% PEG (The corresponding interfacial tension is around 2 $\mu N/m$). According to Ryden and Albertsson [56], interfacial tension less than 0.5 $\mu N/m$ is obtained for even lower polymer concentration. By a similar argument, it is found that l can be as thick as $5\mu m$. The detailed Matlab code for calculation is in Table 3.3.

Remark:

By rough calculation above, we find that the interface can be as thick as 1 micron for compositions near the coexistence line (Figure 2.5(b)). If the string-like filaments

(Figure 2.4(e)) are further sheared to smaller scales, it is possible to have overlap between two interfaces. In addition, under such circumstances, the fluctuation of the interface can no longer be neglected and hence needs to be taken into account for more detailed studies.

Table 3.3: Matlab Code for Interface Thickness Calculation

```
function f = interfacialthickness
% The two polymers are assumed to have the same composition profile.
% The profile is assumed to have a shape of tanh(x)
R = 8.314; T = 298;k_B = 1.3806504e-23;
chi_12=245/(R*T); chi_13 = 100/(R*T); chi_23 = 0;
N1 = 180; N2 = 3086; R_G1 = 3; R_G2 = 15;
c_dex1 = 0.046106; c_peg1 = 0.022688; c_h2o1 = 0.931205; c_dex2 = 0.011095; c_peg2
= 0.042869246; c_h2o2 = 0.946036;
% c_dex1 = 0.059877; c_peg1 = 0.016586; c_h2o1 = 0.923537; c_dex2 = 0.006460;
c_peg2 = 0.049673909; c_h2o2 = 0.943866;
% Ryden et al
% c_dex1 =0.061375; c_peg1 = 0.014982; c_h2o1 =0.923643; c_dex2 = 0.004857;
c_peg2 = 0.051290485; c_h2o2 = 0.943853;
% Diamond et al
%%%%%%%%%%%%%%%%%%%
% Change the value of l until the interfacial tension f matches the experimental
value.
%%%%%%%%%%%%%%%%%%%
l = 5000; % interfacial thickness in nm.
l_1 = l;
l_2 = l;
syms c1 c2 x k1 k2 k12
% 1: PEG; 2: DEX
```

```
c1 = c_peg1 + (c_peg2-c_peg1)/2*(1+tanh(x./l_1));
c2 = c_dex1 + (c_dex2-c_dex1)/2*(1+tanh(x./l_2));
k1 = R_G12̂/3*(chi_13 + 1/N1/c1 + 1/(1-c1-c2));
k2 = R_G22̂/3*(chi_23 + 1/N2/c2 + 1/(1-c1-c2));
k12 = R_G12̂/6*(chi_13 - chi_12 + 1/N1/(1-c1-c2)) + R_G22̂/6*(chi_23-chi_12 + 1/N2/(1-c1-c2));
c1_diff = diff(c1,x);
c2_diff = diff(c2,x);
grad_erg = k1/2*(c1_diff)2̂ + k12*(c1_diff)*(c2_diff) + k2/2*(c2_diff)2̂;
surf_ener = k_B*T/(30e-30)*int(grad_erg,x,-3*l,3*l)*10(̂-9);
f = eval(surf_ener); % N/m
```

Chapter 4

Hydrodynamics

In this chapter, both the classical and thermodynamical approaches for the modelling of multiphase flows will be summarized. The existing theoretical and experimental studies on the breakup of drops in flows are to be discussed, which will help with the understanding of the morphologies of our microfluidic ATPS. By drawing an analogy with the previous experimental studies, we will determine the critical capillary numbers for the transitions between different morphology regions. Moreover, the application of Canny Edge Algorithm to the images of the droplets shows high degree of anisotropy. To capture more quantitative information about the droplets, Fast Fourier Transform is employed to find out the characteristic sizes of the elongated fluid filaments at different flow speeds. We find that the sizes from FFT are well larger than the R_{crit} defined by Khakhar and Ottino [37], representing the critical filament radius at which the surface disturbance starts to grow and eventually leads to breakup. From this point of view, the existing theory is consistent with our experimental observations. At last, the effect of chaotic mixing enhanced by the incorporation of the meandering section will be discussed.

4.1 Classical Navier-Stokes Approach

4.1.1 Interface

The science of interfaces was born at the beginning of the 19th century, when Pierre Simon de Laplace and Thomas Young started to investigate the interfacial energy between two immiscible fluids [70][12]. The classical definition for an interface is a definitive boundary of infinitely thin thickness that separates two fluids of different chemical natures (Figure 4.1). They found the pressure difference across an interface, ΔP, called the Young-Laplace pressure

$$\Delta P = 2\sigma C \tag{4.1}$$

where σ is the interfacial energy (N/m) and C is the mean curvature at the interface. For a spherical interface of radius R, $C = 1/R$. For a three-dimensional curve $r = r(z)$ with an axial symmetry, its mean curvature is given as follows [11].

$$2C = -\frac{\ddot{r}}{(1+\dot{r}^2)^{\frac{3}{2}}} + \frac{1}{r(1+\dot{r}^2)^{\frac{1}{2}}} \tag{4.2}$$

An alternative derivation is provided in Appendix D. If $\dot{r}$ is very small, the mean curvature can be approximated by $2C = -\ddot{r} + 1/r$.

From the point of view of continuum mechanics, when we deal with microfluidic systems, the inertial term in the Navier-Stokes equation can be neglected, making the system linear. However, it is the presence of interfaces that is account for the non-linearity of the multiphase system we often encounter in microfluidics. Firstly, we define some dimensionless parameters that will facilitate our following discussions.

$$Re = \frac{\rho U D}{\eta}$$

$$Bo = \frac{\rho g D^2}{\sigma}$$

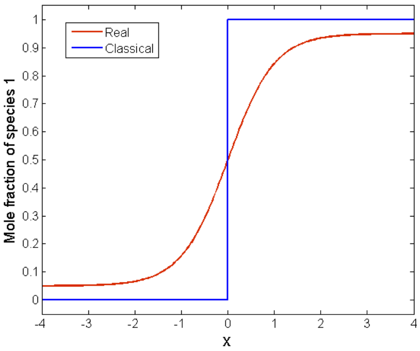

Figure 4.1: Illustration of an interface of a binary system for a classical treatment and a real one.

$$Ca = \frac{\eta U}{\sigma} \tag{4.3}$$

where ρ is density, U is the characteristic velocity of the fluid, D is the characteristic size of the flow domain and η is the viscosity of the fluid. The Reynolds number (Re) describes the weighting of inertial effect relative to viscous effect, whereas the capillary number (Ca) reveals the weighting of viscous force relative to surface tension. Similarly, the Bond number (Bo) compares gravity with interfacial force. For flows in a microfluidic channel, the typical Re value is 10^{-2}, which means viscous force dominates as compared to inertia. For a normal multiphase microfluidic system, the capillary number is around 10^{-6}, which represents that the surface tension is much more important than viscous force. However, Ca can be as big as $0.01 \sim 1$ for an aqueous two-phase system with very low interfacial tension.

4.1.2 Classical Modeling

The classical modeling for a multiphase flow is based on the theory of continuum mechanics. Since the typical Reynolds number is small in microfluidic system, the inertia term , $\rho\mathbf{v}\nabla\mathbf{v}$, can be neglected. Hence, the linearized Navier-Stokes equation for incompressible fluids is expressed as

$$\rho\frac{\partial\mathbf{v}}{\partial t} = -\nabla p_i + \eta_i \Delta\mathbf{v}_i$$

$$\nabla\cdot\mathbf{v}_i = 0 \tag{4.4}$$

with boundary conditions

$$\mathbf{v}_i(\partial\Omega_w) = 0$$

$$p_i(\partial\Omega_I) - p_j(\partial\Omega_I) = \sigma_{(ij)}\nabla\cdot\mathbf{n}(\partial\Omega_I) \tag{4.5}$$

where i represents the fluid i, $\partial\Omega_w$ means at solid boundaries, $\partial\Omega_I$ means at the interface between two fluids, $\sigma_{(ij)}$ is the interfacial tension between the fluid i and j, $\mathbf{n}$ is the normal vector of the interface, p is the hydrodynamic pressure, i.e., $p = p' - \rho g z$ and p' is the total pressure.

4.1.3 Literature Review: Dynamics of Fluid Threads and Drops

Thread Breakup at Rest: Plateau-Rayleigh Instability

Historically, Plateau [50] found from the experiments by Savart that a falling water jet breaks up into drops with a fast-growing wavelength($\sim 4.38D$), where D is the diameter of the cylindrical jet (Figure 4.2).

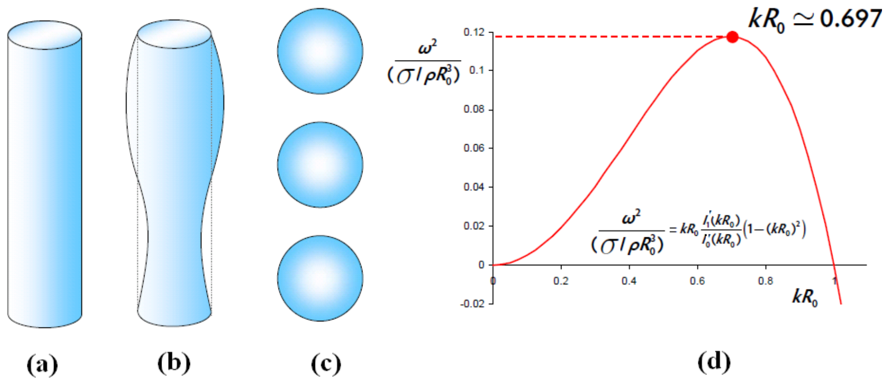

Figure 4.2: Illustration of the Plateau-Rayleigh instability. (a) A cylindrical jet (b) Undulation at the surface (c) Liquid jet breaks up into droplets (d) dispersion relation by small perturbation analysis for inviscid fluid jet (Source: Professor Michiel T. Kreutzer), where the $I_0'(x)$ and $I_1'(x)$ are the modified Bessel functions of the first kinds

Later in 1878, Lord Rayleigh [53] theoretically showed that the interfacial area of a cylindrical jet increases when the surface undulates with a wavelength larger than πD. Detailed perturbation analysis has been carried out by neglecting the viscous and body forces of the liquid jet (Appendix B.1). This can only be valid if the Ca and Bo are small with respect to unity. A dispersion relation (Figure 4.2(d)) can eventually be achieved

$$\omega^2(\kappa) = \frac{\sigma}{\rho a^3} \frac{(\kappa^2 a^2 - 1) i\kappa a I_1(i\kappa a)}{I_0(i\kappa a)} \tag{4.6}$$

where σ is the surface tension, ω is the angular frequency of the undulatory disturbance, κ is the wavenumber and the $I_0(x)$ and $I_1(x)$ are the Bessel functions of the first kinds. This dispersion relation shows a maximum which corresponds to the fastest growing wavelength.

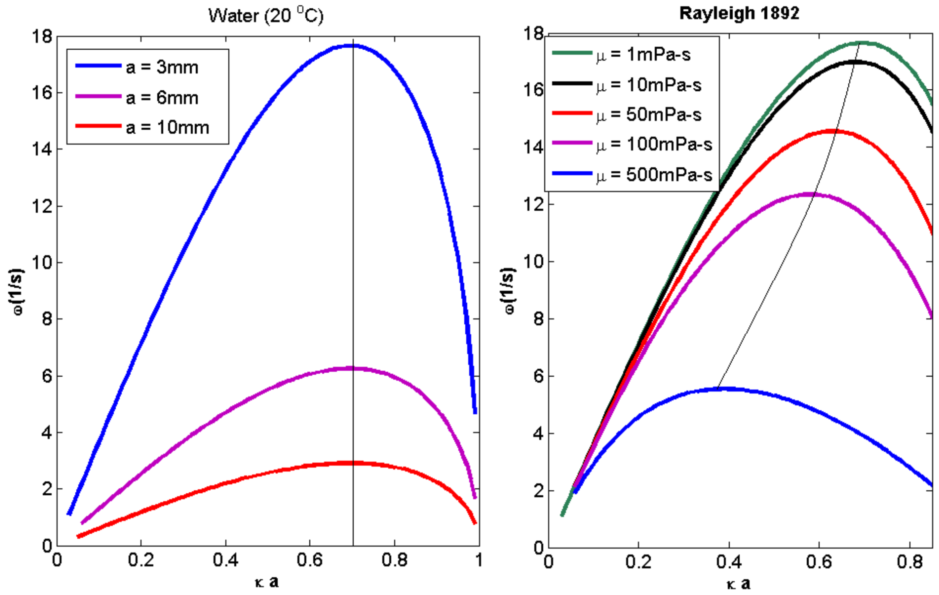

Figure 4.3: (left) Dispersion relation by Rayleigh 1892($\omega = f(\kappa a)$) for water jets of different radii a at 25^oC. (right) for various viscosities. The surface tension in both graphs is 72mN/m and the density is $1g/cm^3$. The black thin line represents the fast growing modes

In 1892, Rayleigh [54] theoretically found out the dispersion relation for viscous fluids by neglecting the kinetic energy ($\sim U^2$):

$$det \begin{pmatrix} Q(\omega, \kappa a) & Z(\omega, \kappa a) \\ 2\kappa^2 I_0'(i\kappa a) & (\kappa_1^2 + \kappa^2) I_0'(i\kappa_1 a) \end{pmatrix} = 0 \tag{4.7}$$

where $Q(\omega, \kappa a)$ and $Z(\omega, \kappa a)$ are defined by Eq B.74 and Eq B.75. The dispersion relation is plotted in Figure 4.3 for water jets of different radii at 25^oC and for various viscosities. We can see clearly that the fast growing mode κa_{max} does not depend on the radius of the liquid jet. However, this is just an artificial result of the Rayleigh's model and it is not true in reality. For large liquid jet, the Reynold's number can become so significant that the kinetic energy cannot be neglected and the Laplace pressure cannot be approximated by Eq B.49 in Appendix B, which makes the analysis of Rayleigh [54] less valid. In addition, we observe that as the viscosity increases, the fast growing wave number κ tends to zero, which corresponds to an infinitely large wavelength. This is to say that the liquid jet of very high viscosity will not break up. If the viscous effect dominates ($\rho \to 0$), the dispersion relation becomes

$$i\omega = \frac{\sigma(\kappa^2 a^2 - 1)}{2\mu a \kappa^2 a^2 \left(I_0^2(i\kappa a)/I_0'^2(i\kappa a) + 1 + 1/(\kappa^2 a^2) \right)} \tag{4.8}$$

However, the analysis by Rayleigh [53][54] only consider liquid jets exposed to vacuum ($\mu'/\mu \to \infty$), where the superscript $'$ represents the fluid jet. In 1935, S. Tomotika proposed some improvement in two consecutive papers by considering viscous liquid threads surrounded by another stationary viscous fluid [64] and by another viscous fluid which is extending at a uniform rate [65]. The first paper by Tomotika is very similar to the paper by Rayleigh in 1892 [54]. The only differences are the boundary conditions. The boundary condition for viscous liquid jet immersed in another viscous liquid:

The general dispersion relation obtained by Tomotika is

$$det \begin{pmatrix} \widetilde{I}_1(\kappa a) & \widetilde{I}_1(\kappa_1' a) & \widetilde{K}_1(\kappa a) & \widetilde{K}_1(\kappa_1 a) \\ \kappa a \widetilde{I}_0(\kappa a) & \kappa_1' a \widetilde{I}_0(\kappa_1' a) & -\kappa a \widetilde{K}_0(\kappa a) & -\kappa_1 a \widetilde{K}_0(\kappa_1 a) \\ 2\frac{\mu'}{\mu}\kappa^2 \widetilde{I}_1(\kappa a) & \frac{\mu'}{\mu}(\kappa^2 + (\kappa_1')^2)\widetilde{I}_1(\kappa_1' a) & 2\kappa^2 \widetilde{K}_1(\kappa a) & (\kappa^2 + \kappa_1^2)\widetilde{K}_1(\kappa_1 a) \\ F_1 & F_2 & F_3 & F_4 \end{pmatrix} = 0 \tag{4.9}$$

1 The difference in normal stress at the surface is equal to the Laplace pressure:

$$\sigma_{rr}(r=a) - \sigma'_{rr}(r=a) = 2C(r=a)\sigma$$

2 There is no singularity at $r = 0$

3 The velocity of the surround fluid at infinity is zero: $\mathbf{v}(r = +\infty) = 0$

4 There is no slip at the surface: $v_r(a) = v'_r(a)$

5 The tangential stress at the surface is continuous: $\sigma'_{zr}(a) = \sigma_{zr}(a)$

where the functions F_1, F_2, F_3 and F_4 are defined by Eq C.1 in Appendix C and $\widetilde{I}_i$ and $\widetilde{K}_i$ are the modified Bessel function (Figure B.1). If the inertial effect is negligible, i.e., $\rho \to 0$ and $\rho' \to 0$, the general dispersion relation (Eq 4.9) simplifies to

$$i\omega = \frac{\omega}{2\mu a}(1 - \kappa^2 a^2)\Phi(\kappa a) \tag{4.10}$$

where $\Phi(x)$ is defined by Eq C.2 in Appendix C.

In 1996, Howard A. Stone and Michael P. Brenner [59] directly included a jump of normal stress to the Stokes equation[1] to account for the Laplace pressure. Then, they empolyed Hankel transform with appropriate boundary conditions and they arrived at the same expression as Tomotika's general result (Eq 4.9) with $\mu'/\mu = 1$ for the case of a capillary thread immersed in another viscous fluid of infinitely large volume:

$$\omega(\kappa) = \frac{\sigma}{\mu a}\kappa^2\left(1 - (\kappa a)^2\right)\left(\widetilde{I}_1(\kappa a)\widetilde{K}_1(\kappa a) + \frac{\kappa a}{2}\left(\widetilde{I}_1(\kappa a)\widetilde{K}_0(\kappa a) - \widetilde{I}_0(\kappa a)\widetilde{K}_1(\kappa a)\right)\right) \tag{4.11}$$

With a different set of boundary conditions, they also obtained the dispersion relation for a thread immersed in another cylinder of viscous fluid, with 1 and 2

---

[1] Stokes equation is valid for fluid flows of negligible inertia

representing the inner and outer cylinders respectively.

$$\left(\omega - \frac{\kappa^2\sigma_1}{a_1\mu}\left(1-(\kappa a_1)^2\right)\Lambda(a_1,a_1)\right)\left(\omega - \frac{\kappa^2\sigma_2}{a_2\mu}\left(1-(\kappa a_2)^2\right)\Lambda(a_2,a_2)\right)$$

$$= \frac{\kappa^4\sigma_1\sigma_2}{a_1a_2\mu^2}\left(1-(\kappa a_1)^2\right)\left(1-(\kappa a_2)^2\right)\Lambda(a_1,a_2)^2 \tag{4.12}$$

with

$$\Lambda(b,c) = \int_0^\infty \frac{sI_1(sb)I_1(sc)}{(s^2+\kappa^2)^2}ds \tag{4.13}$$

Since the investigation of Rayleigh, there has been active research on the breakup of liquid threads in another quiescent liquid. More recent publications include notably [10][38][40][47].

Table 4.1: Summary of the Plateau-Rayleigh Instability

	Assumption	Paper	Dispersion Relation
General thread in another liquid	$U^2 \cong 0$	[64]	Eq 4.9
General thread in vacuum	$\mu'/\mu \to \infty,\ \rho \to 0$	[54]	Eq 4.7
Inviscid thread in vacuum	$\mu, \mu' \to 0,\ \rho \to 0$	[53]	Eq 4.6
Viscous thread in another liquid	$\rho, \rho' \to 0$	[64]	Eq 4.10
Viscous thread in vacuum	$\rho, \rho' \to 0, \mu'/\mu \to \infty$	[54]	Eq 4.8
Viscous thread in equally viscous liquid	$\rho,\ \rho' \to 0,\ \mu'/\mu = 1$	[59]	Eq 4.11
Viscous thread in equally viscous cylinder	$\rho, \rho' \to 0,\ \mu'/\mu = 1$	[59]	Eq 4.12

Note: Superscript ' represents the inner liquid thread. Viscous thread means the viscous effect dominates and inviscid thread means the inertial effect dominates

Thread Breakup in Flow

Other than the previous investigations on thread breakup in a quiescent fluid matrix, the breakup of liquid threads in flow has also been theoretically studied. The first paper is by Tomotika in 1936 [65]. He studied the breakup of liquid thread in an elongational flow, i.e.,

$$\mathbf{v}_r = -\frac{1}{2}Gr \qquad \mathbf{v}_z = Gz \tag{4.14}$$

The starting equations are Stokes equation in terms of stream function ψ and the continuity equation for incompressible fluids. The boundary conditions used are very similar to his paper on thread breakup at rest [64]. One additional condition is imposed on top of the three boundary conditions specified in Appendix B.2.1: the velocity is continuous at the surface of the thread.

However, Tomotika did not take into account the varicosity of the surface when he specified the boundary conditions at the surface. In 1975, T. Mikami, R. G. Cox and S. G. Mason [44] analyzed the problem by the theory of perturbation in a systematic matter. They considered the varicosity of the thread surface as a perturbation to the leading-order flow $\sim O(1)$, which is just an elongational flow of a liquid thread without surface varicosity. The velocity profiles for the inner and the surrounding liquids to the leading order are both

$$(\mathbf{v}_0)_r = -\frac{1}{2}Gr \quad (\mathbf{v}_0)_\theta = 0 \quad (\mathbf{v}_0)_z = Gz \tag{4.15}$$

where the subscript 0 refers to the case without perturbation on the thread surface. Then, perturbation is introduced to the surface of the thread by

$$r = a + \epsilon\alpha_0 cos\kappa z \tag{4.16}$$

The velocity profiles for the inner liquid thread and the surround liquid are

$$\mathbf{v}' = \mathbf{v}'_0 + \epsilon\mathbf{v}'_1 \quad (r < a + \epsilon\alpha_0 cos\kappa z) \tag{4.17}$$

$$\mathbf{v} = \mathbf{v}_0 + \epsilon \mathbf{v}_1 \qquad (r > a + \epsilon\alpha_0 cos\kappa z)$$

where the superscript ' represents the inner liquid thread and the subscript 1 refers to the correction to the first order ($\sim O(\epsilon)$). The Cauchy stress tensor

$$\sigma_{ij} = (\sigma_0)_{ij} + \epsilon(\sigma_1)_{ij} \tag{4.18}$$

The boundary conditions are subsequently linearized and only the correction to the first order ($\sim O(\epsilon)$) is considered. The only difference between the analysis of Mikami et al [44] and Tomotika [65] is the boundary condition for the continuity of the tangential stress. By perturbation analysis to the first order, Mikami et al found that the continuity of the tangential stress to the first order should be expressed as

$$(\sigma_1')_{rz} + 3\eta' G\alpha_0\kappa sin\kappa z = (\sigma_1)_{rz} + 3\eta G\alpha_0\kappa sin\kappa z \tag{4.19}$$

at $r = a$ and they arrived at a growth relation a bit different from that from Tomotika (See Eq 65 in Mikami et al [44]). They also identified four dimensionless parameters (η'/η, $\sigma/(\eta a_0 G)$, Gt, $x = \kappa a$) and studied the asymptotic values for various extreme cases.

In 1986, D. V. Khakhar and J. M. Ottino [37] extended the previous works to general linear flows with asymmetric varicosity at the surface. A general linear flow is characterized by the following relation

$$\frac{dx}{dt} = \nabla\mathbf{v}\cdot\mathbf{x} \tag{4.20}$$

$\nabla\mathbf{v}$ can be diagonalized except for $\alpha = 0$ (See Eq F.1). For $\alpha \neq 0$, the deformation gradient tensor ($\widetilde{F} = \partial\widetilde{\mathbf{x}}/\partial\mathbf{X}$) is a diagonal matrix in the eigen-frame[2]. In this eigen-frame, the analysis would become similar to the previous works by Tomotika [65] and by Mikami et al [44]. Then, they introduced two perturbations: one for

---

[2] In other words, the axis of the eigen-frame are the eigenvectors of $\nabla\mathbf{v}$

the varicosity of the surface (ϵ_1) and the other to account for the asymmetry of the disturbance (ϵ_2)

$$r = a + \epsilon_1 \alpha_0 cos(\kappa z + \epsilon_2 \kappa a \beta) \tag{4.21}$$

where β specifies the non-axisymmetric phase shift of the disturbance. Perturbation analysis up to the first order ($\sim O(\epsilon_1, \epsilon_2)$) is then performed (similar to [44]). A general growth relation was obtained (Eq 9 by Khakhar and Ottino [37]).

Drop Breakup in Flow

The breakup of drops in flows is a very difficult problem in fluid mechanics and it is of great industrial interests. To date, it has been extensively studied by a large number of mathematicians, experimental and theoretical fluid physicists. The first investigation dated back to the pioneer experimental work by G. I. Taylor, who is the first one to used a four-roll mill ($\alpha = 1$) and a parallel band ($\alpha = 0$) apparatus to experimentally study the effect of flow parameters and flow types on the deformation and breakup of liquid drops [63], where the definition of α is in Appendix F. He found that there is a critical capillary number, Ca_c above which the drop breaks up.

Since then, there has been many theoretical works on the deformation and breakup of drops in linear flows. Two comprehensive review papers by A. Acrivos [1] and by Rallison [52] have summarized the majority of them. Many experimental works have also been done [55][35][20][67]. But, most of them are only limited to simple shear flows ($\alpha = 0$) and 2D elongational flows ($\alpha = 1$).

Later in 1986, B. J. Bentley and L. G. Leal experimentally studied the breakup of drops in other types of linear flows ($\alpha = 0.2, 0.4, 0.6, 0.8, 1.0$) for different viscosity ratios using a computer-controlled four-roll mill [6]. He found that the prediction from existing theories agreed well with his experimental results.

4.2 Thermodynamic Navier-Stokes-Cahn-Hilliard Approach

4.2.1 Modelling Equations

Now, we are able to write the governing equation for a binary fluid system. In the framework of this thesis, the concentration and momentum fluctuation due to thermal noise are neglected. We assume that the fluids are incompressible and Newtonian. The Navier-Stokes Equation is written as

$$\rho \frac{D\mathbf{v}}{Dt} = -\nabla p + \eta \nabla^2 \mathbf{v} + f \tag{4.22}$$

$$\nabla \cdot \mathbf{v} = 0 \tag{4.23}$$

where p is the hydrodynamic pressure and f represents the additional force due to the presence of composition gradient

$$f = \mu \nabla c(\mathbf{r}) \tag{4.24}$$

where μ represents the chemical potential (See Equation 3.13). This coupled Navier-Stoke-Cahn-Hilliard(NSCH) equation is referred as the model H in the theory of dynamic critical phenomena by P. C. Hohenberg and B. I. Halperin [28]. Alternative approaches for the derivation of the NSCH equation are available, notably by M. E. Gurtin [21][22] and by J. Lowengrub and L. Truskinovsky [39]. In addition, the local mass balance equation is

$$\frac{\partial c}{\partial t} + \mathbf{v} \cdot \nabla c + \nabla \cdot J = 0 \tag{4.25}$$

By the general Fick's Law, the flux

$$J = -D \nabla \mu \tag{4.26}$$

where D is a mobility term and depends on local composition.

Boundary conditions have to be imposed in order to solve the three partial differential equations above. Firstly, the boundary is nonslip,

$$\mathbf{v}(\partial\Omega) = 0 \tag{4.27}$$

Since none of the mixture can penetrate through the boundary, we have

$$\nabla c \cdot \mathbf{n} = 0 \tag{4.28}$$

In addition, we must have

$$\nabla \mu \cdot \mathbf{n} = 0 \tag{4.29}$$

where $\partial\Omega$ represents the boundary and $\mathbf{n}$ is the normal vector to the boundary. This condition guarentees that the flux across the boundary is not possible. The system has to minimize its total free energy inside the boundary.

4.2.2 Theoretical Solution

Since we are dealing with microfluidic systems, the Reynolds number is typical much smaller than unity. Therefore, the system is over-damped and it's legitimate to ignore the inertial term $\rho\mathbf{v}\nabla\mathbf{v}$ [7]. The Navier-Stokes equations for steady incompressible flow becomes

$$\nabla \cdot \mathbf{v} = 0 \tag{4.30}$$

$$0 = -\nabla p + \eta\nabla^2\mathbf{v} + f \tag{4.31}$$

In Fourier Space, they are expressed as

$$\mathbf{k} \cdot \widehat{\mathbf{v}}(\mathbf{k}) = 0 \tag{4.32}$$

$$0 = i\mathbf{k}\widehat{p}(\mathbf{k}) - \eta k^2 \widehat{\mathbf{v}}(\mathbf{k}) + \widehat{f}(\mathbf{k}) \tag{4.33}$$

By multiplying Equation 4.33 by $\mathbf{k}$ and using Equation 4.32, we have

$$\widehat{p}(\mathbf{k}) = \frac{i\mathbf{k}\widehat{f}(\mathbf{k})}{k^2} \tag{4.34}$$

Therefore, from Equation 4.33, we have

$$\widehat{\mathbf{v}}(\mathbf{k}) = \widehat{T}(\mathbf{k})\widehat{f}(\mathbf{k}) \tag{4.35}$$

where

$$\widehat{T}(\mathbf{k}) = \frac{1}{\eta k^2}(I - \frac{\mathbf{k} \otimes \mathbf{k}}{k^2}) \tag{4.36}$$

is the Oseen-Burgers Tensor in Fourier space. In real space, it is expressed as (Appendix A)

$$T(\mathbf{r}) = \frac{1}{8\pi\eta r}(I + \frac{\mathbf{r} \otimes \mathbf{r}}{r^2}) \tag{4.37}$$

Hence, the velocity field is

$$\mathbf{v}(\mathbf{r}) = T * f(\mathbf{r}) = \int_{R^3} T(\mathbf{r} - \mathbf{r}')f(\mathbf{r}')d\mathbf{r}' = \int_{R^3} T(\mathbf{r} - \mathbf{r}')\mu(\mathbf{r}')\nabla' c(\mathbf{r}')d\mathbf{r}' \tag{4.38}$$

where $*$ represents an operation of convolution. By substituting this expression into the local mass balance equation, we have a partial differential equation with only $c(\mathbf{r})$ as the variable:

$$\frac{\partial c}{\partial t} = D\nabla^2 \mu(c(\mathbf{r})) - \int_{R^3} \nabla c(\mathbf{r}) \cdot T(\mathbf{r} - \mathbf{r}') \cdot \mu(\mathbf{r}')\nabla' c(\mathbf{r}')d\mathbf{r}' \tag{4.39}$$

4.3 Investigation on Phase Morphologies

4.3.1 Physical Properties

In order to investigate how the transition between different morphologies occurs, we have to measure the relevant physical properties, such as viscosities and surface tensions for different compositions. Mixtures of PEG and dextran solutions of different initial compositions are allowed to phase separate in batch. The bottom phase(equilibrium dextran-rich phase) and the top phase(equilibrium PEG-rich phase) are separately taken out for viscosity measurements using AR-G2 Rheometer. They are summarized in Table 4.2 and are interpolated in Figure 4.4(a)(b). The surface tensions for different compositions are obtained from the experimental data by Ryden et al [56] and Helfrich et al [26]. These data are interpolated in Figure 4.4(c)(d) for subsequent analysis of morphology transition.

Composition $\%w/w$	η_{PEG} (Pa-s)	η_{DEX} (Pa-s)	η_c (Pa-s)	η_d (Pa-s)
4.0	0.0038	0.0136	0.0035	0.0194
5.5	0.0057	0.0250	0.0035	0.0772
6.5	0.0074	0.0346	0.0044	0.1412
7.0	0.0085	0.0402	0.0049	0.1787
7.5	0.0096	0.0473	0.0055	0.2297
8.0	0.0138	0.0732	0.0074	0.4479

Table 4.2: The viscosities of the PEG (η_{PEG}) and DEX (η_{DEX}) solutions before mixing and the viscosities of the top (η_c) and bottom phases (η_d) at equilibrium for different initial compositions. Temperature: 25 ^oC.

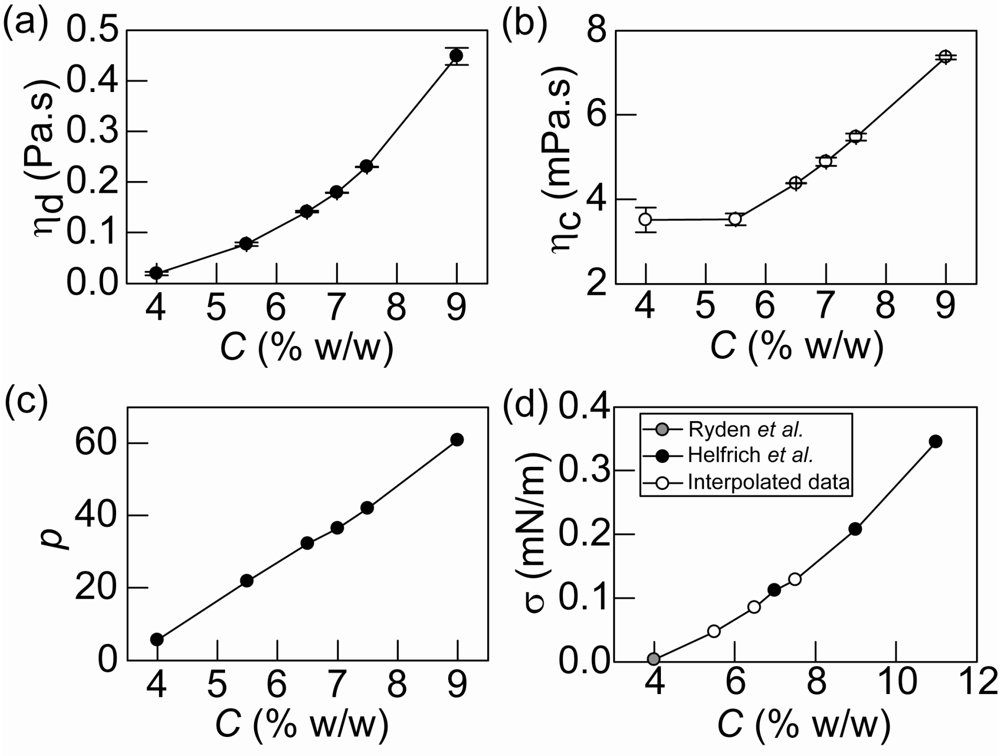

Figure 4.4: Equilibrium viscosities at (a) DEX-rich phase, η_d (b) PEG-rich phase, η_c. (c) viscosity ratio, $p(=\eta_d/\eta_c)$. (d) Interfacial tension, σ, between PEG and DEX at various compositions.

4.3.2 Investigation on Phase Morphologies

Physical Interpretation

In this project, different phase morphologies at different flow rates and compositions have been classified in Section 2.2.1. The underlying physics is simply a competition between the interfacial tension and shear stress in the aqueous droplets. At very low flow rates, the interfacial tension dominates over the shear stress and its natural tendency to minimize the surface area results in a single-lobed morphology as the static case (Figure 4.5). As the flow rate increases until the shear stress becomes comparable to the interfacial tension, the interface will be destabilized and torn apart by the shear. At high flow rates, the inner phase will be deformed to a great extent, forming reticulated phase morphology and string-like morphology for relatively low compositions as reported by Hashimoto [24]. At compositions near the critical points and at the maximum flow rate possible in our device, the aqueous two-phase droplets can become transparent at low resolutions of the microscope, forming a very stable quasi-homogenized phase as explained in Section 2.2.2. However, high anisotropic string-like filaments can still be observed at high resolutions (Figure 2.4(e)).

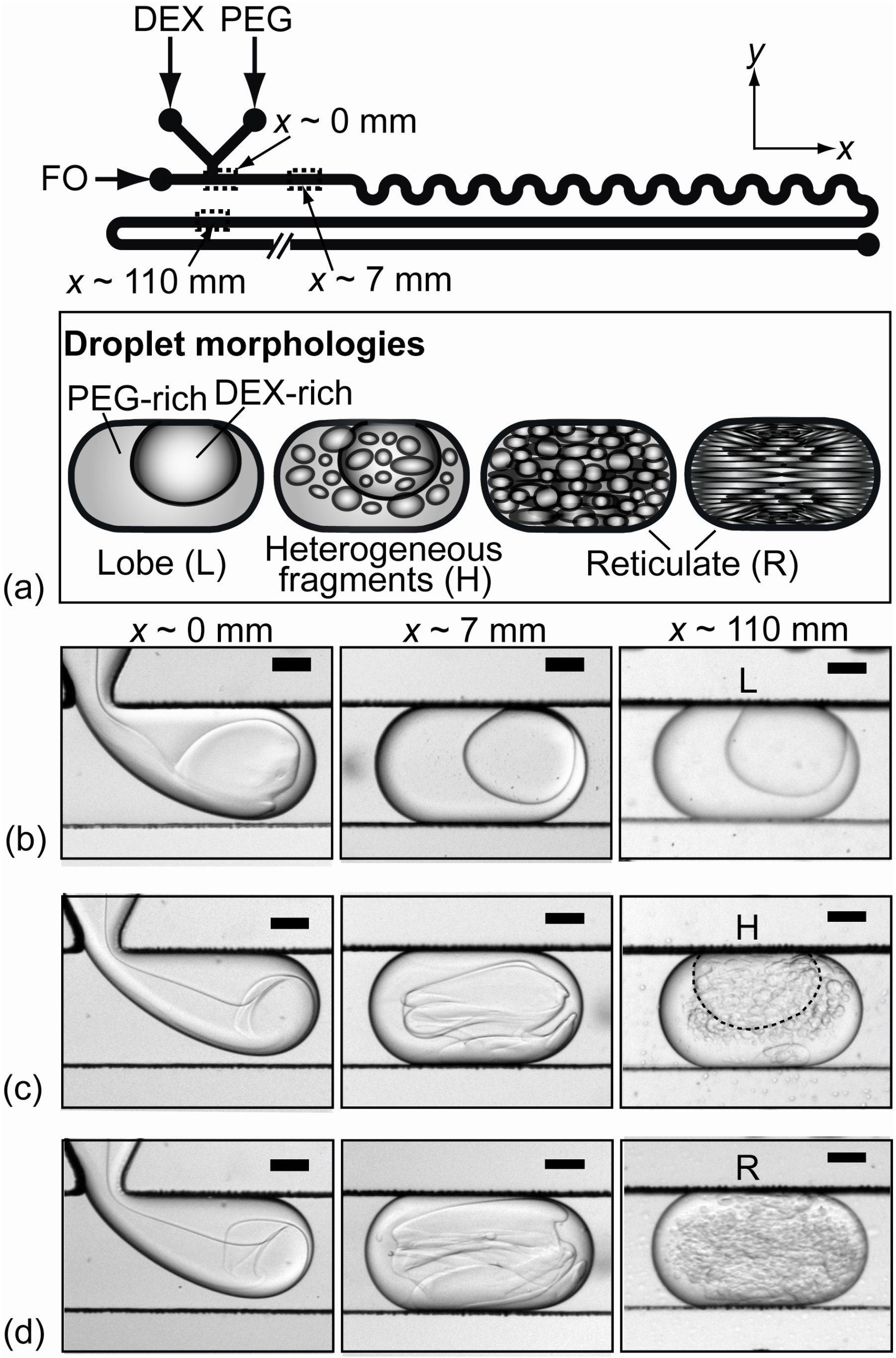

Figure 4.5: Stereomicroscopic images of ATPS droplet structures (C = 5%w/w) captured at various locations of the microchannels with increasing flow speeds (b) 0.64mm/s (c) 4.3mm/s (d) 7.5mm/s. Scale bar: 100μm

Transition Analysis

The deformation and breakup of drops in flows has been studied by many prominent researchers [63][20][6] (Section 4.13). They found that for different viscosity ratios and flow types, there is a critical capillary number above which the drop will break up. In analogy with their arguments, we also define a capillary number for the microfluidic aqueous two-phase droplet as

$$Ca = \frac{U\eta_c}{\sigma} \tag{4.40}$$

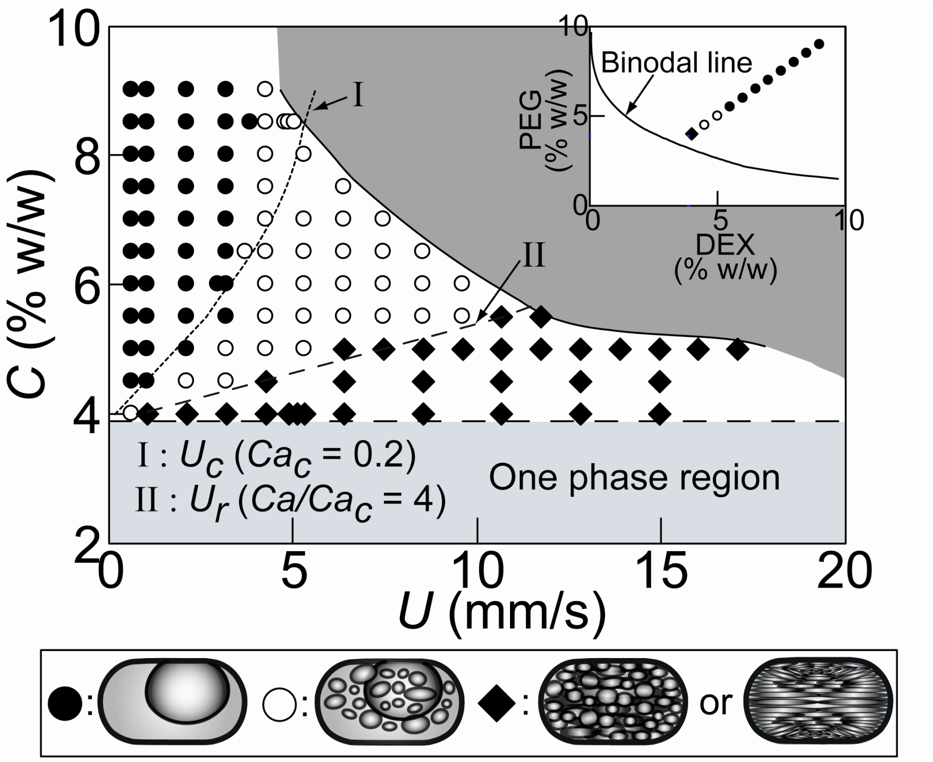

Figure 4.6: Morphology phase map. The dark gray region marks the occurrence of coflow instead of forming ATPS droplets. The light gray area is the miscible region of the two polymer solutions. Inset shows morphology variation of the ATPS droplets at a flow speed of 3.2 mm/s. The binodal line are obtained from Diamond and Hsu (1989) [13].

where η_c is the equilibrium viscosity of the outer PEG-rich phase and U is the flow speed. We also determined that the critical capillary number for the transition from the single-lobed morphology to the heterogeneously fragmented morphology, $Ca_c = 0.2$ (Dashed line I in Figure 4.6). We also found that the capillary number that characterizes the transition from the heterogeneously fragmented morphology to the reticulated morphology (Dashed line II in Figure 4.6) is $4Ca_c = 0.8$.

4.3.3 Digital Image Processing

Canny Edge Detector

In order to investigate the reticulated structure further, it is greatly desired to find out how the interface is distributed inside the aqueous droplet. Therefore, the original images from digital microscope have been analyzed by the Canny Edge Detector algorithm (Figure 4.7). From the image by post hysteresis, highly anisotropic string-like edges along the direct of the flow can be observed. Unfortunately, it is difficult to quantify the degree of randomness or orderedness in term of string-like patterns by image processing. One possible solution might be to use phase contrast microscope or to carefully measure the refractive index at different locations in the aqueous droplet since the refractive index is proportional to the concentration of the polymers [48].

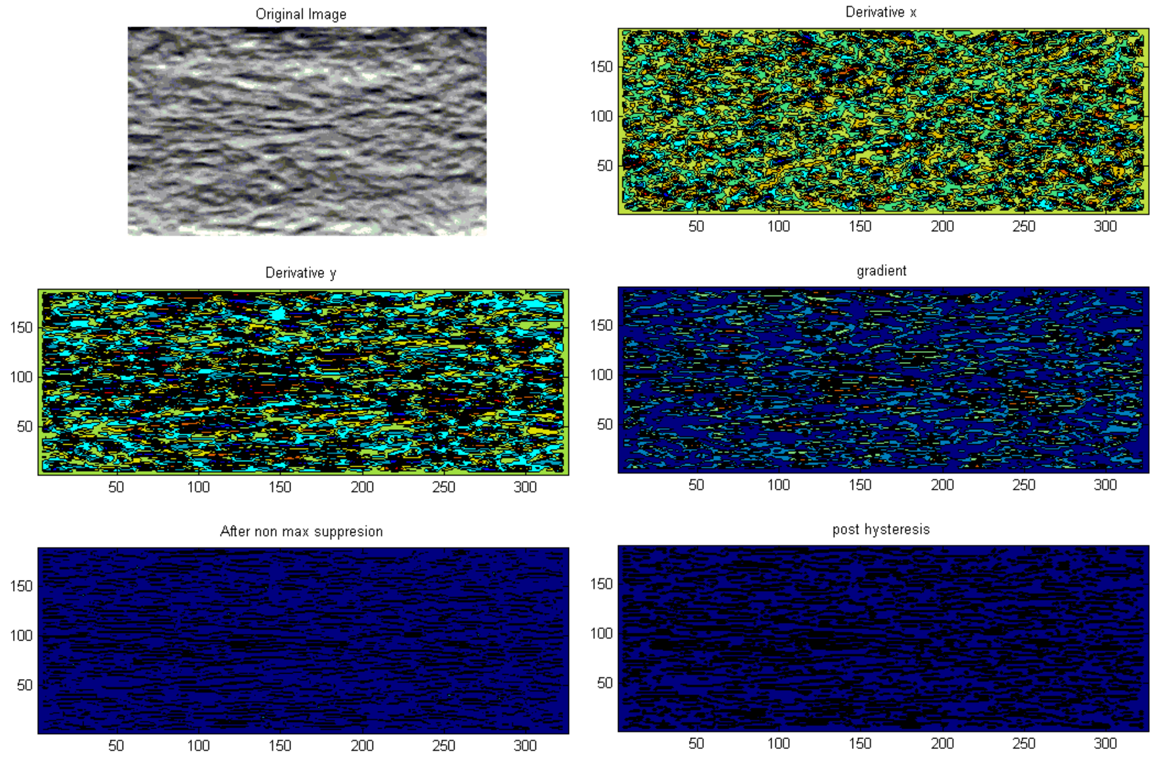
Original Image

Derivative x

Derivative y

gradient

After non max suppresion

post hysteresis

Figure 4.7: Image processed by the algorithm of Canny Edge Detector

Fast Fourier Transform

Although the treatment by Canny Edge algorithm shows the anisotropic feature of the droplet morphology, it does not give any quantitative data about the degree of anisotropy or the characteristic size of the anisotropic string-like fluid domains. Hence, 2-dimensional Fast Fourier Transform (FFT) is employed in order to find out the characteristic size of those elongated filaments, which will give us a clearer picture about the degree of anisotropy and the extent of elongation.

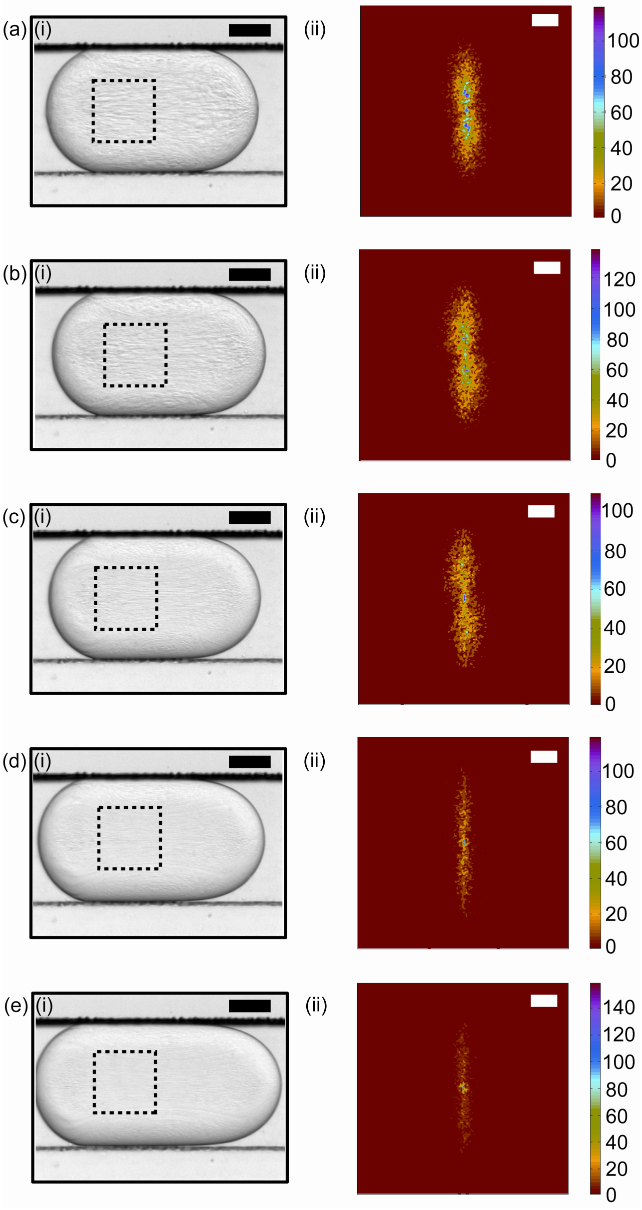

Figure 4.8: (i) Stereomicroscopic images of reticulate structures of ATPS compound drop (C = 4% w/w) captured at L $\cong$ 110 mm with total flow speeds (a) 2.1 mm/s (b) 4.3 mm/s (c) 6.4 mm/s (d) 10.7 mm/s (e) 15.0 mm/s. Scale bars represent 100 μm. The dashed squares in the original images represent the region selected for FFT. (ii) corresponding FFT results. Black scale bars represent 100 μm and white scale bars represent a frequency of 20.

Figure 4.8 shows the 2D FFT of stereomicroscopic images of ATPS droplet structures for a composition near the binodal line (4%w/w PEG and 4%w/w DEX) at different flow speeds (2.1 mm/s, 4.3 mm/s, 6.4 mm/s, 10.7 mm/s and 15.0 mm/s). The characteristic sizes of the fluid filaments at different flow speeds are extracted from the FFT results and are plotted against the flow speed (Figure 4.9). We do see a general trend of decreasing filament size with increasing flow speed. More interestingly, we also find that the characteristic size approaches to order of interfacial thickness, $l \sim 1\mu m$(Section 3.3). This gives us a general idea about the scale of the elongated fluid filaments. One would naturally ask what if we infinitely increase the flow speed. In other words, is shear stress able to homogenize the otherwise aqueous two-phase droplets at static equilibrium? This question will be investigated in details in Chapter 5.

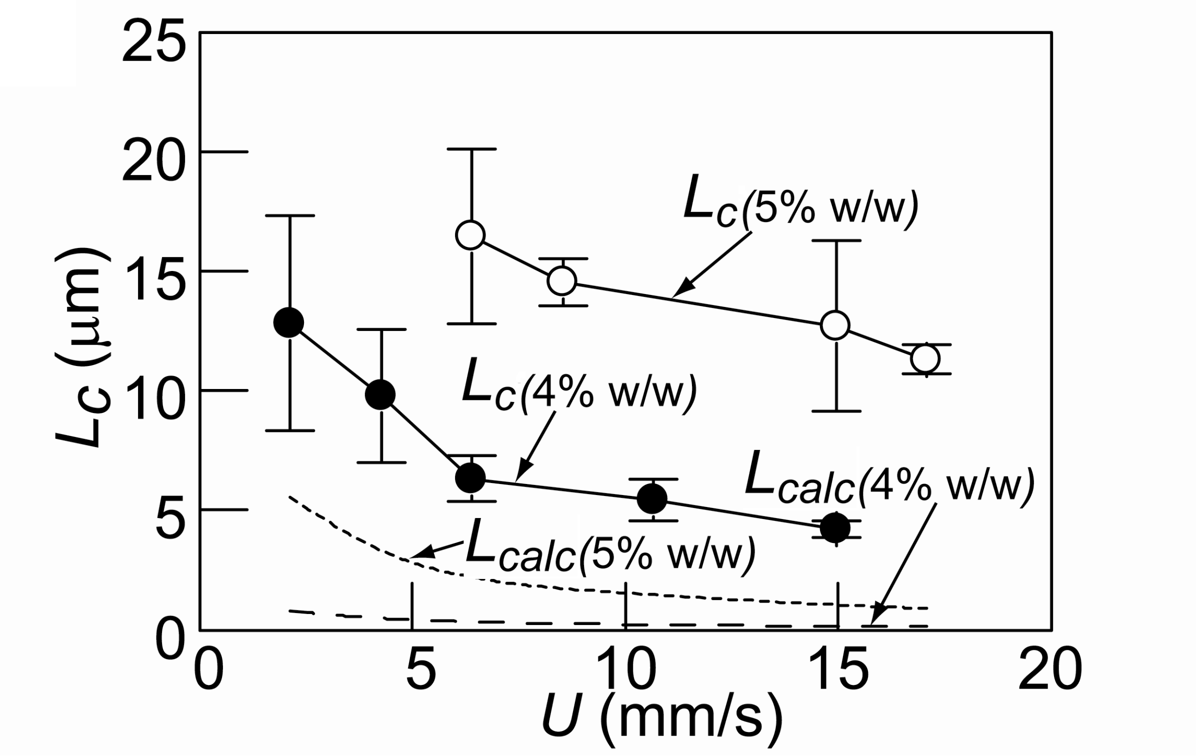

Figure 4.9: Characteristic width of reticulate filaments, L_c (C = 4% w/w and 5% w/w), obtained from FFT with varying total flow speeds, U. L_{calc} represents calculated critical size, R_{crit} defined in Khakhar and Ottino 1987 [37]

In the following, we will investigate the connection of our results from image processing with existing literature. From Grace 1971 [20] (Figure 4.10(right)) and Bentley and Leal 1986 [6], we know that 2D elongational flow is the most efficient among all types of linear flows for the deformation and breakup of drops. We estimate the elongation rate $\dot{\varepsilon}$ by U/H (despite overestimation), where the elongation rate is defined as $\dot{\varepsilon} = \Gamma : (\mathbf{m} \otimes \mathbf{m})^3$, U is the flow speed of the droplets and H is the channel depth ($100\mu m$).

---

[3] For 2D elongational flow, $\dot{\varepsilon} = G$ where G is defined in Appendix F. **m**: orientation vector.

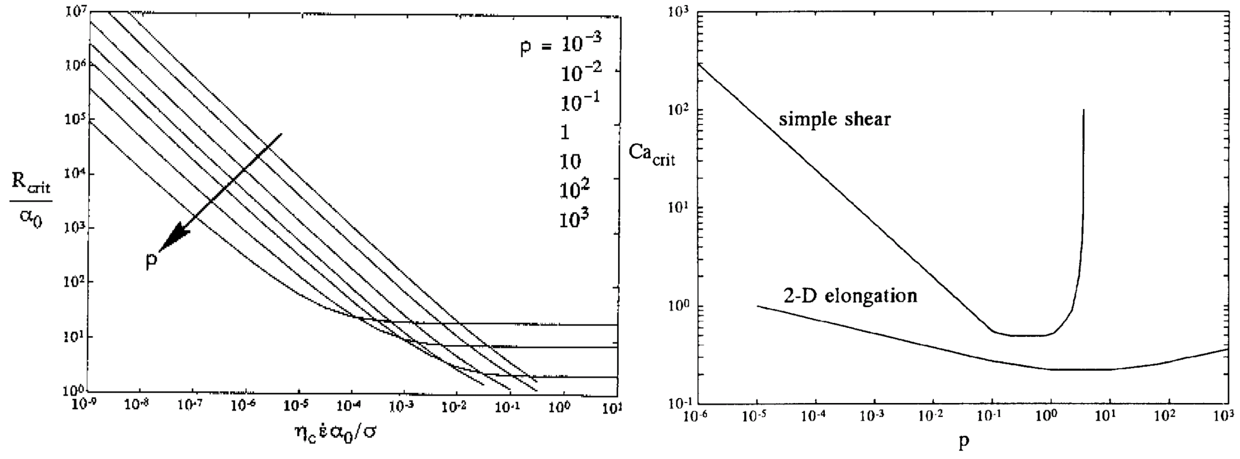

Figure 4.10: (left) Scaled critical thread radius versus scaled stretching rate $\dot{\varepsilon}$. Adopted from Janssen [31]. (right) Critical capillary number versus the viscosity ratio p in simple shear and 2D elongational flows. Adopted from Janssen and Meijer 1993 [32](Reproduced from Grace 1971 [20])

Then, we apply the theoretical analysis by Khakhar and Ottino [37] for the breakup of drops in general linear flows to find out the R_{crit}, representing the starting point for the growth of disturbance that finally leads to breakup (Figure 4.11). The theoretical results by Khakhar and Ottino are summarized to a figure by Janssen (Figure 4.10(left)), from which we obtain the two R_{crit} curves at different flow speeds (Figure 4.9 L_{calc}). Knowing that 2D elongational flow is the most efficient for drop breakup and that $\dot{\varepsilon} = U/H$ is an overestimation, R_{crit} should characterize the finest possible filament size in the droplets. From Figure 4.10, we do observe that $L_{calc} = R_{crit}$ is well below the characteristic sizes of the filaments obtained by FFT of the stereomicroscopic images of the droplets. From this point of view, the existing theory is consistent with our experimental observations.

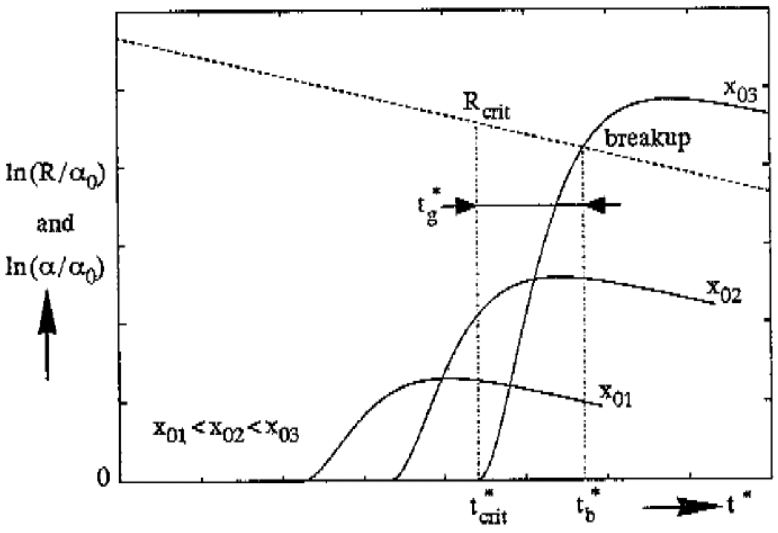

Figure 4.11: Evolution of the undisturbed radius R of a thread that is extending at a constant rate $\dot{\varepsilon}$ (dashed line) and evolution of disturbances with difference amplitude α and with different initial wave numbers (solid curve). Taken from Janssen's Ph.D thesis [31].

4.4 Effect of Chaotic Mixing

According to Ottino [46], chaos refers to a situation where a slightly perturbation in the initial condition leads to a completely different trajectory. In mathematical language, $|dx| = e^{\sigma t}|dX|$, with a positive σ called the Liapunov exponential. The necessary and sufficient condition for chaos is that the flow has homoclinic or heteroclinic points. If a system is two dimensional, it has only one degree of freedom, the stream function, $\psi(x, y)$. A steady two-dimensional flow is always an integrable Hamiltonian system and as a result, convective mixing is rather poor. However, if the stream function $\psi(z, r, t)$ is time-periodic, the system becomes a Hamiltonian system with one and a half degrees of freedom and it produces chaotic mixing in most cases. One example would be the alternating vortices in a circular domain [4].

If we investigate the streamline inside the microchannel (Figure 4.12), there are two hyperbolic points in the dispersed droplet represented by the white spots, indicating the presence of chaotic mixing due to the nonlinearity induced by the interface. However, the fluid particles in the middle part of the dispersed droplet are trapped by the circular streamlines. In order to find out what will happen to our system if we increase the degree of chaotic mixing, a meandering section is incorporated in the device, which introduces time-periodic twists of the dispersed droplet and thereby promoting the interchange of materials across streamlines.

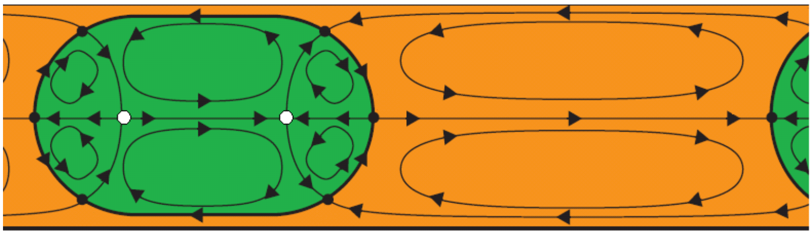

Figure 4.12: The circulation pattern of a droplet in a circular microchannel. Hyperbolic points in white. Adapted from Hodges et al [27]

As for our experiment, the DEX phase inside the droplet got much more dispersed after flowing through the meandering section (Figure 4.13). We can conclude that the meandering section can introduce more degree of chaotic mixing, enhancing the dispersion of the DEX-rich phase in the aqueous droplet.

In order to study the pattern of mixing inside a fluid domain, it is always difficult to distinguish the convective mixing from molecular diffusion if a dye is added into the fluid. With an aqueous two-phase system of ultra-low interfacial tension, molecular diffusion is prohibited due to its tendency to minimize the interfacial area. Hence, this ATPS of low interfacial tension can potentially be used to determine the existence of chaotic mixing as well as the efficiency of convective mixing.

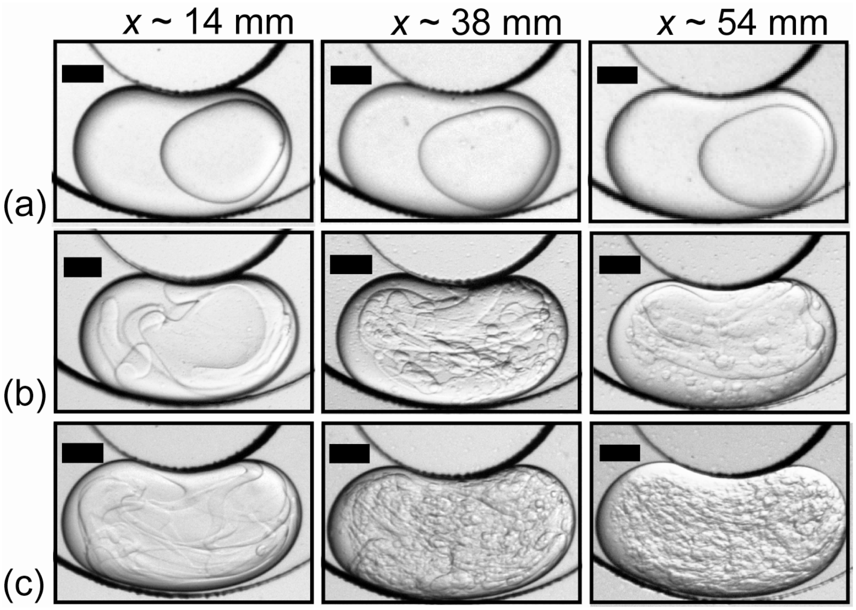

Figure 4.13: Stereomicroscopic images of ATPS droplet structures ($C = 5\%w/w$) obtained along the meandering portion of the microchannel with increasing flow speeds (a)0.64 mm/s (b)4.3 mm/s (c)7.5 mm/s. Scale bars represent 100 μm.

Chapter 5

Shear-Induced Homogenization

In this chapter, Nauman's studies on the thermodynamics of ternary systems will be briefly summarized and the possibility of shear-induced homogenization in the microfluidic ATPS will be discussed from both classical and thermodynamical points of view.

5.1 Nauman Theory for Ternary Systems

Different from the formulation of Cahn and Hilliard which is for an unconfined binary fluid domain, Nauman and Balsara [41] generalized it to a multi-component system of confined fluid domain. For illustrative purpose, a ternary system is taken for detailed analysis and derivation and the theory in this section can easily be generalized to multi-component systems. Essentially, it is a classical minimization problem with constrains. The functional that has to be minimized is the total free energy of the system expressed as

$$G_{total} = \int_V g(a, b, c, \nabla a, \nabla b, \nabla c) dV$$

$$= \int_V g_0(a,b,c) + \frac{K_1}{2}(\nabla a)^2 + K_{12}(\nabla a)(\nabla b) + \frac{K_2}{2}(\nabla b)^2 dV \tag{5.1}$$

with the following constrains

$$\bar{a} = \frac{1}{V}\int_V adV \quad \bar{b} = \frac{1}{V}\int_V bdV \quad \bar{c} = \frac{1}{V}\int_V cdV \tag{5.2}$$

The minimum condition must satisfy the Euler-Lagrange equations

$$\left(\frac{\delta G_{total}}{\delta a}\right)_{b,c} = \gamma_A \quad \left(\frac{\delta G_{total}}{\delta b}\right)_{a,c} = \gamma_B \quad \left(\frac{\delta G_{total}}{\delta c}\right)_{a,b} = \gamma_C \tag{5.3}$$

where γ_A, γ_B and γ_C are the Lagrange multipliers for the three constrains. It is important to note that a, b and c are all considered as independent variables first before imposing the relation $a + b + c = 1$ at the end of the theoretical analysis, which has no difference to if this relation is imposed at the very beginning. Nauman and Balsara introduced a new thermodynamic property, the variational free energy, Υ, defined by the following relationship:

$$\left(\frac{\partial \Upsilon}{\partial a}\right)_{b,c} = \left(\frac{\delta G_{total}}{\delta a}\right)_{b,c} \tag{5.4}$$

This variational free energy, Υ is equivalent to the average molar property of a mixture in the context of classical thermodynamics. According to Van Ness and Abbott [66], the partial molar property can be expressed as

$$\overline{M}_i = M + \left(\frac{\partial M}{\partial x_i}\right)_{T,P,x_{j\neq i}} - \sum_k x_k \left(\frac{\partial M}{\partial x_k}\right)_{T,P,x_{j\neq k}} \tag{5.5}$$

Hence, the generalized chemical potential for each species is defined as

$$\mu_A = \Upsilon + (b+c)\left(\frac{\partial \Upsilon}{\partial a}\right)_{b,c} - b\left(\frac{\partial \Upsilon}{\partial b}\right)_{a,c} - c\left(\frac{\partial \Upsilon}{\partial a}\right)_{b,c} \tag{5.6}$$

with μ_B and μ_C defined in similar manner. It is important to note that this variational free energy is a thermodynamically consistent variable because it satisfies both the Euler's relation

$$\Upsilon = a\mu_A + b\mu_B + c\mu_C \tag{5.7}$$

and the Gibbs-Duhem equation

$$a\nabla\mu_A + b\nabla\mu_B + c\nabla\mu_C = 0 \tag{5.8}$$

From the definition of the variational free energy (Eq 5.4), we have

$$\left(\frac{\partial\Upsilon}{\partial a}\right)_{b,c} = \gamma_A \quad \left(\frac{\partial\Upsilon}{\partial b}\right)_{a,c} = \gamma_B \quad \left(\frac{\partial\Upsilon}{\partial c}\right)_{a,b} = \gamma_C \tag{5.9}$$

By integration,

$$\Upsilon = a\gamma_A + b\gamma_B + c\gamma_C \tag{5.10}$$

By comparison with the Euler's relation (Eq 5.7), we find that Lagrange multipliers are actually the chemical potentials for each species, $\gamma_i = \mu_i$. According to the generalized Fick's law,

$$j_A = -Da\nabla\mu_A \tag{5.11}$$

The equation above can be written in another form (Appendix D)

$$j_A = -Da\left(b\nabla(\mu_A - \mu_B) + c\nabla(\mu_A - \mu_C)\right) \tag{5.12}$$

The same form of expressions applies to μ_B and μ_C. With the conservation equation for each species,

$$\frac{\partial c_i}{\partial t} = -\nabla \cdot j_i \tag{5.13}$$

we will be able to model the phase separation and the hydrodynamics of the ternary mixture.

With the theoretical analysis developped above, He et al [25] linearized the Euler-Lagrange equations by Taylor expansion to the first order around the critical condition. They found that the minimum size that can possibly exist inside a ternary polymer blend is to the order of the radius of gyration of the polymers, R_G (typical between $3R_G$ and $10R_G$).

5.2 Possibility of Shear-induced Homogenization

Dated back to the 1930s, Taylor had investigated the stability of a droplet under uniform shear stress in an unconfined domain [63]. The essential idea is that the interface will be destabilized once the shear stress becomes comparable to the Laplace pressure of the droplet. It was shown that in an unconfined shear field, droplets with $Ca = \eta\dot{\gamma}R/\sigma$ less than a critical value Ca_c remain stable, while those with Ca larger than Ca_c will be stretched and break up. Here, η is the viscosity of the bulk fluid, $\dot{\gamma}$ is the shear rate of the bulk fluid, R is the size of the droplet and σ is the interfacial tension between the bulk phase and the dispersed phase. Most of the previous studies mainly concentrated on an unconfined uniform shear field. T. Hashimoto reported in a series of papers ([23][60][61][19][24]) that polymer blends exhibited highly anisotropic string-like morphology near a thermodynamic phase-transition point. When the shear rate is greater than a critical value, a shear-induced homogenization is achieved (Figure 5.1). Later on, Migler [43] investigated the phase behavior of polymer blends between two rotating disks with a gap $d = 36 \pm 5\mu m$ comparable to the breakup size $R_B = Ca_c\sigma/\eta\dot{\gamma}$. A transition from a dispersed phase to a stable string phase upon decreasing shear rate was reported. In our experiments, blending of two polymers within a microfluidic droplet of the order of a few picolitres has been studied.

Classical Approach

Our system differs from the previous studies in literature as the fluid domain is confined and the shear stress is not uniform. As a result, it is only possible for analysis based on the order of magnitude. Next, we will analyze the velocity required for the characteristic size of the dextran-rich phase to reach the order of the radius

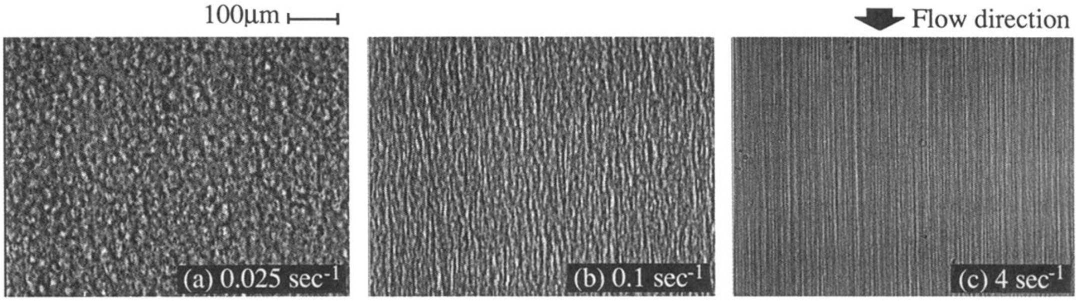

Figure 5.1: Transmission light micrographs for PS/PB (80:20)/DOP 3.3 w% at $\Delta T = 14^oC$. Taken from Hashimoto et al [24]. They claimed that further increase in flow rate would lead to homogenization.

of gyration ($< 100nm$), which is the necessary condition for homogenization [25]. The physical properties of the fluids at ambient temperature are:

	PEG 10 wt%	DEX 10 wt%	Water
Surface Tension with PFD/PO(mN/m)	8.2	17.6	5.4
Viscosity(mPa-s)	5.4	19.7	0.8

Table 5.1: Viscosity and Surface Tension with the oil

If the classical concept of interface of infinitesimal thickness is assumed to be valid, similar argument as Taylor applies

$$\eta\frac{U}{L} \sim \frac{\sigma}{R} \tag{5.14}$$

where U is the average velocity of the fluid, L is the characteristic size of the microchannel ($\sim 100\mu m$), σ is the interfacial tension ($\sim 1\mu N/m$ for compositions near the miscibility line [56]) and R is the characteristic size of the DEX-rich structure. Therefore,

$$10^{-3}\frac{U}{10^{-4}} \sim \frac{10^{-6}}{R} \tag{5.15}$$

In order to tear the DEX-rich phase to structures of the order of $100nm$, an average velocity of $10^6 \mu m/s \sim 10^4 L/s$ must be imposed and in practice, this is far out of the operating range[1]. From this classical point of view, it is not possible to achieve complete homogenization just by the shear caused by the flow in the microchannel of the current design.

Thermodynamic Exploration

For large systems where the energy of the interface is negligible as compared to the free energy of the entire system, phase separation is preferred to have a significant decrease in total free energy [42]. However, for small systems, the second term in the free energy $(\nabla c)^2$ scales as $(c/d)^2$ starts to dominate as d tends to zeros, where d represents the characteristic size of the system. Since this gradient term, $(\nabla c)^2$, is always positive, the system would prefer a zero-gradient state, i.e., a state of uniform composition, if the decrease in the first term of the free energy by phase separation can no longer compensate for the increase in the second term.

Nauman and He [41][42][25] have theoretically studied such a pitchfork-type bifurcation for both binary systems and ternary systems by imposing zero concentration gradient at the boundaries and resorting to Taylor expansion around the average composition, $\overline{c_i}$. They found that if the characteristic size of the fluid do-

---

[1] The possible velocity that can be achieved is within 50 times the width of the channel per second. This limitation of our design is due to the fact that at high flow rates, the two polymer streams at the inlet will coflow instead of forming emulsions. The operating range can be improved by an alternative design in which the two polymer stream form emulsion at low flow rate and an additional stream of oil is injected downstream to speed up the flow. However, the PDMS device will delaminate if the internal pressure exceeds a certain limit and this limitation is insurmountable

main is smaller than a critical value, L_c , the system will be homogeneous. For a binary system,

$$L_c = \pi \left(\frac{K}{-g''(\overline{a})} \right)^{1/2} \tag{5.16}$$

with K defined as in Eq 3.11. For a ternary system, the expression is given by Eq 14 in He et al [25]. However, direct substitution of the physical parameters for our ATPS into the expression by He et al gives an imaginary number. This might be due to the fact that the expression by He et al is obtained from Taylor expansion near critical conditions and as a result, it is only valid for compositions in extremely close vicinity of the binodal line. Moreover, the accuracy of the interaction parameters provided by H. Johansson [34] is questionable.

Although many current literatures have reported shear-induced homogenization by techniques of light scattering or confocal microscopes (Figure 5.1), their definition of such homogenization is that the dispersed fluid droplets cannot be detected by light. In our case, we do observe apparently homogeneous droplets at low resolutions of the microscope. At higher resolutions, very fine and elongated fluid domains with very poor contrast with the matrix fluid can still be observed. Moreover, homogenization might be induced by augmentation of temperature resulting from large viscous dissipation ($2\eta\Gamma : \Gamma$) at high shear rates. Hence, it's difficult to tell whether a complete homogenization up to the level of radii of gyration (R_G) can be induced by applying shear. Another possibility is to study this problem from the point of view of the energy of the system, which for sure will be part of research focus in the future.

Chapter 6

Future Work

In the framework of this thesis, the hydrodynamics and the thermodynamics of the aqueous two-phase microfluidic droplets have been studied in details both by experiments and by theoretical analysis. Microfluidic aqueous two-phase droplets were created in a continuous and uniform fashion by injecting two polymer solutions at a Y-shaped junction into the continuous phase. It was found that the microfluidic droplets exhibited a continuum of morphologies for different flow speeds and compositions and a morphology phase map was constructed in order to facilitate the control of the morphology of such compound droplets.

In order to understand the underlying physics, the author derived the Cahn-Hilliard theory from the Landau theory and the author applied similar analysis for a ternary system and arrived at the conclusion that the surface free energy is minimized when the Δg term is equal to the gradient term (3.86) even for ternary systems. Based on these theoretical analysis, the interfacial thickness (l) of the PEG-dextran aqueous two-phase system(ATPS) was approximately calculated to be a few microns near critical concentrations from the experimental measurement of interfacial tensions for different compositions in literature [56][26]. Fast Fourier Transform (FFT) was employed to find out the characteristic sizes of the elongated fluid filaments at different flow speeds and it was found the elongated fluid filaments resulting from great shear rate can reach the order of interfacial thickness.

The existing theoretical and experimental studies on the breakup of drops in flows were summarized, which helped with the understanding of the morphologies of our microfluidic ATPS. By drawing an analogy with the previous experimental studies, we will determine the critical capillary numbers for the transitions between different morphology regions on the morphology phase map that was constructed. It was also found that the sizes from FFT are well larger than the R_{crit} defined by Khakhar and Ottino [37], representing the critical filament radius at which the surface disturbance starts to grow and eventually leads to breakup. From this point of view, the existing theory is consistent with our experimental observations

Our current device has a small operating range of flow rate. It should be possible to enlarge it by better design of the process. For example, the formation of aqueous two-phase droplets takes place upstream at low flow rate and an additional stream of continuous phase is injected downstream to increase the flow rate and hence the shear. By doing so, coflow of the two polymer solution streams can be suppressed and we will be able to study the morphology of the droplet and the possibility of microfluidic-based homogenization at much higher flow rates that cannot be achieved by the current device. More creative microfluidic designs are desired to separate the satellite droplets from the large ones on-chip and collect the micro-sized aqueous two-phase droplets off-chip. Our system should also be analyzed by more sophisticated equipment like confocal microscope or fluorescence microscope to better understand the partitioning of the two polymers. If the characteristic sizes of the elongated filaments in both the longitudinal and the transverse directions can be quantitatively captured, we could compare the degree of deformation with the experiments done by Bentley and Leal [6] and we will be able to have a better understanding of the fluid mixing inside the droplets.

In addition, some of the theoretical analyses are still based on some approximative arguments and assumptions. A more comprehensive formulation for multicomponent polymer solutions with different length of molecular chains should be explored to better describe the current PEG-DEX-water ternary system. Moreover, it would be of great industrial interests if an automated on-chip extraction and purification process of biomedical products based on the current microfluidic aqueous two-phase system is successfully achieved. Furthermore, the exact causes for the formation of the "third" inner phase have to be studied in greater details.

With detailed studies on the hydrodynamics and thermodynamics of the microfluidic aqueous two-phase droplets, we will be able to better control the hydrodynamic and topological behaviors of the droplets. Hopefully, these will contribute to the development of more sophisticated on-chip molecular separation and reaction process by tuning the morphological state of the ATPS droplets.

Appendix A

Oseen Burgers Tensor

Dirac Distribution

Definition: Ω is an open set of $\mathbf{R}^N$. If we have a linear form defined as $< \delta_0, \phi >= \phi(0)$ for all compactly supported test functions $\phi \in C_c{}^{\infty}(\Omega)$, δ_0 is the Dirac distribution at the origin.

Properties: The Fourier transform of Dirac function is 1, i.e.

$$\boldsymbol{F}(\delta_0(\mathbf{r})) = 1 \tag{A.1}$$

Hence, the inverse Fourier transform of 1 is a Dirac function, i.e.

$$\delta_0(\mathbf{r}) = \boldsymbol{F}^{-1}(1) = \frac{1}{(2\pi)^3} \int_{R^3} e^{i\mathbf{kr}} d\mathbf{k} \tag{A.2}$$

Theorem: $-\nabla^4(\frac{r}{8\pi})$ and $-\nabla^2(\frac{1}{4\pi r})$ are all Dirac distributions at the origin. In other words, the fundamental solutions in three dimensions for Laplace equation and biharmonic equation are respectively $-\frac{1}{4\pi r}$ and $-\frac{r}{8\pi}$ [29].

Derivation from Fourier Space to Real Space

In Fourier space, the Oseen-Burgers tensor (Eq 4.36) is expressed as [72]

$$\widehat{T}(\mathbf{k}) = \frac{1}{\eta k^2}(I - \frac{\mathbf{k}\otimes\mathbf{k}}{k^2}) \tag{A.3}$$

In real space, it should be

$$T(\mathbf{r}) = \boldsymbol{F}^{-1}(\widehat{T}(\mathbf{k})) = \frac{1}{(2\pi)^3}\int_{R^3}\frac{1}{\eta k^2}(1 - \frac{\mathbf{k}\otimes\mathbf{k}}{k^2})e^{i\mathbf{kr}}d\mathbf{k} \tag{A.4}$$

From the precedent paragraph A.1, we have

$$\nabla^2(-\frac{1}{4\pi r}) = \delta_0(\mathbf{r}) = \frac{1}{(2\pi)^3}\int_{R^3} e^{i\mathbf{kr}}d\mathbf{k} \tag{A.5}$$

Hence,

$$\nabla(\frac{1}{4\pi r}) = \frac{1}{(2\pi)^3}\int_{R^3}\frac{i\mathbf{k}}{k^2}e^{i\mathbf{kr}}d\mathbf{k} \tag{A.6}$$

$$\frac{1}{4\pi r} = \frac{1}{(2\pi)^3}\int_{R^3}\frac{1}{k^2}e^{i\mathbf{kr}}d\mathbf{k} \tag{A.7}$$

In addition,$-\nabla^4(r/8\pi)$ is also a Dirac function, i.e.

$$\nabla^4(\frac{r}{8\pi}) = -\delta_0(\mathbf{r}) = -\frac{1}{(2\pi)^3}\int_{R^3} e^{i\mathbf{kr}}d\mathbf{k} \tag{A.8}$$

Hence,

$$\frac{r}{8\pi} = -\frac{1}{(2\pi)^3}\int_{R^3}\frac{1}{k^4}e^{i\mathbf{kr}}d\mathbf{k} \tag{A.9}$$

$$\nabla\nabla(\frac{r}{8\pi}) = \frac{1}{(2\pi)^3}\int_{R^3}\frac{\mathbf{k}\otimes\mathbf{k}}{k^4}e^{i\mathbf{kr}}d\mathbf{k} \tag{A.10}$$

By Equation A.4, A.7 and A.10, we can easily identify that

$$\begin{aligned} T(\mathbf{r}) &= \frac{1}{4\pi\eta r}I - \frac{1}{\eta}\nabla\nabla(\frac{r}{8\pi}) = \frac{1}{4\pi\eta r}I - \frac{1}{\eta}(-\frac{1}{8\pi}\frac{\mathbf{r}\otimes\mathbf{r}}{r^3} + \frac{I}{8\pi r}) \\ &= \frac{1}{8\pi\eta r}(I + \frac{\mathbf{r}\otimes\mathbf{r}}{r^2}) \end{aligned} \tag{A.11}$$

Appendix B

Rayleigh Instability

B.1 Inviscid Fluid Jet

B.1.1 Navier-Stokes Point of View

The assumptions made in this section are that the fluid is incompressible[1] and perfect[2]. The flow is laminar and hence the quadratic terms ($\sim U^2$) are neglected. In addition, the liquid thread is axisymmetric. With the assumptions above, the Navier-Stokes equation simplifies to

$$\begin{aligned} \rho\frac{\partial v_r}{\partial t} &= -\frac{\partial p}{\partial r} \\ \rho\frac{\partial v_z}{\partial t} &= -\frac{\partial p}{\partial z} \end{aligned} \tag{B.1}$$

and the continuity equation becomes

$$\frac{1}{r}\frac{\partial(rv_r)}{\partial r} + \frac{\partial v_z}{\partial z} = 0 \tag{B.2}$$

A perturbation is then introduced by Fourier transform with respect to z and pseudo-Laplace transform with respect to t for all variables [16], i.e.,

$$r = a + \epsilon e^{\omega t + i\kappa z}$$

---

[1] This is equivalent to $D\rho/Dt = 0$ or $\nabla \cdot \mathbf{v} = 0$.

[2] Inviscid and there is no heat flux, i.e., $\eta = 0$ and $\mathbf{q} = -k\nabla T = 0$

$$v_r = R(r)e^{\omega t+i\kappa z} \tag{B.3}$$
$$v_z = Z(r)e^{\omega t+i\kappa z}$$
$$p = p_0 + P(r)e^{\omega t+i\kappa z}$$

The Navier-Stokes equations and the continuity equation become

$$\begin{aligned}
\rho\frac{\partial Re^{\omega t+i\kappa z}}{\partial t} &= -\frac{\partial}{\partial r}\left(Pe^{\omega t+i\kappa z}+p_0\right)\\
\rho\frac{\partial Ze^{\omega t+i\kappa z}}{\partial t} &= -\frac{\partial}{\partial r}\left(Pe^{\omega t+i\kappa z}+p_0\right)\\
\frac{\partial Re^{\omega t+i\kappa z}}{\partial r}+\frac{R}{r}e^{\omega t+i\kappa z}+\frac{\partial}{\partial z}&\left(Ze^{\omega t+i\kappa z}\right)=0
\end{aligned} \tag{B.4}$$

After simplification,

$$\begin{aligned}
\rho\omega R &= -\frac{\partial P}{\partial r}\\
\rho\omega Z &= -\frac{i\kappa P}{\rho}\\
\frac{\partial R}{\partial r}+\frac{R}{r}+i\kappa Z &= 0
\end{aligned} \tag{B.5}$$

The three equations above (Eq B.5) can be combined by eliminating P and Z and we arrive at

$$r^2\frac{d^2R}{dr^2}+r\frac{dR}{dr}-\left(1+(\kappa r)^2\right)R=0 \tag{B.6}$$

This is the modified Bessel equation and its solution is in the form of

$$R(r) = C_1\widetilde{I}_1(\kappa r)+C_2\widetilde{K}_1(\kappa r) \tag{B.7}$$

where $\widetilde{I}_1$ and $\widetilde{K}_1$ are the modified Bessel function of the first and the second kind respectively[3]. The boundary conditions are

$$R(r=0)=0 \tag{B.8}$$

---

[3] The general solution can also be written in the form of the Bessel function as we will see in the next two sections.

$$At\ r \cong a : \frac{\partial r}{\partial t} = \mathbf{v} \cdot \mathbf{n} \cong v_r \tag{B.9}$$

$$At\ \partial\Omega : p = \sigma C = \sigma \nabla \cdot \mathbf{n} \tag{B.10}$$

From the first boundary condition (Eq B.8), the second term in the general solution (Eq B.7) has to vanish because the modified Bessel function of the second kind diverges at the origin (Figure B.1), i.e., $C_2 = 0$ and the solution becomes

$$R(r) = C_1 \widetilde{I}_1(\kappa r) \tag{B.11}$$

From the Eqs B.5, we have

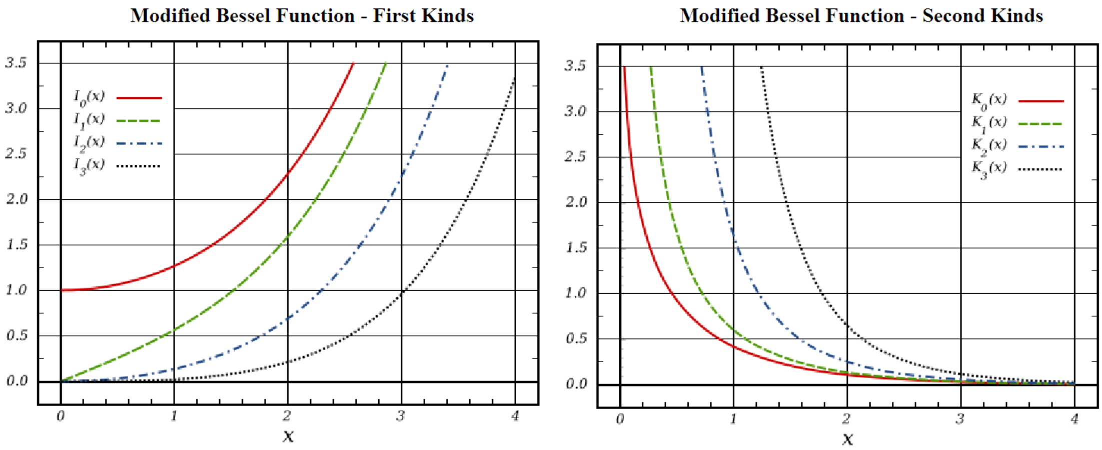

Figure B.1: The modified Bessel function (left) of the first kinds $\widetilde{I}_i$ and (right) of the second kinds $\widetilde{K}_i$.(Source: Wikipedia)

$$P(r) = -\frac{\omega \rho C_1 \widetilde{I}_0(\kappa r)}{\kappa} \tag{B.12}$$

$$Z(r) = i C_1 \widetilde{I}_0(\kappa r)$$

where $\widetilde{I}_1(x) = \widetilde{I}_0'(x)$. From the second boundary condition (Eq B.9), we have

$$\frac{\partial}{\partial t}\left(a + \epsilon e^{\omega t + i\kappa z}\right) = C_1 \widetilde{I}_1(\kappa a) e^{\omega t + i\kappa z} \tag{B.13}$$

It simplifies to

$$C_1 = \frac{\epsilon\omega}{\widetilde{I}_1(\kappa a)} \tag{B.14}$$

By Eq B.12, the pressure is expressed as

$$p = p_0 + \frac{\epsilon\omega^2\rho}{\kappa}\frac{\widetilde{I}_0(\kappa r)}{\widetilde{I}_1(\kappa a)}e^{\omega t + i\kappa z} \tag{B.15}$$

where $p_0 = \sigma/a$.From the third boundary condition (Eq B.10) and with the approximated expression of curvature (Eq 4.2), we have

$$\begin{aligned} p = \sigma C = \sigma\left(-\frac{d^2r}{dz^2} + \frac{1}{r}\right) &= \sigma\left(-\frac{d^2\left(a + \epsilon e^{\omega t + i\kappa z}\right)}{dz^2} + \frac{1}{a + \epsilon e^{\omega t + i\kappa z}}\right) \\ &\cong \sigma\left(\epsilon\kappa^2 e^{\omega t + i\kappa z} + \frac{1}{a} - \frac{\epsilon}{a^2}e^{\omega t + i\kappa z}\right) \end{aligned} \tag{B.16}$$

By comparing the two expressions for pressure (Eq B.15 and Eq B.16), we obtain the dispersion relation

$$\omega^2 = \frac{\sigma}{\rho a^3}\frac{\kappa a\widetilde{I}_1(\kappa a)}{\widetilde{I}_0(\kappa a)}\left(1 - (\kappa a)^2\right) \tag{B.17}$$

The maximum ω_{max} is found when $\lambda = 2\pi/\kappa = 4.51 \times 2a = 4.51D$.

B.1.2 Energetic Point of View

The assumptions made in this section are that the fluid is irrotational[4], incompressible and perfect. In addition, the liquid thread is axisymmetric. This section is the original work by Rayleigh in 1878 [53]. Suppose that the surface of the liquid jet at time t is

$$r = a + \alpha cos(\kappa z) \tag{B.18}$$

The surface area per unit length is

$$A = \frac{1}{\lambda}\int_0^\lambda 2\pi r\sqrt{1 + \left(\frac{dr}{dz}\right)^2}dz = \frac{1}{\lambda}\int_0^\lambda 2\pi(a + \alpha cos\kappa z)\sqrt{1 + (\kappa\alpha sin\kappa z)^2}dz \tag{B.19}$$

---

[4] The curl of the velocity is zero, i.e., $\nabla \times \mathbf{v} = \mathbf{0}$.

Since $\alpha \ll 1$ and by Taylor's expansion $\sqrt{1+x} \cong 1 + x/2$ for $x \ll 1$,

$$A = \frac{1}{\lambda}\int_0^\lambda 2\pi(a + \alpha cos\kappa z)\left(1 + \frac{1}{2}\kappa^2\alpha^2 sin^2\kappa z\right)dz = 2\pi a + \frac{1}{2}\pi a\kappa^2\alpha^2 \tag{B.20}$$

The volume per unit length is

$$S = \frac{V}{\lambda} = \frac{1}{\lambda}\int_0^\lambda \pi r^2 dz = \frac{1}{\lambda}\int_0^\lambda \pi(a + \alpha cos\kappa z)^2 dz = \pi a^2 + \frac{1}{2}\pi\alpha^2 \tag{B.21}$$

From the equation B.21 above, we have $a^2 = \frac{S}{\pi} - 1/2\alpha^2$. Using the same Taylor's expansion,

$$a = \sqrt{\frac{S}{\pi} - \frac{1}{2}\alpha^2} = \sqrt{\frac{S}{\pi}}\sqrt{1 - \frac{1}{2}\frac{\pi\alpha^2}{S}} = \sqrt{\frac{S}{\pi}}\left(1 - \frac{1}{4}\frac{\pi\alpha^2}{S}\right) = \sqrt{\frac{S}{\pi}} - \frac{1}{4}\sqrt{\frac{\pi}{S}}\alpha^2 \tag{B.22}$$

Hence, from Eq B.20 and Eq B.22, we have

$$A = 2\pi\left(\sqrt{\frac{S}{\pi}} - \frac{1}{4}\sqrt{\frac{\pi}{S}}\alpha^2\right) + \frac{1}{2}\pi a\kappa^2\alpha^2 \tag{B.23}$$

From Eq B.22and as α is small, we have

$$\sqrt{\frac{\pi}{S}} = \frac{1}{a + \frac{1}{4}\sqrt{\frac{\pi}{S}}\alpha^2} \cong \frac{1}{a} + O(\alpha^2) \tag{B.24}$$

From Eq B.23, we have

$$A = 2\sqrt{\pi S} - \frac{2\pi}{4}\left(\frac{1}{a} + O(\alpha^2)\right)\alpha^2 + \frac{1}{2}\pi a\kappa^2\alpha^2 = 2\sqrt{\pi S} + \frac{\pi\alpha^2}{2a}(a^2\kappa^2 - 1) + O(\alpha^2) \tag{B.25}$$

For a perfect cylinder without perturbation, $S = \pi r^2$ and $A_0 = 2\pi r$. Hence, we have

$$A_0 = 2\sqrt{\pi S} \tag{B.26}$$

By Eq B.25 and Eq B.26,the potential energy due to perturbation of the surface is

$$V = \sigma(A - A_0) = -\sigma\frac{\pi\alpha^2}{2a}\left(1 - \kappa^2a^2\right) \tag{B.27}$$

Since the fluid jet is assumed to be irrotational, there must be a velocity potential ϕ such that

$$\mathbf{v} = \nabla\phi \tag{B.28}$$

In explicit form,

$$v_r = \frac{\partial\phi}{\partial r} \qquad v_z = \frac{\partial\phi}{\partial z} \tag{B.29}$$

We also assumed that the fluid is incompressible,

$$\nabla \cdot \mathbf{v} = \triangle\phi = 0 \tag{B.30}$$

Due its axisymmetry, the laplacian $\triangle\phi$ becomes

$$\frac{\partial^2\phi}{\partial r^2} + \frac{1}{r}\frac{\partial\phi}{\partial r} + \frac{\partial^2\phi}{\partial z^2} = 0 \tag{B.31}$$

If an undulation is introduced in the z direction, $\phi = \varphi cos\kappa z$. The laplace equation above becomes

$$\frac{\partial^2\varphi}{\partial r^2} + \frac{1}{r}\frac{\partial\varphi}{\partial r} - \kappa^2\varphi = 0 \tag{B.32}$$

It has a general solution

$$\varphi = C_1 I_0(i\kappa r) + C_2 K_0(i\kappa r) \tag{B.33}$$

where I_0 and K_0 are the Bessel functions of the first and second kind respectively. Since there is no singularity at $r = 0$, the second term has to vanish (Figure B.1). The velocity potential is

$$\phi = C_1 I_0(i\kappa r) cos\kappa z \tag{B.34}$$

Another boundary condition for the outwards normal velocity at the surface gives

$$\frac{dr}{dt} = \dot{\alpha} cos\kappa z = v_r = \frac{\partial\phi}{\partial r} = i\kappa A I_0'(i\kappa a) \tag{B.35}$$

The differential kinetic energy is

$$d(KE) = \frac{1}{2}\rho\ dV v^2 = \frac{1}{2}\rho v^2 (2\pi r dr) \tag{B.36}$$

The kinetic energy per unit length is

$$KE = \frac{1}{\lambda}\left(\frac{1}{2}\rho\int_0^\lambda\int_0^a 2\pi r v^2 drdz\right) = \frac{1}{2\lambda}\rho\int_0^\lambda\int_0^a 2\pi r\left(\left(\frac{\partial\phi}{\partial r}\right)^2 + \left(\frac{\partial\phi}{\partial z}\right)^2\right)drdz \tag{B.37}$$

By integration by part and we have

$$KE = \frac{1}{2\lambda}\rho\int_0^\lambda 2\pi\left(\phi r\frac{\partial\phi}{\partial r}\right)_0^a dz - \frac{1}{2\lambda}\rho\int_0^\lambda\int_0^a 2\pi\phi r\left(\frac{\partial^2\phi}{\partial r^2} + \frac{1}{r}\frac{\partial\phi}{\partial r} - \kappa^2\phi\right)drdz \tag{B.38}$$

The last term vanishes because of Eq B.32 and we arrive at

$$KE = \frac{1}{2\lambda}\rho\int_0^\lambda 2\pi a\phi(a)\left(\frac{\partial\phi}{\partial r}\right)_a dz = \frac{1}{2\lambda}\rho\int_0^\lambda 2\pi a(AI_0(i\kappa a)cos\kappa z)(i\kappa AI_0'(i\kappa a)cos\kappa z)dz \tag{B.39}$$

From Eq B.35, $A^2 = \dot{\alpha}^2/(i\kappa)^2(I_0'(i\kappa a))^2$

$$KE = \frac{1}{2}\rho\pi a^2\frac{I_0(i\kappa a)\dot{\alpha}^2}{i\kappa a I_0'(i\kappa a)}$$

In order to study the temporal evolution of the system, we set $\alpha = \alpha' e^{\omega t}$ and substitute it into the expression for kinetic energy above

$$KE = \frac{1}{2}\rho\pi a^2\frac{I_0(i\kappa a)\omega^2\alpha^2}{i\kappa a I_0'(i\kappa a)} \tag{B.40}$$

By energy balance, the kinetic energy has to be equal to the potential energy

$$KE = V \tag{B.41}$$

from which we obtain the dispersion relation

$$\omega^2(\kappa) = \frac{\sigma}{\rho a^3}\frac{(1-\kappa^2a^2)i\kappa a I_0'(i\kappa a)}{I_0(i\kappa a)} = -\frac{\sigma}{\rho a^3}\frac{(1-\kappa^2a^2)i\kappa a I_1(i\kappa a)}{I_0(i\kappa a)} \tag{B.42}$$

as $I_0'(x) = -I_1(x)$. This is the same expression as the result (Eq B.17) from Navier-Stokes point of view (Section B.1.1). They are interchangeable by the relation between the Bessel functions and the modified Bessel functions: $\widetilde{I}_n(x) = i^{-n}I_n(ix)$.

B.1.3 Bernoulli Point of View

This section summarizes the work by Rayleigh in 1892 [54]. The assumptions made in this section are that the fluid is irrotational, barotropic[5], incompressible and perfect. Since the flow is laminar and the velocity is small, the quadratic terms ($\sim U^2$) are neglected. In addition, the liquid thread is axisymmetric. The Bernoulli's equation for irrotational, barotropic, incompressible and perfect fluid is [51]

$$\frac{\partial \phi}{\partial t} + \frac{U^2}{2} + \frac{p}{\rho} = c(t) \tag{B.43}$$

where ϕ is the velocity potential (Eq B.28) and it follows Eq B.31, p is the hydrodynamic pressure and $c(t)$ is a function of time. If we define a parameter μ_t by

$$\mu_t = -\frac{\rho c(t)}{\phi} \tag{B.44}$$

By introducing a perturbation in the solution of B.31, we have

$$\phi = A e^{int+ikz} I_0(i\kappa r) \tag{B.45}$$

From the Bernoulli's equation (B.43) and by neglecting the quadratic velocity term,

$$p = -(\mu_t + in\rho)\phi \tag{B.46}$$

Next, we are going to find another expression for p. The displacement ξ at the surface is expressed as

$$\xi = \int v_r dt = \int \frac{\partial \phi}{\partial r} dt = \frac{1}{in} \frac{\partial \phi}{\partial r} \tag{B.47}$$

By Eq 4.2, the mean curvature of the interface C follows

$$2C \cong -\frac{d^2 \xi}{dz^2} + \frac{1}{a+\xi} \cong \kappa^2 \xi + \frac{1}{a} - \frac{\xi}{a^2} \tag{B.48}$$

---

[5] The pressure is a function of density only, i.e., $p = f(\rho)$.

where a is the initial radius of the fluid jet. After subtracting the initial Laplace pressure σ/a, the hydrodynamic pressure should be

$$p = 2C\sigma \cong \kappa^2\sigma\xi - \frac{\sigma\xi}{a^2} = \frac{\sigma\xi(\kappa^2a^2-1)}{a^2} \tag{B.49}$$

By equating the two expressions for the hydrodynamic pressure (Eq B.46 and Eq B.49) and using Eq B.47,

$$\frac{\sigma(\kappa^2a^2-1)}{ina^2}\frac{\partial\phi}{\partial r} = -(\mu_t + in\rho)\phi \tag{B.50}$$

By Eq B.45, the dispersion relation is

$$\frac{\sigma}{\rho a^3}\frac{(\kappa^2a^2-1)i\kappa a I_0'(i\kappa a)}{I_0(i\kappa a)} + in(in + \frac{\mu_t}{\rho}) = 0 \tag{B.51}$$

This dispersion relation is equivalent to that of Section B.1.2 (Eq B.42) if $\mu_t = 0$.

B.2 Viscous Fluid Jet

B.2.1 Stream Function Point of View

This section summarizes the treatment by Rayleigh in 1892 [54]. We assume the fluid is incompressible and the system of interests is axisymmetric. If we neglect the quadratic terms ($\sim U^2$), the Navier-Stokes can be written as

$$\frac{\partial v_r}{\partial t} = -\frac{1}{\rho}\frac{\partial p}{\partial r} + \nu\left(\frac{\partial^2 v_r}{\partial r^2} + \frac{1}{r}\frac{\partial v_r}{\partial r} - \frac{v_r}{r^2} + \frac{\partial^2 v_r}{\partial z^2}\right) \tag{B.52}$$

in the $\mathbf{e}_r$ direction and

$$\frac{\partial v_z}{\partial t} = -\frac{1}{\rho}\frac{\partial p}{\partial z} + \nu\left(\frac{\partial^2 v_z}{\partial r^2} + \frac{1}{r}\frac{\partial v_z}{\partial r} + \frac{\partial^2 v_z}{\partial z^2}\right) \tag{B.53}$$

in the $\mathbf{e}_z$ direction.The continuity equation is

$$\frac{\partial v_r}{\partial r} + \frac{v_r}{r} + \frac{\partial v_z}{\partial z} = 0 \tag{B.54}$$

1 The normal stress at the surface equals to the Laplace pressure: $\sigma_{rr}(r = a) = 2C(r = a)\sigma$
2 There is no singularity at $r = 0$
3 The tangential stress at the surface is zero: $\sigma_{zr}(r = a) = 0$

The boundary conditions: Due to its axisymmetric feature, a 3D problem now becomes a 2D problem which can be described by a single parameter - the stream function ψ, which automatically satisfies the continuity equation

$$v_r = \frac{1}{r}\frac{\partial \psi}{\partial z} \qquad v_z = -\frac{1}{r}\frac{\partial \psi}{\partial r} \tag{B.55}$$

Combine the two Navier-Stokes equations by ∂_z(Eq B.52) $-$ ∂_r(Eq B.53), and we arrive at

$$\left(D - \frac{1}{\nu}\frac{\partial}{\partial t}\right) D\psi = 0 \tag{B.56}$$

where

$$D = \frac{\partial^2}{\partial r^2} - \frac{1}{r}\frac{\partial}{\partial r} + \frac{\partial^2}{\partial z^2} \tag{B.57}$$

Since the operator $D - \frac{1}{\nu}\frac{\partial}{\partial r}$ and D are commutative, ψ can be decomposed to two parts

$$\psi = \psi_1 + \psi_2 \tag{B.58}$$

where ψ_1 and ψ_2 satisfy

$$\left(D - \frac{1}{\nu}\frac{\partial}{\partial t}\right) \psi_1 = 0 \qquad D\psi_2 = 0 \tag{B.59}$$

By the similar technique as the previous sections, we impose

$$\psi_1 = \phi_1(r)e^{i(\omega t + \kappa z)}, \quad \psi_2 = \phi_2(r)e^{i(\omega t + \kappa z)} \tag{B.60}$$

Eq B.59 becomes

$$\frac{d^2\phi_1}{dr^2} - \frac{1}{r}\frac{d\phi_1}{dr} - \kappa^2\phi_1 = 0 \qquad \frac{d^2\phi_2}{dr^2} - \frac{1}{r}\frac{d\phi_2}{dr} - \kappa_1^2\phi_2 = 0 \tag{B.61}$$

where $\kappa_1^2 = \kappa^2 + i\omega/\nu$. The general solutions of Eq B.61 are

$$\phi_1 = ArI_0'(i\kappa r) \qquad \phi_2 = BrI_0'(i\kappa r) \tag{B.62}$$

because the fluid jet does not have singularity at $r = 0$ (Boundary Condition 2) and the solution should not have the Bessel function of the second kinds (Figure B.1). Boundary Condition 3 requires that at $r = a$:

$$\sigma_{zr}(a) = 0 \tag{B.63}$$

where σ_{ij} is the ij-th entry of the Cauchy's stress tensor for incompressible Newtonian fluids $\sigma_{ij} = -p\delta_{ij} + 2\mu\Gamma_{ij}$ and

$$\Gamma = \frac{1}{2}\left(\nabla\mathbf{v} + \nabla^T\mathbf{v}\right) = \frac{1}{2}\begin{pmatrix} 2\frac{\partial v_r}{\partial r} & \frac{1}{r}\left(\frac{\partial v_r}{\partial \theta}\right) + \frac{v_\theta}{r} & \frac{\partial v_z}{\partial r} + \frac{\partial v_r}{\partial z} \\ \frac{1}{r}\left(\frac{\partial v_r}{\partial \theta}\right) + \frac{v_\theta}{r} & \frac{2}{r}\left(\frac{\partial v_\theta}{\partial \theta} + v_r\right) & \frac{1}{r}\frac{\partial v_z}{\partial \theta} + \frac{\partial v_\theta}{\partial z} \\ \frac{\partial v_z}{\partial r} + \frac{\partial v_r}{\partial z} & \frac{1}{r}\frac{\partial v_z}{\partial \theta} + \frac{\partial v_\theta}{\partial z} & 2\frac{\partial v_z}{\partial z} \end{pmatrix} \tag{B.64}$$

Hence,

$$\frac{\sigma_{zr}(a)}{\mu} = \frac{\partial v_z}{\partial r} + \frac{\partial v_r}{\partial z} = 0 \tag{B.65}$$

From Eq B.62 and Eq B.55,

$$2\kappa^2 AI_0'(i\kappa a) + (\kappa_1^2 + \kappa^2)BI_0'(i\kappa_1 a) = 0 \tag{B.66}$$

Since p can also be decomposed to $P(r)e^{i(\omega t + \kappa z)}$, the Navier-Stokes equation in the $\mathbf{e}_z$ direction (Eq B.53) becomes

$$i\omega v_z = -\frac{i\kappa}{\rho}p + \nu\left(\frac{\partial^2 v_z}{\partial r^2} + \frac{1}{r}\frac{\partial v_z}{\partial r} - \kappa^2 v_z\right) \tag{B.67}$$

from which

$$p = -\frac{\rho\omega}{\kappa}v_z + \frac{\nu\rho}{i\kappa}\left(\frac{\partial^2 v_z}{\partial r^2} + \frac{1}{r}\frac{\partial v_z}{\partial r} - \kappa^2 v_z\right) \tag{B.68}$$

By apply Eq B.55,

$$p = \mu \left(\frac{\omega}{\kappa \nu r} \frac{d\psi_2}{dr} + 2i\kappa \frac{d}{dr} \left(\frac{\psi}{r} \right) \right) \tag{B.69}$$

With the expression for Laplace pressure Eq B.49, Boundary condition 1 requires that at $r = a$

$$\sigma_{rr}(a) = -p + 2\mu \frac{dv_r}{dr} = \frac{\sigma \xi (\kappa^2 a^2 - 1)}{a^2} \tag{B.70}$$

By Eq B.69, Eq B.55 and the expression for the stream function Eq B.62, we have

$$0 = \left(\frac{\sigma(1 - \kappa^2 a^2)}{\rho a^3} \frac{\kappa a}{\omega} I_0'(i\kappa a) + 2\nu\kappa^2 I_0''(i\kappa a) - i\omega I_0(i\kappa a) \right) A +$$
$$\left(\frac{\sigma(1 - \kappa^2 a^2)}{\rho a^3} \frac{\kappa a}{\omega} I_0'(i\kappa_1 a) + \nu \left(\frac{\kappa_1(\kappa_1^2 - \kappa^2)}{\kappa} I_0(i\kappa_1 a) + 2\kappa\kappa_1 I_0''(i\kappa_1 a) \right) - \frac{i\kappa_1 \omega}{\kappa} I_0(i\kappa_1 a) \right) B \tag{B.71}$$

for which we used the relation

$$I_0''(x) + \frac{I_0'(x)}{x} + I_0(x) = 0 \qquad I_0'(x) = -I_1(x) \tag{B.72}$$

To simultaneously satisfy the Boundary Condition 1 (Eq B.66) and the Boundary Condition 3 (Eq B.71), we must have the dispersion relation

$$det \begin{pmatrix} Q(\omega, \kappa a) & Z(\omega, \kappa a) \\ 2\kappa^2 I_0'(i\kappa a) & (\kappa_1^2 + \kappa^2) I_0'(i\kappa_1 a) \end{pmatrix} = 0 \tag{B.73}$$

where we define

$$Q(\omega, \kappa a) = \frac{\sigma(1 - \kappa^2 a^2)}{\rho a^3} \frac{\kappa a}{\omega} I_0'(i\kappa a) + 2\nu\kappa^2 I_0''(i\kappa a) - i\omega I_0(i\kappa a) \tag{B.74}$$

$$Z(\omega, \kappa a) = \frac{\sigma(1 - \kappa^2 a^2)}{\rho a^3} \frac{\kappa a}{\omega} I_0'(i\kappa_1 a) + \nu \left(\frac{\kappa_1(\kappa_1^2 - \kappa^2)}{\kappa} I_0(i\kappa_1 a) + 2\kappa\kappa_1 I_0''(i\kappa_1 a) \right) - \frac{i\kappa_1 \omega}{\kappa} I_0(i\kappa_1 a) \tag{B.75}$$

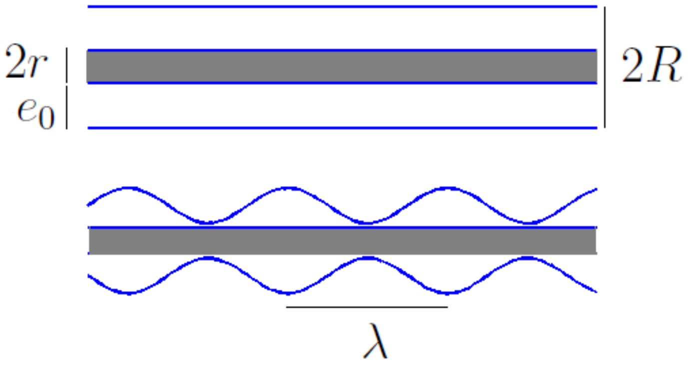

Figure B.2: (a) Schematic illustration for a layer of liquid of thickness e_0 stuck onto a thread of radius r. (b) Schematic illustration of undulation of wavelength λ on the surface

B.2.2 Poiseuille Point of View

We consider a cylindrical jet of liquid of radius R. This cylinder can be a free jet or a liquid film deposited onto a thread as shown in B.2. We denote r as the radius of the thread, $R = e_0 + r$ as the total radius of the cylinder, e_0 as the thickness of the liquid. First, we consider an axisymmetric undulation written in the form

$$e = e^* + \varepsilon cos(kx) \tag{B.76}$$

Since the volume of the liquid has to be conserved, we have

$$\lambda\pi\left((r+e_0)^2 - r^2\right) = \int_0^\lambda \pi\left((r + e^* + \varepsilon cos(kx))^2 - r^2\right) dx \tag{B.77}$$

Then, we will get an expression for e^*:

$$e^* = e_0 - \frac{\varepsilon^2}{4(r+e_0)} \tag{B.78}$$

If $R < \kappa^{-1} = \sqrt{\sigma/\rho g}$, the gravity can be neglected and we only need to consider the surface energy. Next, we are going to investigate how the surface area varies with the wavelength of undulation. The change in surface area is

$$\Delta\Sigma = \int_0^\lambda 2\pi(r+e)\sqrt{1+\left(\frac{de}{dx}\right)^2}\,dx - 2\pi\lambda(r+e_0) \tag{B.79}$$

By Taylor's expansion and neglecting the 3rd and higher orders,

$$\Delta\Sigma = -\frac{\pi\varepsilon^2\lambda}{2}\left(\frac{1}{r+e_0} - k^2(r+e_0)\right) + o(\varepsilon^2) \tag{B.80}$$

The surface area decreases only if $1/(r+e_0) - k^2(r+e_0) \geq 0$, i.e.,

$$\lambda \geq 2\pi(r+e_0) \tag{B.81}$$

In the following, we are going to find out the fastest growing mode of undulation. The pressure inside the liquid, p can be expressed as

$$p = p_0 + \frac{\sigma}{R} - \frac{\sigma\ddot{e}}{(1+\dot{e}^2)^{\frac{3}{2}}} \cong p_0 + \frac{\sigma}{R} - \sigma\ddot{e} \tag{B.82}$$

By Taylor's expansion up to the first order, we have

$$p = p_0 + \varepsilon k^2\sigma cos(kx) + \frac{\sigma}{(r+e_0)\left(1+\frac{\varepsilon cos(kx)}{r+e_0}\right)}$$

$$p = p_0 + \frac{\sigma}{r+e_0} + \varepsilon\sigma cos(kx)\left(k^2 - \frac{1}{(r+e_0)^2}\right) \tag{B.83}$$

By the Poiseuille's law, the flow rate is proportional to the pressure gradient

$$Q = C_1\left(-\frac{\partial p}{\partial x}\right) \tag{B.84}$$

By conservation of mass, we have

$$\frac{\partial Q}{\partial x} = \frac{\partial e}{\partial t} \tag{B.85}$$

Finally, we arrive at the dynamic equation for liquid jet

$$\frac{\partial\varepsilon}{\partial t} = \frac{\varepsilon}{\tau(k)} \tag{B.86}$$

where

$$\frac{1}{\tau(k)} = C_1\ k^2\left(k^2 - \frac{1}{(r+e_0)^2}\right) \tag{B.87}$$

Hence, it is obvious that $\tau(k)$ is minimized when $k = 1/\sqrt{2}(r + e_0)$, i.e.,

$$\lambda = 2\sqrt{2}\pi R = 4.44D \tag{B.88}$$

Remark:

In this simple analysis, we decoupled the Navier-Stokes equation into Poiseuille's Law (for steady-state unidirectional flow) and a transient mass balance equation. This decoupling is valid only when the Reynold's number Re is small (the convective time scale $\tau_c \sim L/U$ is much larger than the viscous time scale $\tau_v \sim \rho L^2/\mu$). In addition, Poiseuille's law will not be valid for non-unidirectional flows. Therefore, the analysis above can only be valid for the onset of the breakup of liquid jets when then surface is relatively flat. However, unfortunately, this simply analysis cannot capture the evolution of the undulatory motion of the liquid jets. Although the fast growing wavelength obtained from the analysis above is closed to the result for inviscid liquid jet, the result in this section does not have much realistic physical meaning.

Appendix C

Tomotika Functions

In the theoretical treatment by Tomotika [64], he defined some functions that are involved in the dispersion relation for the breakup of liquid threads immersed in another viscous fluid at rest. They are listed in the following, where superscript $'$ represents the fluid jet inside.

$$\begin{aligned} F_1 &= 2i\frac{\mu'}{\mu}\kappa^2\widetilde{I}_1'(\kappa a) - \frac{\omega\rho}{\mu}\widetilde{I}_0(\kappa a) + \frac{\sigma(\kappa^2a^2-1)}{a^2}\frac{\kappa}{\omega\mu}\widetilde{I}_1(\kappa a) \\ F_2 &= 2i\frac{\mu'}{\mu}\kappa\kappa_1'\widetilde{I}_1'(\kappa_1'a) + \frac{\sigma\kappa(\kappa^2a^2-1)}{\omega\mu a^2}\widetilde{I}_1(\kappa_1'a) \\ F_3 &= 2i\kappa^2\widetilde{K}_1'(\kappa a) + \frac{\omega\rho}{\mu}\widetilde{K}_0(\kappa a) \\ F_4 &= 2i\kappa\kappa_1\widetilde{K}_1'(\kappa_1 a) \end{aligned} \tag{C.1}$$

where

$$\kappa_1^2 = \kappa^2 + \frac{i\omega}{\nu} \qquad (\kappa_1')^2 = \kappa^2 + \frac{i\omega}{\nu'}$$

$$\Phi(x) = \frac{N(x)}{D(x)} \tag{C.2}$$

with

$$N(x) = \widetilde{I}_1(x)\Delta_1 - \left(x\widetilde{I}_0(x) - \widetilde{I}_1(x)\right)\Delta_2$$

$$D(x) = \frac{\mu'}{\mu}\left(x\widetilde{I}_0(x) - \widetilde{I}_1(x)\right)\Delta_1 - \frac{\mu'}{\mu}\left((x^2+1)\widetilde{I}_1(x) - x\widetilde{I}_0(x)\right)\Delta_2$$

$$-\left(x\widetilde{K}_0(x)+\widetilde{K}_1(x)\right)\Delta_3-\left((x^2+1)\widetilde{K}_1(x)+x\widetilde{K}_0(x)\right)\Delta_4$$

$$\Delta_1 = det\begin{pmatrix} x\widetilde{I}_0(x)-\widetilde{I}_1(x) & \widetilde{K}_1(x) & -x\widetilde{K}_0(x)-\widetilde{K}_1(x) \\ \widetilde{I}_0(x)+x\widetilde{I}_1(x) & -\widetilde{K}_0(x) & -\widetilde{K}_0(x)+x\widetilde{K}_1(x) \\ (\mu'/\mu)x\widetilde{I}_0(x) & \widetilde{K}_1(x) & -x\widetilde{K}_0(x) \end{pmatrix}$$

$$\Delta_2 = det\begin{pmatrix} \widetilde{I}_1(x) & \widetilde{K}_1(x) & -x\widetilde{K}_0(x)-\widetilde{K}_1(x) \\ \widetilde{I}_0(x) & -\widetilde{K}_0(x) & -\widetilde{K}_0(x)+x\widetilde{K}_1(x) \\ (\mu'/\mu)\widetilde{I}_1(x) & \widetilde{K}_1(x) & -x\widetilde{K}_0(x) \end{pmatrix}$$

$$\Delta_3 = det\begin{pmatrix} \widetilde{I}_1(x) & x\widetilde{I}_0(x)-\widetilde{I}_1(x) & -x\widetilde{K}_0(x)-\widetilde{K}_1(x) \\ \widetilde{I}_0(x) & \widetilde{I}_0(x)+x\widetilde{I}_1(x) & -\widetilde{K}_0(x)+x\widetilde{K}_1(x) \\ (\mu'/\mu)\widetilde{I}_1(x) & (\mu'/\mu)x\widetilde{I}_0(x) & -x\widetilde{K}_0(x) \end{pmatrix}$$

$$\Delta_4 = det\begin{pmatrix} \widetilde{I}_1(x) & x\widetilde{I}_0(x)-\widetilde{I}_1(x) & \widetilde{K}_1(x) \\ \widetilde{I}_0(x) & \widetilde{I}_0(x)+x\widetilde{I}_1(x) & -\widetilde{K}_0(x) \\ (\mu'/\mu)\widetilde{I}_1(x) & (\mu'/\mu)x\widetilde{I}_0(x) & \widetilde{K}_1(x) \end{pmatrix}$$

Appendix D

Chemical Potential Gradient

In this chapter, the alternative formula of the chemical potential gradient for multi-component system is derived. For a multi-component system, the chemical potential gradient can be alternatively written as

$$\nabla\mu_i = \sum_{j\neq i} c_j \nabla(\mu_i - \mu_j) \tag{D.1}$$

where c_i is the concentration for species i. The expression for ternary system is simplified as Eq 5.12. The detailed derivation of the relation above is as follows. According to the expression for partial molar property (Eq 5.5), the generalized chemical potential by Nauman and Balsara [41] is

$$\mu_i = \Upsilon + \left(\frac{\partial\Upsilon}{\partial c_i}\right)_{T,P,c_{m\neq i}} - \sum_k c_k \left(\frac{\partial\Upsilon}{\partial c_k}\right)_{T,P,c_{m\neq k}} \tag{D.2}$$

Hence,

$$\mu_i - \mu_j = \left(\frac{\partial\Upsilon}{\partial c_i}\right)_{T,P,c_{m\neq i}} - \left(\frac{\partial\Upsilon}{\partial c_j}\right)_{T,P,c_{m\neq j}} \tag{D.3}$$

Since

$$\nabla\Upsilon = \sum_k \nabla c_k \left(\frac{\partial\Upsilon}{\partial c_k}\right)_{T,P,c_{m\neq k}} \tag{D.4}$$

the chemical potential gradient of species i can be simplified

$$\nabla\mu_i = \nabla\Upsilon + \nabla\left(\frac{\partial\Upsilon}{\partial c_i}\right)_{T,P,c_{m\neq i}} - \sum_k \nabla c_k \left(\frac{\partial\Upsilon}{\partial c_k}\right)_{T,P,c_{m\neq k}} - \sum_k c_k \nabla\left(\frac{\partial\Upsilon}{\partial c_k}\right)_{T,P,c_{m\neq k}}$$

$$= \nabla \left(\frac{\partial \Upsilon}{\partial c_i} \right)_{T,P,c_{m \neq i}} - \sum_k c_k \nabla \left(\frac{\partial \Upsilon}{\partial c_k} \right)_{T,P,c_{m \neq k}} \tag{D.5}$$

From Eq D.3, we have

$$\sum_{j \neq i} c_j \nabla(\mu_i - \mu_j) = \left(\sum_{j \neq i} c_j \right) \nabla \left(\frac{\partial \Upsilon}{\partial c_i} \right)_{T,P,c_{m \neq i}} - \sum_{j \neq i} c_j \nabla \left(\frac{\partial \Upsilon}{\partial c_j} \right)_{T,P,c_{m \neq j}}$$

$$= (1 - c_i) \nabla \left(\frac{\partial \Upsilon}{\partial c_i} \right)_{T,P,c_{m \neq i}} - \left(\sum_k c_k \nabla \left(\frac{\partial \Upsilon}{\partial c_k} \right)_{T,P,c_{m \neq k}} - c_i \nabla \left(\frac{\partial \Upsilon}{\partial c_i} \right)_{T,P,c_{m \neq i}} \right) = \nabla \mu_i \tag{D.6}$$

Appendix E

Curvature

The following provides a general derivation of the mean curvature of an axisymmetric surface (4.2). The mean curvature of a surface C is defined as half of the divergence of the normal vector $\mathbf{n}$, i.e.,

$$2C = \nabla \cdot \mathbf{n} \tag{E.1}$$

An axisymmetric surface can be represented by $f(r, z) = r - S(z) = 0$. The normal vector is

$$\mathbf{n} = \frac{\nabla f}{|\nabla f|} \qquad 2C = \nabla \cdot \frac{\nabla f}{|\nabla f|} \tag{E.2}$$

where the gradient and divergence in cylindrical coordinate are defined as

$$\nabla f = \frac{\partial f}{\partial r}\mathbf{e}_r + \frac{1}{r}\frac{\partial f}{\partial \theta}\mathbf{e}_\theta + \frac{\partial f}{\partial z}\mathbf{e}_z \tag{E.3}$$

$$\nabla \cdot v = \frac{\partial v_r}{\partial r} + \frac{v_r}{r} + \frac{1}{r}\frac{\partial v_\theta}{\partial \theta} + \frac{\partial v_z}{\partial z} \tag{E.4}$$

Hence,

$$\nabla f = 1\mathbf{e}_r + 0\mathbf{e}_\theta - S'(z)\mathbf{e}_z \tag{E.5}$$

$$\mathbf{n} = \frac{\nabla f}{|\nabla f|} = \frac{1}{\sqrt{1 + S'(z)^2}}(1\mathbf{e}_r + 0\mathbf{e}_\theta - S'(z)\mathbf{e}_z) \tag{E.6}$$

$$2C = \nabla \cdot \mathbf{n} = -\frac{r(z)''}{\left(\sqrt{1 + r'(z)^2}\right)^3} + \frac{1}{r\sqrt{1 + r'(z)^2}} \tag{E.7}$$

Appendix F

Affine Deformation

The deformation and breakup of drops in two-dimensional linear flows has been extensively studied [63][20][1][52]. A 2D linear flows can be described by a constant velocity gradient, i.e.,

$$\frac{d\mathbf{x}}{dt} = \mathbf{v} = (\nabla \mathbf{v}) \cdot \mathbf{x} \tag{F.1}$$

where

$$\nabla \mathbf{v} = \frac{G}{2} \begin{pmatrix} 1+\alpha & 1-\alpha \\ -1+\alpha & -1-\alpha \end{pmatrix}$$

with $-1 \leq \alpha \leq 1$. For $\alpha = -1$, it's purely rotational flow. For $\alpha = 0$, it's a simple shear flow. For $\alpha = 1$, it's a plane hyperbolic flow (also named as 2D elongational flow). The rate of strain tensor is

$$\Gamma = \frac{1}{2}\left(\nabla \mathbf{v} + \nabla^T \mathbf{v}\right) = \frac{G}{2} \begin{pmatrix} 1+\alpha & 0 \\ 0 & -1-\alpha \end{pmatrix} \tag{F.2}$$

The vorticity tensor is

$$\Omega = \frac{1}{2}\left(\nabla \mathbf{v} - \nabla^T \mathbf{v}\right) = \frac{G}{2} \begin{pmatrix} 0 & 1-\alpha \\ -1+\alpha & 0 \end{pmatrix} \tag{F.3}$$

and the shear rate is defined as

$$\dot{\gamma} = \sqrt{2\Gamma : \Gamma} = G(1+\alpha) \tag{F.4}$$

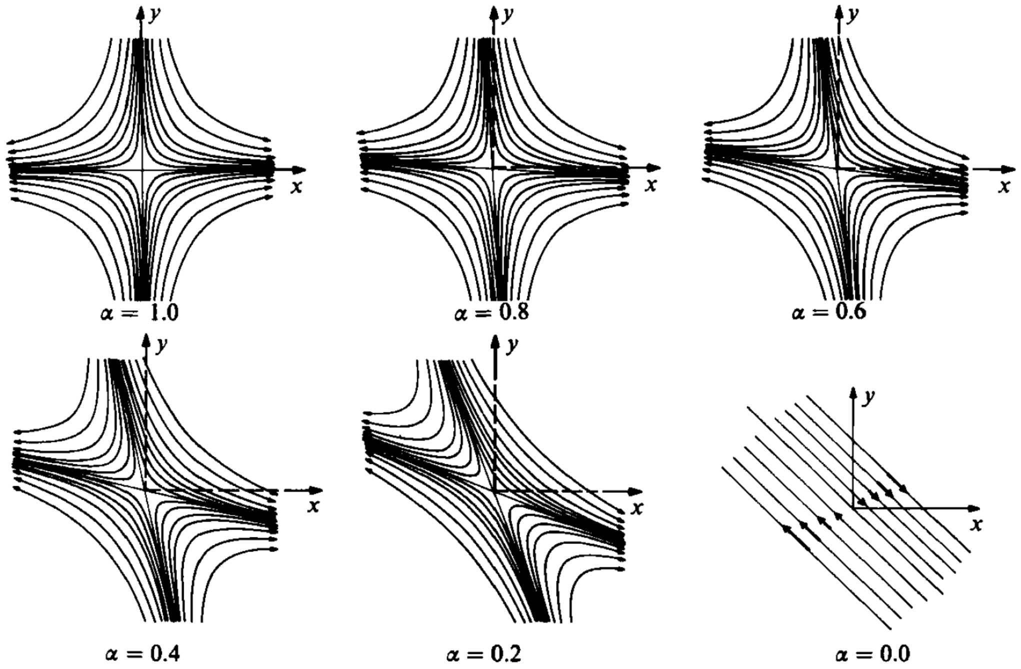

Figure F.1: The streamlines for different types of linear flows. Adopted from Bentley and Leal [6].

In the following, we are interested in the affine deformation of a sphere (like a liquid drop) in simple shear flow by neglecting the presence of interface. In order to

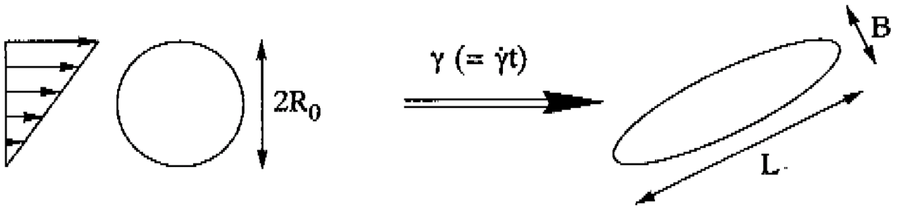

Figure F.2: The affine deformation of a sphere domain in a simple shear flow. Adopted from Janssen[31].

characterize the degree of deformation, we define a geometric parameter D as

$$D = \frac{L - B}{L + B} \tag{F.5}$$

The general idea of calculating the D values for different types of linear flow is as follows:

1 Find the deformation gradient tensor $F = \partial\mathbf{x}(t)/\partial\mathbf{X}$ by solving the system of ODEs for $\mathbf{x}$ (Eq F.1)
2 Find the Cauchy-Green tensor: $C = F^T F$
3 Find the eigenvectors which correspond to the principle stretching directions (in the initial coordinates) and find the corresponding eigenvalues of C: λ_1 and λ_2
4 $\sqrt{\lambda_1}$ and $\sqrt{\lambda_2}$ are the stretch factors, i.e., $L/(2R_0) = max\{\sqrt{\lambda_1}, \sqrt{\lambda_2}\}$ and $B/(2R_0) = min\{\sqrt{\lambda_1}, \sqrt{\lambda_2}\}$

where X represents the position vector at $t = 0$, i.e., $X = x(t = 0)$. The rationale for Step 3 above is that the stretching factor for an eigenvector $\mathbf{X}_i$ of the Cauchy-Green tensor (with an eigenvalue λ_i) is calculated as follows

$$\frac{|\mathbf{x}_i|}{|\mathbf{X}_i|} = \sqrt{\frac{\mathbf{x}_i \cdot \mathbf{x}_i}{|\mathbf{X}_i|^2}} = \sqrt{\frac{(F\mathbf{X}_i)^T(F\mathbf{X}_i)}{|\mathbf{X}_i|^2}} = \sqrt{\frac{\mathbf{X}_i \cdot C \cdot \mathbf{X}_i}{|\mathbf{X}_i|^2}} = \sqrt{\lambda_i} \tag{F.6}$$

However, the procedure above is not applicable to simple shear flows because the determinant of $\nabla\mathbf{v}$ is zero. We have to write the expression for the deformation in another coordinate

$$\mathbf{x} = \mathbf{X} + (Gt)X_2\mathbf{e}_1 \tag{F.7}$$

and the deformation gradient tensor is

$$F = \frac{\partial\mathbf{x}}{\partial\mathbf{X}} = \begin{pmatrix} 1 & Gt \\ 0 & 1 \end{pmatrix} \tag{F.8}$$

and the Cauchy-Green tensor is

$$C = F^T F = \begin{pmatrix} 1 & Gt \\ Gt & (Gt)^2 + 1 \end{pmatrix} \tag{F.9}$$

from which we can find the eigenvalues and eigenvectors of C.

In summary, for a 2D simple shear flow,

$$\frac{L}{2R_0} = \frac{1}{2}Gt + \frac{1}{2}\sqrt{4+(Gt)^2} \qquad \frac{B}{2R_0} = -\frac{1}{2}Gt + \frac{1}{2}\sqrt{4+(Gt)^2} \tag{F.10}$$

$$D = \frac{Gt}{\sqrt{(Gt)^2+4}}$$

For a 2D plane hyperbolic flow,

$$\frac{L}{2R_0} = e^{Gt} \qquad \frac{B}{2R_0} = e^{-Gt} \qquad D = tanh(Gt) \tag{F.11}$$

Bibliography

[1] Acrivos, A., *Annals of the New York Academy of Sciences*, 404:1-11

[2] Akashi, N. et al, *Ultrasonics*, 38:915-919 (2000)

[3] Albertsson, P.-A., Partition of Cell Particles and Macromolecules, 3rd Edition, Wiley, New York, (1986)

[4] Aref, H., *Journal of Fluid Mechanics*, 143: 1-21 (1984)

[5] Ariyapadi, M. V. and Nauman, E. B., *Journal of Polymer Science*, 28:2395-2409 (1990)

[6] Bentley, B. J. and Leal, L. G., *Journal of Fluid Mechanics*, 167:241-283 (1986)

[7] Bray, A. J., *Advances in Physics*, 51:2, 481-587 (2002)

[8] Cahn, J. W., and Hilliard, J. E., *Journal of Chemical Physics*, 28(2), 258-267 (1958)

[9] Callen, H. B., Thermodynamics and an Introduction to Thermostatistics, 2nd Edition, John Wiley and Sons, (1985)

[10] Christiansen, R. M. and Hixson, A. N., *Industrial & Engineering Chemistry Research*, 49:1017-1024 (1957)

[11] de Gennes, P. G., et al, Gouttes, Bulles, Perles et Ondes, Belin (2005)

[12] de Laplace, P. S., *Œuvres complètes de Laplace, t. IV, Supplément au livre X du traité de la mécanique célese*, P. 394 - 2e *supplément au livre X*, p. 419, Ch.I

[13] Diamond, A. D. et al, *Biotechnology techniques*, 3(2):119-124 (1989)

[14] Dittrich, P. S. and Manz, A. *Nature Reviews Drug Discovery*, 5(3):210 (2006)

[15] Dittrich, P. S. et al, *Analytical Chemistry*, 78(12):3887-3907 (2006)

[16] Drazin, P. D., Introduction to Hydrodynamic Stability, Cambridge University Pressure (2002)

[17] Eliassi, A. and Modarress, H., *Journal of Chemical & Engineering Data*, 43:719-721 (1998)

[18] Forciniti, D. et al, *Journal of Biotechnology*, 16:279-296 (1990)

[19] Fujioka, K. et al, *Journal of Chemical Physics* 98(1):717-728 (1993)

[20] Grace, H. P., *Engineering Foundation Research Conference on Mixing* (1971). Republished in *Chemical Engineering Communications*, 14:225-277 (1982)

[21] Gurtin, M. E., *Physica D*, 92:178-192 (1996)

[22] Gurtin, M. E., Polignone, D. and Vinals, J., Two-Phase binary fluids and immiscible fluids described by an order parameter (2008)

[23] Hashimoto, T. et al, *Journal of Chemical Physics*, 88(9):5874-5881 (1988)

[24] Hashimoto, T. et al, *Physical Review Letters*, 74:126 (1995)

[25] He, D. Q. et al, *Macromolecular Theory and Simulations*, 5:801-827 (1996)

[26] Helfrich, M. R. et al, *Langmuir*, 21:8478-8486 (2005)

[27] Hodges, S. R. et al, *Journal of Fluid Mechanics*, 501:279-301 (2004)

[28] Hohenberg, P. C. and Halperin, B. I., *Reviews of Modern Physics*, 49:435-479 (1977)

[29] Gaul, Kögl and Wagner, Appendix B, Boundary Element Methods for Engineers and Scientists, Springer (2003)

[30] Jahnisch, K. et al, *Angewandte Chemie International Edition*, 43:406-446 (2004)

[31] Janssen, J. M. H., Dynamics of Liquid-Liquid Mixing, Ph.D Thesis, Technische Universiteit Eindhoven (1993)

[32] Janssen, J. M. H. and Meijer, H. E. H., *Journal of Rheology*, 37(4):597-608 (1993)

[33] Jensen, K. F., *Chemical Engineering Science*, 56(2):293-303 (2001)

[34] Johansson, H. et al, *Journal of Chromatography B*, 711:3-17 (1998)

[35] Karam, H. J. and Bellinger, J. C., *Industrial & Engineering Chemistry Fundamentals*, 7:576-583, (1968)

[36] Karr, L. J. et al, *Journal of Chromatography A*, 354:269-282 (1986)

[37] Khakhar, D. V. and Ottino, J. M., *International Journal of Multiphase Flow*, 13:71-86 (1987)

[38] Kinoshita, C. M. et al, *International Journal of Multiphase Flow*, 20(3):523-533 (1994)

[39] Lowengrub, J. and Truskinovsky, L., *Proceedings of the Royal Society A*, 454(1978):2617-2654 (1998)

[40] Lister, J. R. and Stone, H. A., *Physics of Fluids*, 10(11):2758-2764 (1998)

[41] Nauman, E. B. and Balsara, N. P., *Fluid Phase Equilibria*, 45:229-250 (1989)

[42] Nauman, E. B. and He, D. Q., *Chemical Engineering Science*, 56:1999-2018 (2001)

[43] Migler, K. B., *Physical Review Letters*, 86:1023 (2001)

[44] Mikami, T. et al, *International Journal of Multiphase Flow*, 2:113-138 (1974)

[45] Minton, A. P., *Journal of Cell Science*, 119:2863-2869 (2006)

[46] Ottino, J. M., The kinematics of mixing : stretching, chaos, and transport, Cambridge University Press (1989)

[47] Papageorgiou, D. T., *Journal of Fluid Mechanics*, 301:109-132 (1995)

[48] Pavlov, G. M. et al, *Carbohydrate Polymers*, 38:267-271 (1999)

[49] Pihl, J. et al, *Drug Discovery Today*, 10(20):1377-1383 (2005)

[50] Plateau, J., Statique expérimentale et théorique des liquides soumis aux seules forces moléculaire, *Gauthier-Villars*, Paris (1873)

[51] Pozrikidis, C., Introduction to Theoretical and Computational Fluid Dynamics, Oxford University Press (1997)

[52] Rallison, J. M., *Annual Review of Fluid Mechanics*, 16:45-66

[53] Rayleigh, L.,On the instability of jets, *Proceedings London Mathematical Society*, 10:4-13 (1878)

[54] Rayleigh, L., *Philosophical Magazine and Journal of Science*, 34. No.207 (1892)

[55] Rumscheidt, F. D. and Mason, S. G., *Journal of Colloid and Interface Science*, 16:238-261, (1961)

[56] Ryden, J. and Albertsson, P., *Journal of Colloid and Interface Sciences*, 37(1):219 (1971)

[57] Song, H. et al, *Angewandte Chemie International Edition*, 42(7):768-72 (2003)

[58] Song, H. and Ismagilov, R. F., *Journal of the American Chemical Society*, 125 (47):14613 (2003)

[59] Stone, H. A. and Brenner, M. P., *Journal of Fluid Mechanics*, 318:373-374 (1996)

[60] Takebe, T. et al, *Journal of Chemical Physics*, 91(7):4369-4379 (1989)

[61] Takebe, T. et al, *Journal of Chemical Physics*, 93(7):5271-5280 (1990)

[62] Tan, Y. C. and Lee, A. P., *Lab on a Chip*, 5:1178-1183 (2005)

[63] Taylor, G. I., *Proceedings of the Royal Society A*, 146:501-523 (1934)

[64] Tomotika, S., *Proceedings of the Royal Society A*, 150:322-337 (1935)

[65] Tomotika, S., *Proceedings of the Royal Society A*, 153:302-318 (1936)

[66] Van Ness, H. C. and Abbott, M. M., Classical Thermodynamics of Nonelectrolyte Solutions, MaGraw-Hill, pp. 47-48 (1982)

[67] Torza, S. et al, *Journal of Colloid and Interface Science*, 38:395-411 (1972)

[68] Walter, H. et al, Partitioning in Aqueous Two-Phase Systems: Theory, Methods, Uses, and Applications to Biotechnology, Adademic Press, New York (1985)

[69] Xia, Y. and Whitesides, G. M., *Annual Review of Materials Science*, 28:153-184 (1998)

[70] Young, T., *Philosophical Transactions of the Royal Society of London*, 95:65-87 (1805)

[71] Yu, J. D. et al, *Journal of Computational Physics*, 206(1):227-251 (2005)

[72] Zapryanov, Z. and Tabakova, S., Dynamics of Bubbles, Drops and Rigid Particles, Springer (1998)